INFORMATION TO USERS

This manuscript has been reproduced from the microfilm master. UMI films the text directly from the original or copy submitted. Thus, some thesis and dissertation copies are in typewriter face, while others may be from any type of computer printer.

The quality of this reproduction is dependent upon the quality of the copy submitted. Broken or indistinct print, colored or poor quality illustrations and photographs, print bleedthrough, substandard margins, and improper alignment can adversely affect reproduction.

In the unlikely event that the author did not send UMI a complete manuscript and there are missing pages, these will be noted. Also, if unauthorized copyright material had to be removed, a note will indicate the deletion.

Oversize materials (e.g., maps, drawings, charts) are reproduced by sectioning the original, beginning at the upper left-hand corner and continuing from left to right in equal sections with small overlaps. Each original is also photographed in one exposure and is included in reduced form at the back of the book.

Photographs included in the original manuscript have been reproduced xerographically in this copy. Higher quality 6" x 9" black and white photographic prints are available for any photographs or illustrations appearing in this copy for an additional charge. Contact UMI directly to order.

UMI

A Bell & Howell Information Company
300 North Zeeb Road, Ann Arbor MI 48106-1346 USA
313/761-4700 800/521-0600

The Effect of Vertical Mixing on Along Channel Transport in a Layered Flow

by

Cynthia Nova Cudaback

A dissertation submitted in partial fulfillment of
the requirements for the degree of

Doctor of Philosophy

University of Washington

1998

Approved by David A Jay
(Chairperson of Supervisory Committee)

Program Authorized
to Offer Degree Geophysics Program

Date May 20, 1998

In presenting this dissertation in partial fulfillment of the requirements for the Doctoral degree at the University of Washington, I agree that the Library shall make its copies freely available for inspection. I further agree that extensive copying of this dissertation is allowable only for scholarly purposes, consistent with "fair use" as prescribed in the U.S. Copyright Law. Requests for copying or reproduction of this dissertation may be referred to University Microfilms, 1490 Eisenhower Place, P.O. Box 975, Ann Arbor, MI 48106 to whom the author has granted "the right to reproduce and sell (a) copies of the manuscript in microform and/or (b) printed copies of the manuscript made from microform."

Signature Carl Lindabaek

Date May 19, 1998

University of Washington

Abstract

The Effect of Vertical Mixing on Along Channel Transport in a Layered Flow

by Cynthia Nova Cudaback

Chairperson of Supervisory Committee
Adjunct Research Associate Professor David A. Jay
Geophysics Program

The Columbia River has a large, biologically productive estuary whose ecosystem depends on the balance of salt and fresh water. Outflow from the river also forms a vast buoyant plume which affects circulation for hundreds of miles along the coast. Both the estuarine salt balance and the initial state of the plume are determined by flow through the narrow entrance channel. I have made a three-part study of the effects of interfacial turbulence and bottom friction on along-channel transport through the Columbia River entrance channel.

My observations in the Columbia River entrance channel show that both interfacial mixing and bottom friction significantly affect circulation. The pycnocline is thinned by lateral advection on flood and thickened by vertical mixing on ebb and . On late flood, the pycnocline is close to the surface and quite thin; on late ebb, its center is below mid-depth and it fills 3/4 of the water column. Bottom friction retards the near-bottom currents, so early flood currents are strongest at mid-depth, and peak

flood currents are strongest at the surface. At peak ebb and peak flood, salinity transport is strongest at mid-depth.

A two-layer time-dependent model [Helfrich, 1995] simulates along-channel currents and layer thicknesses. By assuming a near-critical bulk Richardson number, I estimated the pycnocline thickness from the two-layer model results. Bottom friction raises the pycnocline and causes tidal variations in vertical shear, which drive the changes in pycnocline thickness. This model replicates the observed pycnocline quite well, but cannot simulate mid-depth currents.

I created a new three-layer time-dependent model, in which the middle layer represents the pycnocline. Mixing of salt and fresh water creates water of intermediate density, which is modeled as entrainment from the top and bottom layers into the middle layer. This model simulates along-channel circulation at all stages of the tide, including the mid-depth maximum at early flood. It also simulates the vertical distribution and tidal average of salinity transport. For the best fit to observations, the three-layer model requires significantly more bottom friction than the two-layer model; this is consistent with the formulation of the bottom roughness coefficient.

TABLE OF CONTENTS

LIST OF FIGURES

ACKNOWLEDGMENTS

In November of 1805, when the Lewis and Clark expedition reached the entrance to the Columbia River, after a long and dangerous journey, William Clark wrote in his journal:

Great joy in camp. We are in view of the ocean, this great Pacific Ocean, which we have been so long anxious to see.

I feel much the same way about finally defending my PhD thesis. It has been a long hard journey, and I've had a great deal of help. This journey started when my parents, David and Dorothea Cudaback, first gave me a teddy bear representing the Cal mascot; they have encouraged me academically ever since. More recently, when I was a NOAA Corps officer, Bill Lavelle chose to treat me as a graduate student in estuarine studies. It was that work which inspired my advisor, David Jay, to retrieve my application from the Oceangraphy department and offer me a place in Geophysics. My committee members, Barbara Hickey, Marcia Baker and Parker McCready have been encouraging and helpful through the entire process. Andy Jessup provided the ship time for a key cruise, Jeff Musiak set up all the instruments, and Karl Helfrich gave me his model code – without their help, this thesis would not exist.I'm also grateful for the assistance of Mitsuhiro Kawase, Rocky Geyer, Larry Armi and many others. Finally, and most of all, I am grateful to all the powers that be for bringing me here to meet my husband, Andrew Newell. Not only does he cook clean and provide emotional support, but he has read

most of this thesis and greatly improved the writing.

I am grateful for financial support from several grants: an Office of Naval Research graduate student fellowship, National Science Foundation Grant OCE-9807118 (Columbia River Land-Margin Ecosystem Research Project; LMER), Office of Naval Research Grant N00014-94-1-0009 (Circulation in Stratified Tidal Channels and Straits) and National Science Foundation Grant OCE-8918193 (The Columbia River Plume Project). Dr. B. Hickey provided the map of plume salinities.

DEDICATION

This work is dedicated to my parents, David and Dorothea Cudaback, who started me on this journey, and to my husband, Andrew Newell, who made it worth completing

Chapter 1

INTRODUCTION

Great joy in camp. We are in view of the ocean, this great Pacific Ocean, which we have been so long anxious to see.

When Captain William Clark wrote these words in his journal, on November 7, 1805, he was near the mouth of the Columbia River and the end of an epic journey. His company had made a long hard trek across the plains and the Rockies, and finally traveled most of the river's 1200 mile length in small unstable boats. In those days, the river was wild, savage and dangerous.

Now the river is tamed by 19 dams that divert the flow for irrigation and power production. Between the wild and scenic stretches of the Snake River and the Pacific Ocean, the river collects the effluvia of clear cuts, farms, a plutonium plant, paper mills and cities. Yet, after all these human depredations, the Columbia remains one of the least polluted large rivers in the country. It carries 3/4 of the fresh water entering the Pacific Ocean between San Francisco and the Canadian border. The point where it enters the Pacific Ocean is one of the most dangerous river bars in the world. This is my study area.

All transport of water, salt, nutrients, sediments and pollutants between the Columbia River and the Pacific Ocean is controlled in the narrow entrance channel of the river. The salt wedge which enters the estuary through the channel determines boundary conditions for estuarine circulation and strongly affects the productive estuarine ecosystem and salmon fishery. The fresh water entering the ocean has a

significant effect on coastal and shelf circulation and on cross-shelf transport. The interaction of riverine and oceanic water masses in the channel is thus important to the study of physical oceanography as well as marine biology and ecology. The exchange of salt and fresh water in the channel may be pictured as a two-layer flow, with seaward-moving fresh water overlying landward-moving salt water, but the reality is much more complicated. This thesis deals with some of these complications.

1.1 The Project

This thesis project grew out of questions regarding the relevance of one-dimensional, two-layer internal hydraulic control theory [Armi and Farmer, 1986; Farmer and Armi, 1986], (Chapter 5) in the Columbia River entrance channel. I designed and conducted a research cruise to collect along-channel sections for comparison with the predictions of the two-layer theory (Chapter 3). Two important aspects of observed circulation were not predicted by the existing theory[Cudaback and Jay, 1996]. First, observed lateral variations in density and velocity structure are not included in the one-dimensional theory. Second, both bottom friction and shear-induced turbulent mixing significantly influence estuarine circulation, but are not allowed in the classic inviscid theory. Some turbulent effects may be explained using variants on the two-layer model (Chapter 4 and Chapter 5), but one intriguing detail of observed circulation lies completely outside the two-layer model. Early on flood, currents are strongest at mid-depth, due to a combination of baroclinic, barotropic and frictional forces.

This mid-depth maximum in flood currents should have a significant effect on salt transport into the estuary. Whereas a bottom current carries the saltiest water, a mid-depth current carries water of intermediate salinity. Bottom friction further reduces net transport. One possible application of my work is modeling changes in salt transport due to a jetty or other engineered change in a channel. A two-

layer frictionless model may significantly overestimate the amount of salt entering the estuary; a three-layer model with bottom friction is far more accurate.

I created a new three-layer, one-dimensional model to simulate both along-channel and temporal variations in along channel currents, with special interest in the flood circulation pattern (Chapter 6). In this model, the middle layer represents the pycnocline; it may grow by entrainment from the other two layers or contract by differential advection. The model formulation is a generalization of a two-layer model by Helfrich [1995], and the parameterization of vertical entrainment is from Ellison and Turner [1959]. The speed and thickness of each layer varies both spatially, in response to channel topography, and temporally, in response to imposed tidal transport. Agreement between model results and observed circulation is good, and the model produces a mid-depth maximum in early flood currents as observed (Chapter 7).

1.2 Physical Setting

1.2.1 The Estuary

The Columbia River estuary occupies a drowned river valley on the border between Oregon and Washington. The triangular basin in figure 1.1 is 15 km wide at its widest and about 70 km long. The salt wedge advances 18-60 km up the estuary, depending on river flow and tidal conditions. There are two main channels, each 8-10 meters deep, and several minor channels braided among tidal islands. The major shoal just landward of the Astoria-Megler bridge once held barns for the horses who towed beach seines to catch fish in the shallow water. The navigation channel along the south side of the river is dredged to about 14 meters depth for international shipping. Except in shallow peripheral areas, the estuary is sand-bedded. Sand waves of 0.5-2 meters height are common.

Most of the Columbia river drainage basin is east of the Cascade mountains; this eastern sub-basin is quite dry. Only 6% of the total drainage area is west of the

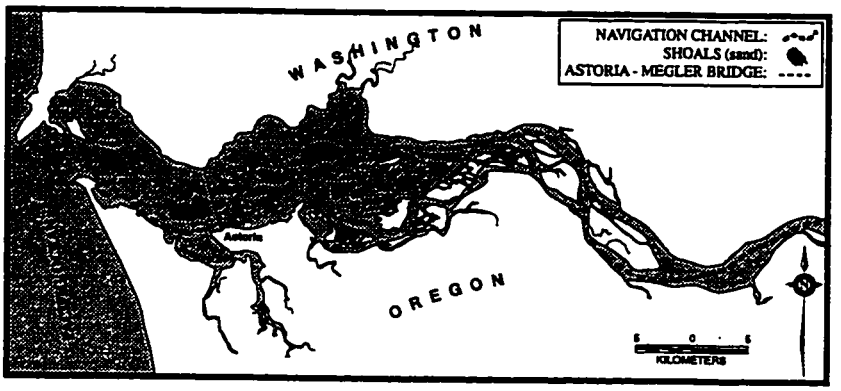

Figure 1.1: Map of the Columbia River estuary. The navigation channel is shown as a dotted line, land is white and mud flats are dark grey. There is a second channel along the northern bank of the estuary, west of the bridge.

Cascades, but the western sub-basin receives most of the rain [Simenstad *et al.*, 1990]. The climate in these areas defines three seasons for river flow. In winter (November-March), variable rainfall west of the Cascades causes flows which vary between 3,000 $m \cdot s^{-1}$and 25,000 $m \cdot s^{-1}$on a time scale of a few days. In spring (April-June), the melting snow pack east of the Cascades causes high flows (10,000 $m \cdot s^{-1}$to 18,000 $m \cdot s^{-1}$). In fall (July-October), flow is generally low ($\approx$ 3000 $m \cdot s^{-1}$). This annual variability is much less than the natural variability, due to flow regulation through dams. However, the total annual outflow is only 15% less than it was in the Nineteenth Century [Sherwood *et al.*, 1990].

Tides on the Oregon-Washington coast are mixed diurnal and semi-diurnal with a strong fortnightly modulation. In the Columbia River estuary, the maximum diurnal tidal height range is 2.5-3.8 meters and tidal currents in the entrance channel can exceed 4 $m \cdot s^{-1}$during a spring tide. These vigorous currents drive significant vertical mixing between the salt and fresh water. The weaker neap tidal currents leave the water well stratified. The river flow and tides cause rapid flushing of the estuary

(residence time is a few days), and this rapid flushing allows the estuary to respond to monthly variations in tidal currents. Thus, the estuary switches between the well-stratified and weakly-stratified or partially mixed states twice a month [Jay and Smith, 1990a].

Biological productivity depends strongly on both salinity and suspended sediment, and is therefore affected by tidal variations in circulation. One especially productive region is the estuarine turbidity maximum (ETM), which is found near the upstream limit of salinity intrusion during both flood and ebb. Strong near-bottom currents cause high suspended sediment concentrations which are accompanied by concentrations of inorganic and organic particles, microbes, and zooplankton. Certain bacteria, at the base of the food chain, grow best when attached to particles [Baross *et al.*, 1994], and some copepods may physically cling to the sediment [Morgan, 1993]. The residence time and import of suspended particulate matter are partly controlled by two-layer exchange through the Columbia River mouth. Exchange at the mouth also controls the salt balance in the estuary. Bottom friction and vertical mixing in the entrance channel strongly affect salinity transport; this is the inspiration for my research.

1.2.2 The Plume

The fresh water of the Columbia River forms a large dynamic plume that spreads into the Pacific Ocean and turns northward due to Coriolis acceleration. The plume typically drifts offshore in summer, pushed by Ekman drift caused by prevailing northerly winds (coastal upwelling conditions). In winter, typically southerly winds create downwelling conditions, and the plume can be pressed against the Washington coast [Barnes *et al.*, 1972; Hickey *et al.*, 1998]. When combined with the plumes of other large rivers in British Columbia and Alaska this outflow forms a vast layer of relatively fresh (< 32.5 psu) water, that influences coastal circulation throughout the Northeast Pacific.

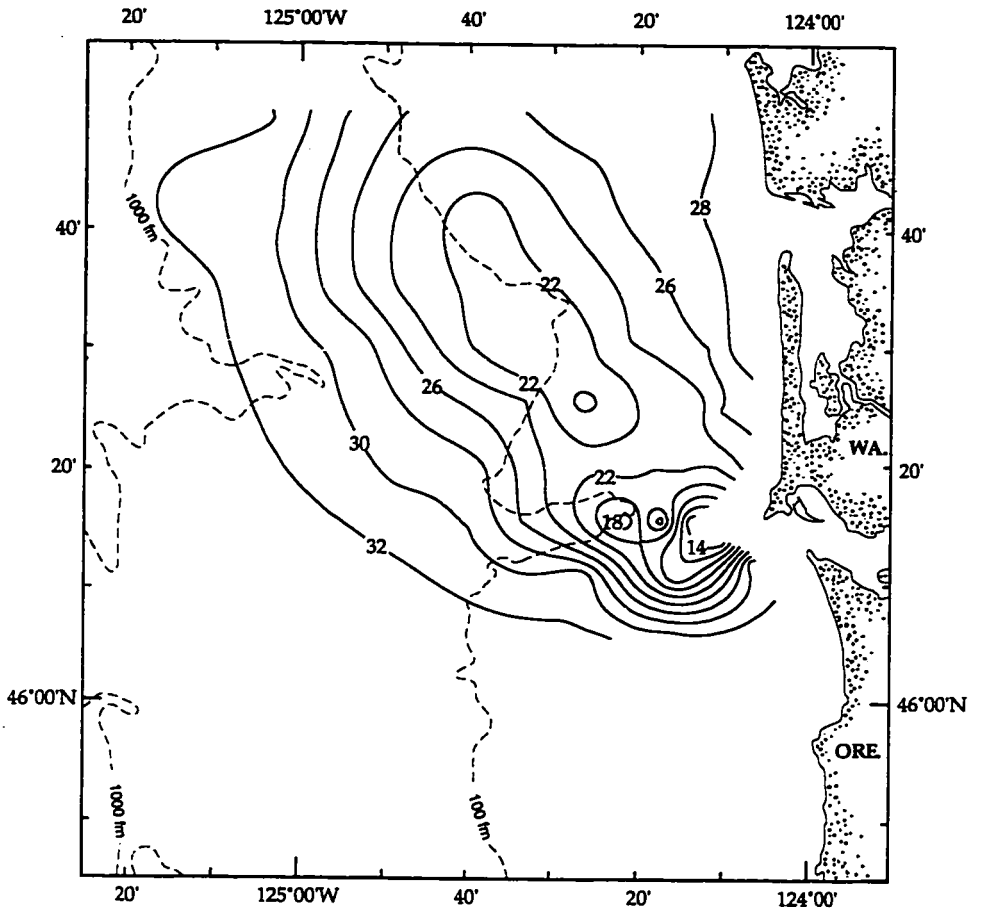

Figure 1.2: Plan view of surface salinities in the Columbia River plume. The 32 psu isopleth is about 100km offshore, and extends well beyond the experimental area. The 22 psu isopleth delineates two distinct areas of fresher water, each formed by the outflow of a single ebb. Figure reproduced from Hickey *et al.* [1998], by permission.

Essential characteristics of the river plume are determined at its origin in the constricted entrance to the river (figure 1.3). On ebb, when the strong tidal flow enhances the river outflow, the fresh plume lifts off the river bottom in the entrance channel. Lateral and vertical constrictions in the channel help determine the precise location of plume lift off from the river bottom. Flood currents block the river outflow, so the plume is formed as a series of distinct fresh pulses on successive ebbs rather than as a steady outflow. Within the greater surface freshening, the plume may thus be broken into multiple distinct, fresher areas ($<$ 22 psu, figure 1.2)

1.2.3 The Entrance Channel

The strong riverine and tidal currents in the Columbia River entrance channel have been compared to two freight trains colliding. Tidal amplitudes of 1.6-3.8 m drive currents up to 3-4 $m \cdot s^{-1}$through the narrow entrance channel. The river discharges 3,000 to 30,000 $m^3 s^{-1}$ of fresh water, which causes strong stratification ($\Delta\rho/\rho \approx 10^{-2}$) in the entrance channel. The tidal and riverine currents combined with wave action can make conditions very treacherous for ship observations, so relatively few direct observations have been made in "the graveyard of the Pacific".

These strong currents are funneled through a channel with some complex topography. The channel (figure 1.3) is 15-30 meters deep with an average width of 3 km. It is constricted laterally by the seaward convergence of the North and South entrance jetties and by a lateral jetty located 4 km landward of the entrance (Jetty A). At Jetty A, the channel width is $\approx$ 2 km, and strong currents have scoured a 30 meter deep hole. Buoy 10 is 2 km seaward of jetty A, at the crest of a modest sill. Each of these constrictions can act as an internal hydraulic control during part of the tidal cycle, but the effect of these controls is complicated by channel curvature and lateral variations in channel depth.

The channel bends almost 90°, from northeast to southeast on the landward approach. Although the radius of curvature ($R \approx$ 6-10 km) is larger than in other

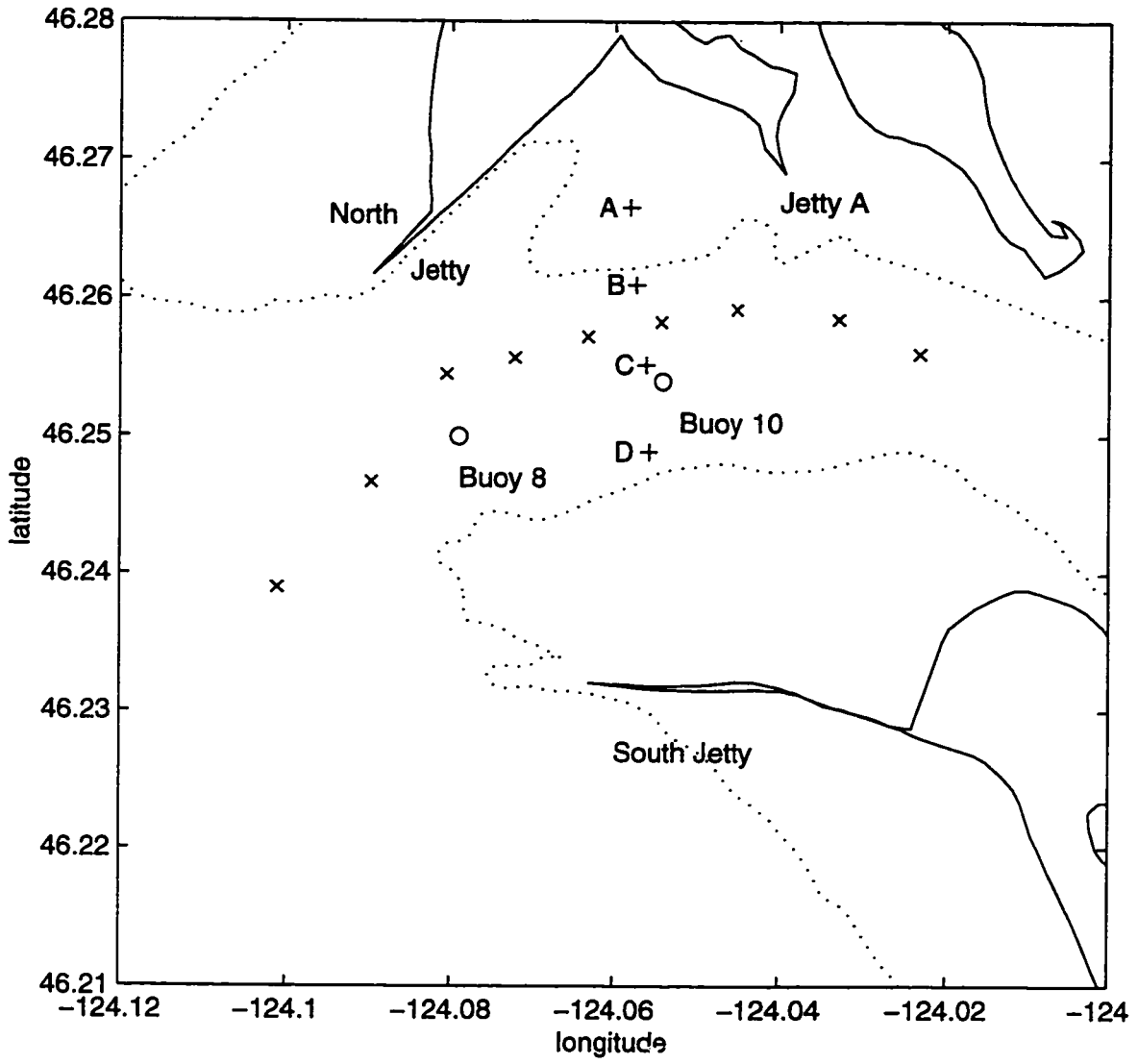

Figure 1.3: Map of Columbia River entrance area. The Pacific Ocean is to the left, and the estuary to the right. The dotted lines are the 30 foot depth contours, which mark the channel boundaries. Jetty A constricts the channel landward of Buoy 10, and the channel curves from NE to SE on the landward approach. Plus signs mark the stations at which time-series measurements were made in May, 1992; the longest time-series was taken at station D. Crosses mark the along-channel transect used in September, 1993.

systems where the effect of channel curvature has been studied in detail [Smith and McLean, 1984; Nelson, 1988; Geyer, 1993], the effect on circulation is apparent. The strong tidal and riverine currents rounding the bend are accelerated toward the inside of the curve (southward), and experience an apparent force toward the outside of the curve (northward). This results in both lateral currents and a lateral displacement of along-channel currents. The stronger currents along the outside of the bend enhance erosion along parts of the north bank of the channel and deposition on the inside (south bank) of the bend. In this respect the Columbia River entrance resembles a neutrally stratified river meander. However, dredging along the south side of the ship channel modifies the lateral depth variations of the channel.

In my observational work, I looked at two different ways this complex topography can influence the currents. First, I examined the effects of the lateral and vertical constrictions, and compared these effects with the results of internal hydraulic control theory (chapter 3 and Cudaback and Jay [1996]). Second, I studied the lateral circulation and forcing in the channel, with special attention to the effects of channel curvature [Cudaback and Jay, 1997]; this work is not included in my thesis.

The various cruises in which I participated were blessed with good weather, so I rarely felt as disheartened as Captain Clark did on December 1, 1805, when he wrote:

... 24 days since we arrived in sight of the Great Western (for I cannot say Pacific) Ocean, as I have not seen one pacific day since my arrival in its vicinity, and its waters which are forming perpetually break with immense waves on the sands and rocky coasts, tempestuous and horrible.

Chapter 2

HYDRAULIC CONTROL THEORY

Water from the Columbia River forms a fresh plume on the ocean surface, while water from the ocean forms a salt wedge in the estuary. The interface between the two water masses slopes almost from the surface to the river bed over a short stretch of the entrance channel, and the steepness of the slope is partly due to channel constrictions. The behavior of the salt and fresh layers in the channel may, to some extent, be predicted using the theory of internal hydraulic control [Armi and Farmer, 1986; Farmer and Armi, 1986]. This theory of two-layer exchange in the presence of channel constrictions is descended from the theory of one-layer hydraulic control.

2.1 One Layer Hydraulic Control Theory

One-layer hydraulic theory [Officer, 1976] analyzes the effects of lateral and vertical constrictions on the speed and depth of one-dimensional channel flow of uniform density. The same theory applies to atmospheric flows as well, but I will focus on water for this chapter. When moving water encounters a channel constriction, both the energy and total transport of the flow must be conserved. This requires that the flow either get deeper and slower or shallower and faster. What actually happens depends on the initial conditions.

The behavior of the flow depends on its initial hydraulic state, defined by the Froude number, F.

$$\mathrm{F}^2 = \frac{u^2}{gh} \tag{2.1}$$

where current speed u and water depth h both vary along channel, and g is gravita-

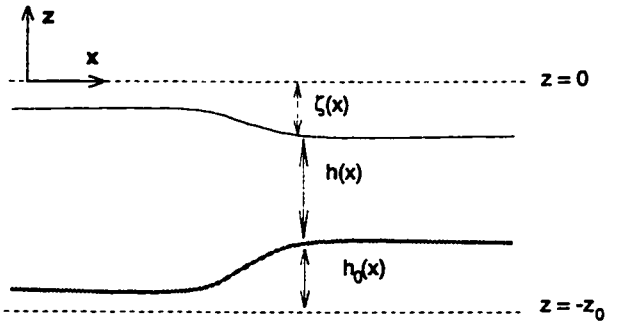

Figure 2.1: Definition sketch for one layer hydraulics, after Officer [1976].

tional acceleration. The Froude number may usefully be interpreted in either of two ways. First, F^2 is proportional to the ratio of kinetic energy (u^2) to potential energy (gh). Second, F compares the current speed with the propagation speed of surface gravity waves, $\sqrt{gh}$. In either case, the flow is defined as supercritical if $F^2 > 1$ and subcritical if $F^2 < 1$. A sill or lateral constriction may act as a point of hydraulic control and cause the flow to change from subcritical to supercritical or vice versa. If the undisturbed flow is subcritical, it is dominated by potential energy, and responds to a lateral or vertical constriction by reducing the amount of potential energy, *i.e.* decreasing h and increasing u. An initially supercritical flow is dominated by kinetic energy and responds to a constriction by increasing h and decreasing u. Changes in the flow may also be interpreted in terms of propagation of information. At the control point, gravity waves are generated on the surface. If $F < 1$, the waves can propagate upstream or downstream, but if $F > 1$, waves can no longer propagate against the current, so no information about the control point gets to points upstream of the constriction. In anthropomorphic terms, supercritical flow is flow which cannot anticipate the effect of a downstream constriction; this condition is unstable and rarely observed.

A more quantitative explanation of this phenomenon requires a careful definition of terms and coordinates. As neither the bottom nor the free surface will, in general,

be flat, I have chosen a coordinate referenced to two arbitrary flat surfaces (figure 2.1, modified from Officer [1976]). One surface, representing $z = 0$, lies above the highest point of the free surface, and another ($z = -z_0$) lies below the lowest point of the bottom. The free surface lies a distance $\zeta(x)$ below $z = 0$, and the bottom rises by $h_0(x)$ above $z = -z_0$. The water depth is $h(x)$, so $-z_0 = h(x) + h_0(x) + \zeta(x)$. In one-dimensional flow, ρ is constant throughout the channel, and u varies only along channel.

The total Bernoulli energy, H, of a unit parcel of water in this channel is the sum of its kinetic energy, its potential energy relative to the lower reference surface ($-z_0$) and the hydrostatic pressure due to the weight of water above it. In the equations below, a free surface is assumed, so atmospheric pressure is ignored.

$$\begin{aligned} \mathrm{H} &= 1/2 \cdot \rho u^2 + \rho g(z + z_0) - \rho g(z + \zeta) && (2.2) \\ &= 1/2 \cdot \rho u^2 + \rho g(z + h + h_0 + \zeta) - \rho g(z + \zeta) && (2.3) \\ &= 1/2 \cdot \rho u(x)^2 + \rho g(h(x) + h_0(x)) && (2.4) \end{aligned}$$

where g is gravitational acceleration and ρ is the water density, assumed to be constant. Note that total energy H is independent of depth; this is part of the beauty of this method. For steady inviscid flow, Bernoulli's theorem states that H must be conserved along a streamline, or throughout the flow in steady state. Physically, if a parcel of water either moves into an area of higher pressure or is lifted over some obstacle, it loses kinetic energy. Thus, any change in h_0, such as a sill or step, must be accompanied by a change in u and h. Total volume transport $Q = u(x) \cdot h(x) \cdot b(x)$ must also be conserved, so any change in channel width b will also affect u and h.

Intuitively, it makes sense that the narrowest or shallowest part of a channel should control the flux through the channel. There is also a more dynamical explanation of hydraulic control and critical flow. For steady inviscid channel flow in a single layer with width b and bottom elevation h_o, momentum conservation may be expressed by

taking the x-derivative of the Bernoulli energy (2.4), giving:

$$u\frac{\partial u}{\partial x} = -g\frac{\partial}{\partial x}(h + h_o) \tag{2.5}$$

Conservation of mass requires that transport be constant along channel, or:

$$0 = \frac{\partial q}{\partial x} = \frac{\partial}{\partial x}(u(x) \cdot b(x) \cdot h(x)) \tag{2.6}$$

According to Armi [1986], these equations may be rewritten as:

$$\frac{1}{u}\frac{\partial u}{\partial x} = -(\frac{1}{1-\mathrm{F}^2})\frac{1}{b}\frac{\partial b}{\partial x} + (\frac{1}{1-\mathrm{F}^2})\frac{1}{h}\frac{\partial h_o}{\partial x} \tag{2.7}$$

$$\frac{1}{h}\frac{\partial h}{\partial x} = (\frac{\mathrm{F}^2}{1-\mathrm{F}^2})\frac{1}{b}\frac{\partial b}{\partial x} - (\frac{1}{1-\mathrm{F}^2})\frac{1}{h}\frac{\partial h_o}{\partial x} \tag{2.8}$$

When the flow is critical, $\mathrm{F}^2 = 1$, and the above expressions get infinitely large, unless a certain geometric condition is met, namely:

$$\frac{1}{b}\frac{\partial b}{\partial x} = \frac{1}{h}\frac{\partial h_o}{\partial x} \tag{2.9}$$

In a channel with a flat bottom and a single lateral constriction, (2.9) requires that critical flow be located at the narrows. With straight sides and a sill, the critical condition may be met only at the crest of the sill. These simple geometries have a single control point, tied to a topographic feature. With a combination of a sill and narrows, there may be more than one place where flow is critical, and these virtual controls will generally not coincide with either topographic feature. As (2.9) depends on both water depth h and sill height h_s, the location of the virtual controls depends both on channel geometry and flow strength [Armi, 1986]. This ability to move relative to topographic features defines virtual controls, which we will encounter again in two-layer flow.

2.2 Steady Two-Layer Exchange Flow

The behavior of two layers of different densities in the presence of channel constrictions has been a subject of study at least since early this century, but the full theory

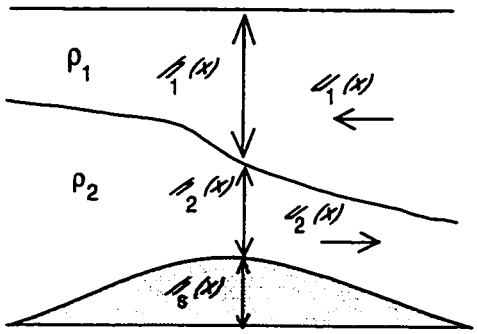

Figure 2.2: Definition sketch for two layer hydraulics. Fresh water is to the right. Fresh layer thickness is $h_1(x)$, salt layer thickness is $h_2(x)$, and sill height above flat reference level is h_s. Layer speeds are $u_i(x)$.

of steady two-layer exchange flow is due to Wood [1970] and Armi [1986]. One attractive aspect of classical steady-state theory is that the entire flow is controlled by, and may be determined from, conditions at a few points in the channel. The basic assumptions of internal hydraulic theory are as follows. One imagines a narrow channel connecting infinite basins of fresh and saline water. Baroclinic pressure gradient forces set up a steady exchange flow which moves salt water into the fresh basin and fresh water into the salt basin in two layers separated by a characteristic s-shaped interface (figure 2.2). The flow is assumed to be inviscid, so there is no vertical exchange of mass or momentum between the layers, and each layer is homogeneous and unsheared (ρ constant and u varies only in the direction of flow). Pressure is assumed to be hydrostatic, which requires that along-channel variations in width and depth be gradual. This is related to the hydraulic assumption, that the water depth is much less than the scale length of topographic features. Displacements of the free surface are usually assumed to be negligible; this is the rigid lid approximation.

In the two-layer theory, the flow may be characterized by a total internal Froude number.

$$G^2 = F_1^2 + F_2^2 = u_1^2/g'h_1 + u_2^2/g'h_2 \tag{2.10}$$

where subscripts 1 and 2 indicate the upper and lower layers, h is the layer thickness,

u is the average along-channel current speed in the layer, ρ is the average density of a given layer and g' is reduced gravity.

$$g' = g(\rho_2 - \rho_1)/\rho_2 \tag{2.11}$$

This definition of G requires that $(1 - \rho_1/\rho_2) << 1$, which is reasonable for even a highly stratified estuary. By analogy with the one-layer case, $G > 1$ defines supercritical flow, and $G < 1$ defines subcritical flow. For a purely baroclinic flow with no constrictions, the entire two-layer exchange flow should be approximately critical ($G = 1$). For a two-layer flow, there are always two control points, but under certain conditions they coalesce into a single control at a constriction or sill.

The Bernoulli energy function may again be used to predict the behavior of two-layer inviscid flows under the influence of channel constrictions. As G depends on the speed and thickness of both layers, this method can be used to predict a set of possible internal states [Armi, 1986]. The Bernoulli equations for two layers flowing over an uneven bottom (definition sketch) in the absence of barotropic currents are:

$$H_1 = 1/2 \cdot \rho_1 u_1^2 + \rho_1 g(h_1 + h_2 + h_0) + p \tag{2.12}$$

$$H_2 = 1/2 \cdot \rho_2 u_2^2 + \rho_1 g h_1 + \rho_2 g(h_2 + h_0) + p \tag{2.13}$$

where p is the atmospheric pressure at the free surface and h_0 is the bottom elevation above a flat datum [Armi, 1986]. Unlike the one-layer theory, the two-layer theory generally requires the imposition of a rigid lid, so p is finite. Note that the Bernoulli functions H_i include both the potential energy and the hydrostatic pressure as well as the kinetic energy of the flow. By analogy with the one layer case, H_i is constant in each layer, and is independent of depth z and surface displacement ζ. The energy difference between the layers, ΔH, must also be constant along the channel. Armi [1986] expresses ΔH in terms of the layer Froude numbers F_i and q_r, the ratio of the fluxes in the two layers. If q_r is fixed there is a unique (ΔH) for each (F_1, F_2) pair, so curves of constant ΔH may be plotted in the (F_1^2, F_2^2) plane. Each curve represents a

solution locus; for a given ΔH, all parts of the flow must have internal states lying on the same curve. Armi [1986] shows some elegant plots of these solution loci for flow through a constriction and over a sill.

One important solution to the conservation of Bernoulli energy in a two-layer flow is maximal exchange flow, as discussed at some length by Armi and Farmer [1986] and Farmer and Armi [1986]. In a maximal exchange flow, there is one control ($G^2 = 1$) associated with a topographic constriction (either a narrows or a sill) and a second virtual control some distance away. The interface must have a finite slope at each control point. The location of the virtual control point depends on the strength of barotropic currents in the channel, measured by q_{b0}.

$$q_{b0} = \frac{u_{b0}}{\sqrt{g'H}} \tag{2.14}$$

where u_{b0} is the barotropic current speed, H is now the total water depth and $g' = (\rho_2 - \rho_1)/\rho_2$ is reduced gravity. This scaled current speed is also called an inflow Froude number [Largier, 1992]. If $q_{b0} = 0$, the hydraulic control points ($G = 1$) coalesce at the topographic control. For a moderate barotropic current ($0 < q_{b0} < 0.544$), the virtual control point is upstream of the topographic control. Intermediate barotropic currents ($0.544 < q_{b0} < 1$) block the opposing flow, so only one layer is active. In this case, the virtual control is drawn into the upstream reservoir, and only the topographic control remains. Finally, strong barotropic currents ($q_{b0} > 1$) wash the topographic control point away, and the one-layer flow is controlled downstream of the constriction.

A maximal exchange flow is controlled at two locations, between which the currents are subcritical and isolated from either reservoir. In a sub maximal exchange flow, by contrast, the virtual control is submerged, and the internal flow is more strongly affected by conditions in the reservoir [Armi and Farmer, 1986; Farmer and Armi, 1986]. For example, if exchange through the Strait of Gibraltar is sub maximal, the transport may be affected by climate changes, but if the exchange is maximal it will be unaffected. The maximal or sub maximal nature of the flow in that channel is therefore

an important observational question [Bormans and Garrett, 1989]. Transport through the Columbia River entrance channel, however, is driven mostly by strong fluvial and tidal barotropic currents. Hydraulic effects are significant at certain stages of the tidal cycle, but the difference between maximal and sub maximal exchange is less important there.

The analytic results of Armi and Farmer [1986]; Farmer and Armi [1986] may be compared with the results of a numerical model created by Helfrich [1995]. This time-dependent model of two-layer exchange, will be discussed more in the next section. Helfrich generously provided me with a copy of the model code in FORTRAN, which I translated into MATLAB and ran to steady state with various imposed barotropic currents. Figure 2.3 shows results of model runs for a simple constriction with three different imposed barotropic currents. This may be compared with Armi and Farmer [1986], figure 9, but note that I show salt water on the left whereas their salt water is to the right. The horizontal bars in each plot indicate the strength of barotropic forcing, which may be read off the horizontal axis of the plot. From top to bottom, the plots represent strong and moderate flood (to the right), no forcing, and moderate and strong ebb (to the left).

In the absence of barotropic forcing ($q_{b0} = 0$), the interface height is 1/2 at the narrows (2.3 d), and the transport in the two layers is equal and opposite. Total Froude number G (2.10) is critical at the narrows and supercritical elsewhere; the dotted vertical line represents $G^2 = 1$. An imposed barotropic current of $|q_{b0}| = 0.54$, is almost strong enough to block the opposing layer (2.3 c,e). The interface height at the narrows is 2/3 on flood and 1/3 on ebb. The flow is critical both at the narrows and at a virtual control just upstream of the narrows. A strong imposed barotropic flow ($|q_{bo}| = 1$), washes the interface all the way out of the narrows (2.3 b,g). On flood, G is supercritical landward of the narrows, and meaningless seaward of the narrows where $h_1 = 0$ (2.3 b). The situation is reversed on ebb, giving G supercritical seaward of the narrows. All of these model results are confirmed by the analytic

results of Armi and Farmer [1986].

2.3 Time Dependent Two-Layer Flow

The next step in the evolution of internal hydraulic theory is the addition of time dependence, such as that due to an oscillating tidal current. This has been addressed by Helfrich [1995], who uses a two-layer inviscid dynamical model to predict current speeds and layer thicknesses for a baroclinic flow influenced by a barotropic current which varies sinusoidally in time, e.g., a pure semidiurnal tide. The published model does not include unequal tides or a steady flow like that of the Columbia River. [Helfrich, 1995] suggests parameters to estimate the strength of barotropic forcing and the importance of time dependence. Strength is measured by the same parameter q_{b0} (2.14), but u_{b0} is now understood to be the maximum speed of a sinusoidally varying current. Time dependence is estimated by comparison of the tidal period with the time for an internal wave to propagate across the sill. If the propagation time were very much less than a tidal period, steady state theory would still be valid [Largier, 1992]. Helfrich [1995] expresses this concept with his parameter

$$\gamma = \frac{T\sqrt{g'H}}{L} \tag{2.15}$$

the tidal period over the internal adjustment time, where T is the tidal period and L is the length scale of the sill. γ is also the ratio of the internal tidal wavelength to the length of the sill. The quasi-steady-state approximation is valid for $\gamma > 30$, or very slow tides over a short sill (Helfrich, 1995). The Columbia River entrance area (about 10 km long and 20 m deep, see figure 1.3) is subject, by these criteria, to very strong forcing with significant time dependence; $\gamma = 4 - 6$ and q_{b0} is between 1 and 1.5.

Helfrich [1995] found a number of important effects associated with strong, tidally driven barotropic currents. In a two-layer exchange flow, a fast barotropic current ($q_{b0} >= 1$) can block the opposing layer, creating a one-layer flow. Over the tidal cycle,

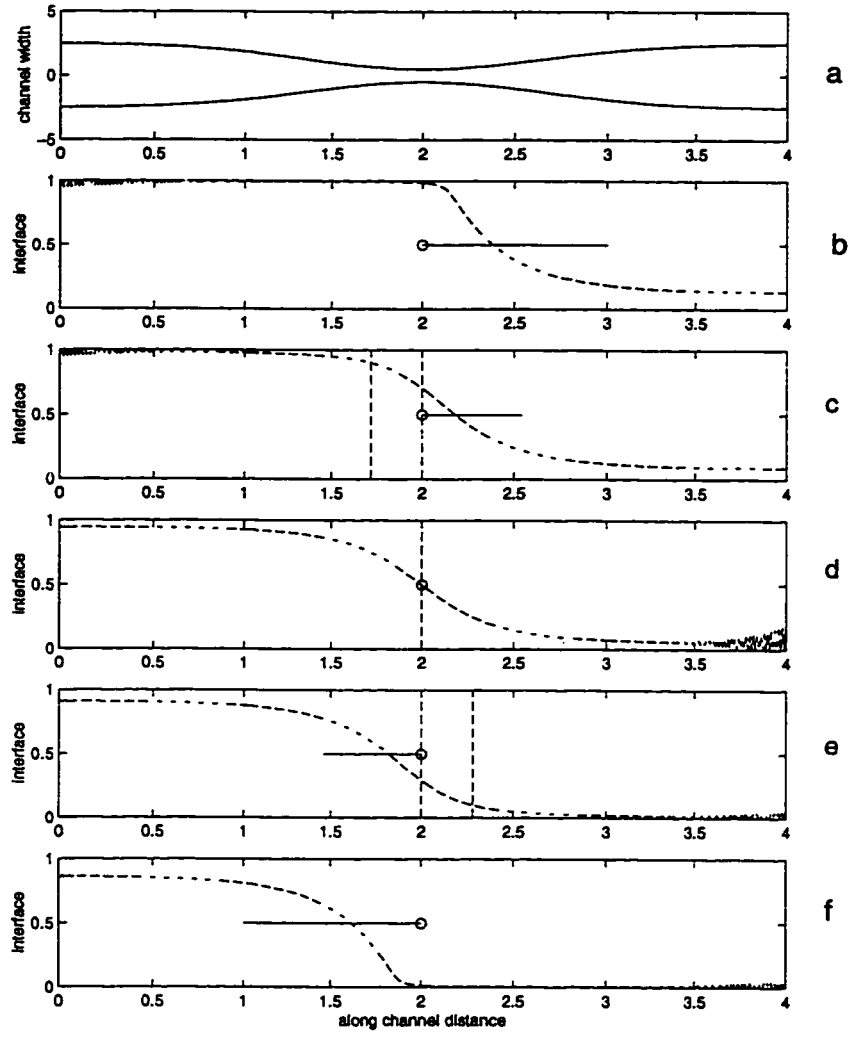

Figure 2.3: Interface positions for steady 2-layer exchange through a constriction, from time-dependent model run to steady state. Horizontal bars are vectors showing the strength of imposed barotropic currents; q_{b0} = 1, 0.54, 0, -0.54 and -1, respectively. Dotted vertical lines are control points where $G^2 = 1$; with moderate barotropic transport, there is a virtual control upstream of the narrows.

the current speed changes, so that single-layer currents at peak flood and peak ebb alternate with two-layer circulation near slack water. Another important model result is that, for a constant γ, the average exchange transport increases with increasing q_{b0}. For a constant q_{b0}, the maximum exchange is obtained in the quasi-steady limit of very large γ. Finally, the time dependence makes it impossible to determine the flow based only on fluid properties at the control points. Complete information on the geometry of the strait is needed.

Helfrich [1995] predicted the shape of the density interface and the evolution of the internal Froude number, G, for two geometries and several combinations of forcing strength and time dependence. With my copy of his model, I simulated the effect of tidal barotropic currents through a simple constriction, using parameters $q_{b0} = 1$ and $\gamma = 4$, which are appropriate for the Columbia River entrance channel. My figures 2.4 and 2.5 contain the same information as Helfrich [1995] figures 6 and 7.

In figure 2.4, the tidal motion of the layer interface is apparent. Both flood and ebb currents cause bore propagation in the direction of the current. A steady flow of strength $q_{b0} = 1$ would push the opposing layer out of the narrows (see figure 2.3), but the tidal current does not quite manage to eject the opposing layer. The vertical oscillation of the interface at the narrows is shown in figure 2.5a. As the total barotropic transport Q reverses, the upper and lower layer currents move in alternation (2.5b). The upper layer carries most of the ebb transport ($q_1 < 0$), whereas the lower layer carries the flood transport ($q_2 > 0$). Note that lower layer transport is thus plotted above upper layer transport. The Froude number of each layer is dominated by transport, so that F_1 is supercritical on ebb and F_2 is supercritical on flood. The total Froude number, G is critical only at slack water and supercritical at all other stages of the tide. These results are consistent with observations in the Columbia River entrance channel, as discussed in the next chapter.

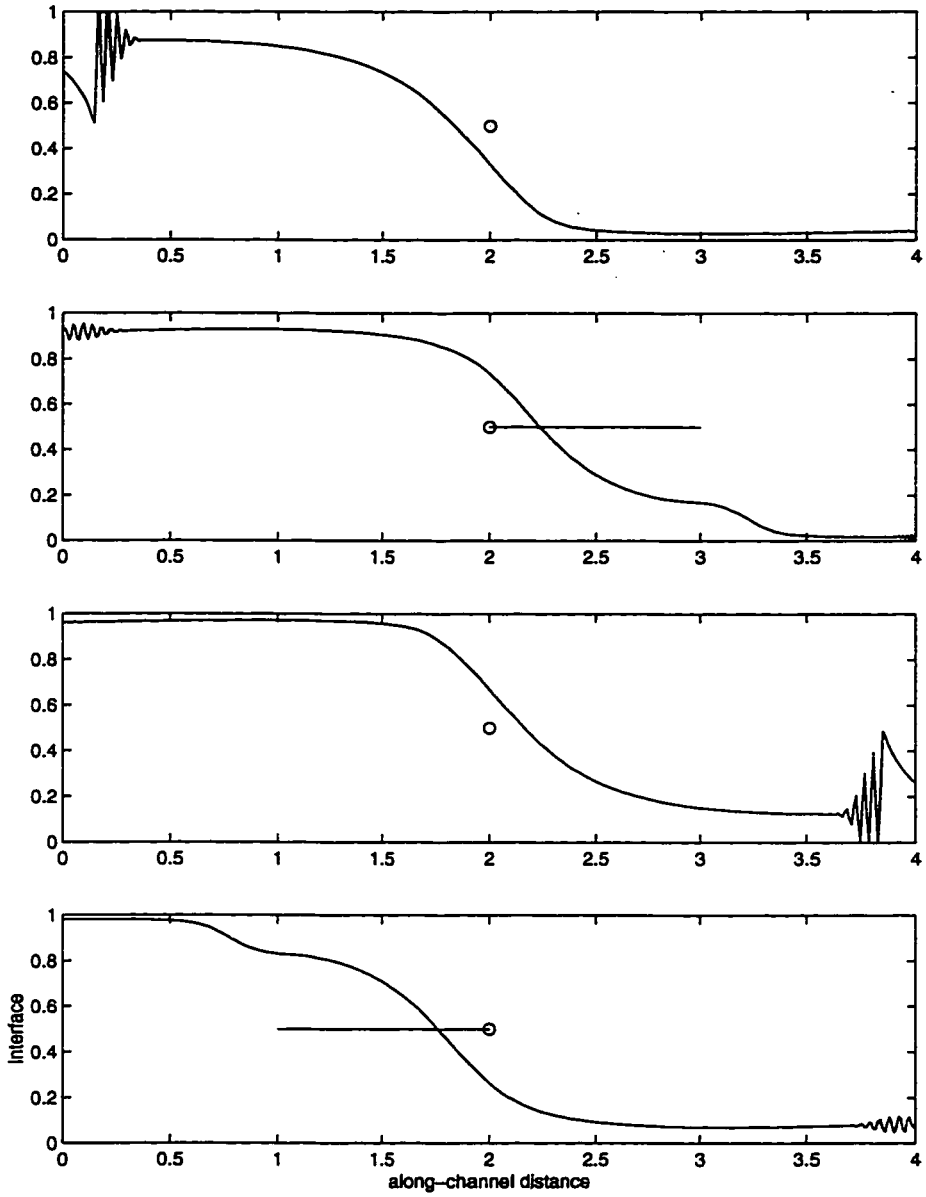

Figure 2.4: Interface positions $h_2(x)$ for 2-layer exchange through a constriction, forced by tidal currents. Subplots represent slack before flood (a), peak flood (b), slack before ebb (c) and peak ebb (d). Note the propagation of a small bore in the interface in response to tidal adjustments, after Helfrich [1995].

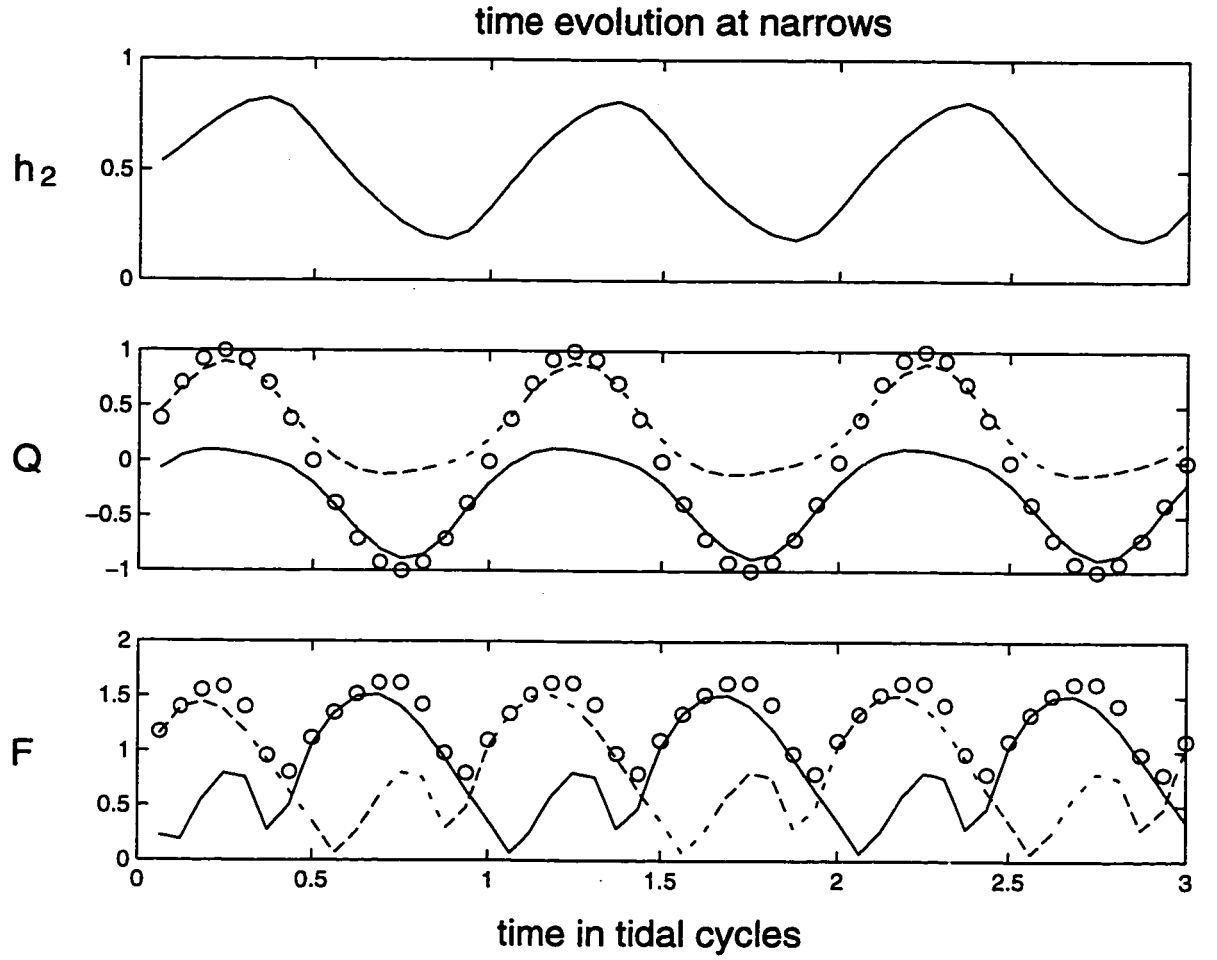

Figure 2.5: Results of two-layer time dependent model; time series plotted at narrows. The layer interface (solid line in a) oscillates vertically in response to imposed tidal barotropic transport, Q (circles in b). Upper layer transport q_1 (solid line in b) dominates on ebb ($Q < 0$), and lower layer transport q_2 dominates on flood (dashed line in b). Layer Froude numbers, F_1 and F_2 are correlated with layer transports. Thus, $F_1 > 1$ on ebb and $F_2 > 1$ on flood, and total Froude number $(F_1^2 + F_2^2)^{1/2}$ is supercritical on both ebb and flood. Model by Helfrich [1995], used with permission.

2.4 Synopsis of Inviscid Two-layer Exchange Theory

The main concepts in two-layer exchange theory are synopsized in figure 2.6. Infinite basins of salt and fresh water are separated by a narrow channel, through which there is a baroclinic exchange flow. In the presence of a channel constriction, the interface between the seaward-moving fresh layer and the landward-moving salt layer takes on a characteristic s-shape (figure 2.6a). Steady barotropic currents distort the interface so that it appears to be advected landward or seaward (figure 2.6b).

Time dependent (tidal) currents cause the interface to move back and forth with time, so an observer at a single location would see the interface rise and fall with the tides (figure 2.6c). At slack water, density driven two-layer estuarine circulation should dominate, giving a two layer flow (surface seaward, bottom landward). This pattern should be seen at the onset of either flood or ebb. Strong tidal currents can overwhelm this circulation, giving unidirectional flows at peak flood and peak ebb. For purely sinusoidal forcing, peak ebb and peak flood currents should be the same strength. In the absence of bottom friction, ebb currents should be strongest near the surface and flood currents should be strongest at the bottom.

This theory is one-dimensional, two-layered, laterally averaged and inviscid. The real world is three-dimensional, multi-layered, laterally varying and subject to both viscous friction and turbulent mixing. The goal of this thesis work is to separate out necessary and un-necessary complications in understanding transport through the Columbia River entrance channel.

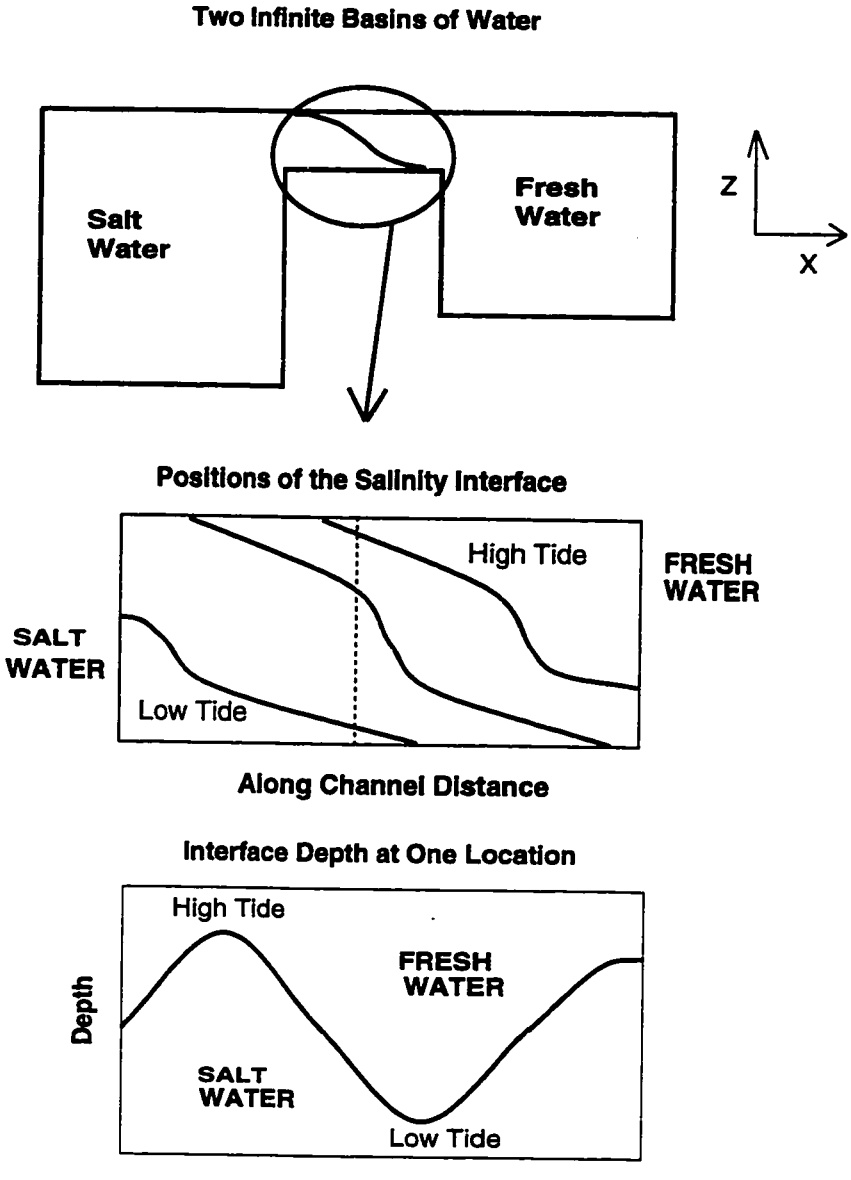

Figure 2.6: Imagine two infinitely large basins, one salt, one fresh, connected by a narrow channel. The salt water slides under the fresh, setting up a two-way exchange in layers separated by an S-shaped interface (a). The interface moves landward and seaward with the flood and ebb currents (b). As seen from one location, the interface rises and falls with the tides (c).

Chapter 3

COMPARISON OF OBSERVATIONS WITH INVISCID THEORY

The inviscid two-layer theory discussed in chapter 2 applies quite well to the Straits of Gibraltar and to some fjords. In the Columbia River entrance channel, circulation is rather more complicated. A lateral constriction and a moderate sill may act as hydraulic controls (figure 1.3), but strong tidal and fluvial currents may overwhelm the controlled flow. The river is relatively shallow, and circulation is strongly influenced by bottom friction and interfacial mixing.

Two data sets of velocity, salinity and temperature were collected in the Columbia River entrance area, to study the effects of time dependent barotropic forcing and vertical mixing on internal hydraulic control. Both salinity and temperature were measured, and density calculated from measurements. The estuary is salt-stratified, so in figures 3.1, 3.3 and 3.5, salinity is shown instead of density. In September and October of 1993, a research cruise was conducted specifically to measure along-channel sections for comparison with the results of internal hydraulic control theory. Time series collected in May of 1992 at Buoy 10 were also studied with the same goal. With both data sets the questions to be answered were "is the flow truly two-layered?" and "do the sill and lateral constrictions act as points of hydraulic control?"

3.1 Data Collection

Both research cruises were made aboard R/V Snowgoose, carrying a Conductivity Temperature Depth (CTD) profiler and an Acoustic Doppler Current Profiler

(ADCP). Position was determined by GPS and the ships orientation by a gyrocompass with a synchronized interface. The Ocean Sensors CTD was deployed at stations located 500- 800 m apart. Averaging of the 100-Hz sensor output was set to yield data at 8 Hz, providing better than 0.2 m vertical resolution in both temperature and salinity. For calculation of the gradient Richardson number, as described below, the CTD data were averaged to 1 m vertical resolution. The R. D. Instruments 1.2 MHz ADCP was in constant operation. One sample, or acoustic ping is an acoustic signal sent by the ADCP and reflected by particles moving with the flow. The water velocity relative to the instrument is calculated from the Doppler shift of the returning signal. The signal reflecting off the bottom measures the speed of the vessel over ground, so the absolute water speed may be calculated. Sixty to 70 acoustic pings are averaged together over a 20 second period to minimize random errors. In a vessel moving at 8 knots, this gives a horizontal resolution of < 100 meters. The data presented here were averaged again over the 5-10 minute duration of each CTD cast. In this area , subject to large vertical shears, the maximum vertical resolution of 1 meter is used. Errors of a few $\text{cm} \cdot \text{s}^{-1}$can be induced by vertical shear, but the water velocities of order $1\ \text{m} \cdot \text{s}^{-1}$were significantly larger than the error.

3.2 Data Reduction

Classical hydraulic control theory assumes two inviscid layers with no mixing between the layers. By contrast, in the Columbia River entrance channel, there is a great deal of turbulent mixing between the layers, and the layer interface is not sharply defined. The resistance of the water column to vertical mixing is measured with (Ri_{gt}).

$$Ri_{gt} = \frac{N^2}{S^2 + N^2} \tag{3.1}$$

where the square of the buoyancy frequency,

$$N^2 = \frac{-g}{\rho_0}\frac{\partial \rho}{\partial z} \tag{3.2}$$

measures vertical stratification and

$$S^2 = (\frac{\partial u}{\partial z})^2 + (\frac{\partial v}{\partial z})^2 \tag{3.3}$$

is the square of the vertical shear. Vertical mixing is driven by the vertical shear and inhibited by density stratification, so a large (Ri_{gt}) indicates a stable flow at a given depth. This formulation of the gradient Richardson number, developed by Geyer [1988], is based on the need to include both mean flow shear and internal wave shear. Mean flow shear is resolvable by the ADCP, but internal wave shear is not. N^2 can be measured at the higher vertical resolution of the CTD measurements, and if equipartition of kinetic and potential energy is assumed, N^2 serves as an estimate of the kinetic energy in a saturated internal wave field. In this formulation, Ri_{gt} varies between zero and one, and the critical value is about 0.3. Above this critical level, turbulence cannot be maintained by the flow. In a truly two-layered system, $(Ri_{gt}) = 0$ at all depths, except right at the interface where $(Ri_{gt}) = 1$. If mixing occurs at the interface, the local stratification is slightly reduced, but the thickness of the interface increases. An estuarine channel generally has a pycnocline of a few meters thickness, in which Ri_{gt} is slightly super-critical.

Calculation of the internal Froude number, G, (2.10) is somewhat problematic. During flood and ebb, the strong barotropic flow overwhelms the baroclinic circulation, and currents in the entrance channel are unidirectional. However, the density distribution is essentially two-layer during most of the tidal cycle, so it seems reasonable to apply the concept of two-layer circulation [Helfrich, 1995]. In our data reduction, we calculated G only when each layer was at least 2 meters thick, thereby avoiding large spikes produced by the pinching off of a layer. Near peak flood, at some places in the channel, both density and velocity were one-layer, and calculation of G would have been meaningless.

There are several possible ways to define the layer interface; for example the depth of maximum stability, measured either by N^2 or Ri_{gt} might be used. In practice, as

both of these quantities are calculated from vertical gradients, there is enough noise in the vertical profiles that concise selection of a maximum is impractical. Inspection of the measured salinity sections (figures 3.1 and 3.3) and time series (figure 3.5) reveals a strong salinity gradient around 22-26 psu. The 22 psu contour also marks the lateral boundaries of the plume pulses in figure 1, so this salinity range may be used to identify the forming plume. To calculate G, we chose the 24 psu isopleth as the layer interface.

3.3 Along-Channel Sections

Observations of velocity and density were made in repeated along-channel crossings of the entrance bar in September and October of 1993. We present here two of the sections, representing conditions at flood onset (figures 3.1 and 3.2) and early flood (figures 3.3 and 3.4).

The horizontal axis of these plots is kilometers landward of the seaward ends of the North and South Entrance Jetties. Buoy 10 is at the crest of a moderate sill (kilometer 1), and Jetty A is a strong lateral constriction at kilometer 3. Strong currents in that area have scoured the deep hole near kilometer 4. Each section was run in a seaward direction and took about two hours, so the western end of each represents a later stage in the tidal cycle than does the eastern end. At peak ebb, when plume-pulse formation is well underway, no observations could be made, due to extremely rough sailing conditions on the bar. Therefore, none of our sections show seaward currents at all depths.

The two salinity sections have some common features (figures 3.1b and 3.3b). In general we find an orderly progression from salt (> 30 psu) to fresh (≈ 8 psu) water in layers separated by an s-shaped interface ($\approx 22 - 26$ psu). The interface is actually a 5-10 meter thick layer due to turbulent mixing, but the basic shape is familiar from hydraulic control theory.

Comparison among all the measured sections shows this interface moving landward on flood and seaward on ebb (see appendix for all sections). The motion of the salinity interface is somewhat jerky, so the leading edge of the salt wedge actually crosses the sill as a series of discrete pulses. These pulses produce a multi-layer intruding water mass (as opposed to a single salt wedge) farther upstream.

The section most resembling the results of two-layer hydraulic control theory was taken an hour after low water (figure 3.1). This circulation is possible only when flood currents oppose the river flow and are of roughly comparable strength. The system is then briefly subject to weak barotropic forcing. The bottom layer is flooding and the surface layer is still ebbing slightly, indicating the end of the plume pulse. The plume lifts off the river bottom just landward of the sill, due to a combination of topographic uplift at the sill and hydraulic control at Jetty A. Both stratification and mixing are apparent directly above the sill (km 1, figure 3.1b). Note the sharp halocline between the 15 and 24 psu contours (about 5 m apart) and the strong mixing indicated by the separation between the 24 and 27 psu contours.

Stability, as measured by Ri_{gt}, was estimated from the above data and plotted as a set of vertical profiles (figure 3.2a). If the system were truly two-layered, Ri_gt would be zero at most depths, and one in a very thin band near mid-depth. Instead, the entire section is essentially critical. Above the sill, where vertical mixing is apparent in the salinity contours, there is a wide band of $Ri_gt > 0.3$, the width of this band indicates enhanced vertical mixing. The 24 psu isopleth was used as a layer interface to calculate the internal Froude number. Consistent with the strong ebb currents landward of the sill, G is strongly supercritical in this area, and critical seaward of the sill (figure 3.2b).

During peak flood, the strong barotropic forcing ($q_{b0} \approx 1$) is expected to drive a one-layer flow [Helfrich, 1995], or a two-layer unidirectional flow with faster currents in the bottom layer [Lawrence, 1990]. The observed current (figure 3.3a, taken four hours after low water) is unidirectional, but strongest at mid-depth. This three-

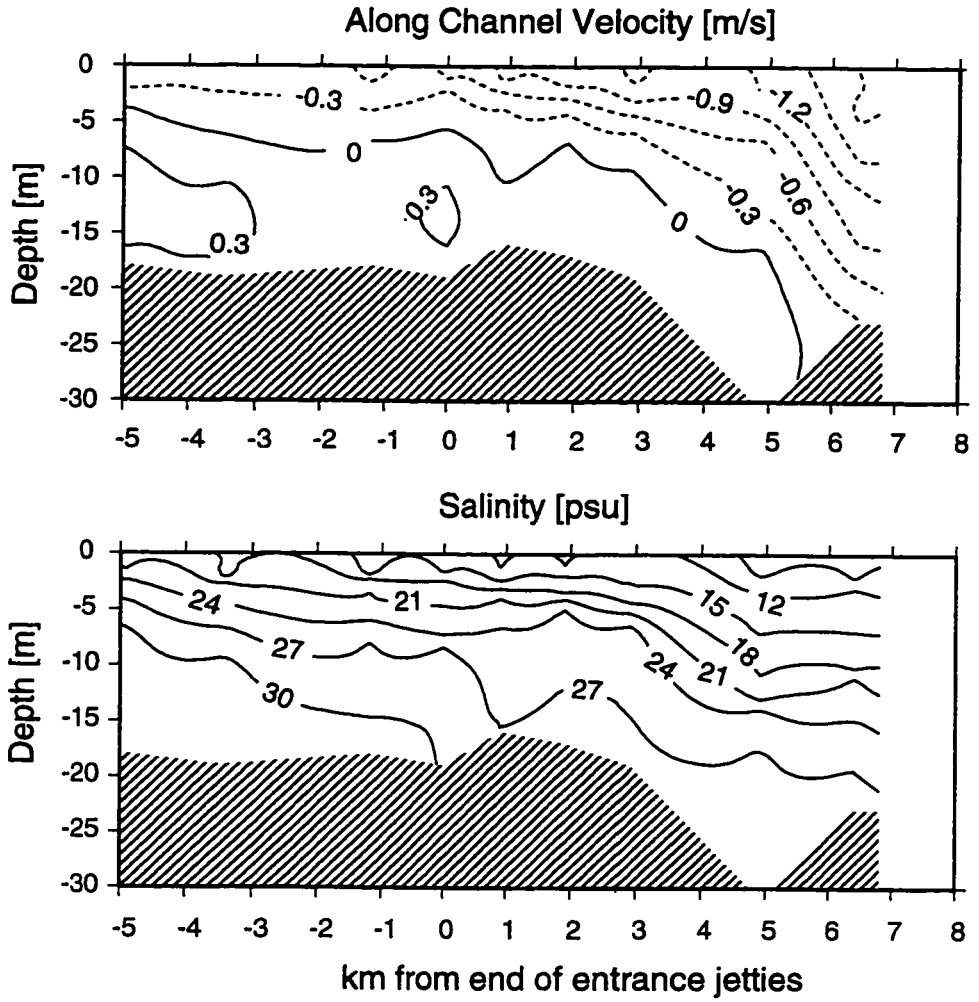

Figure 3.1: Along channel current and salinity section, flood onset. Surface currents are still ebbing (to the left, $u < 0$), and bottom currents are flooding weakly. Salinity increase monotonically toward the bottom.

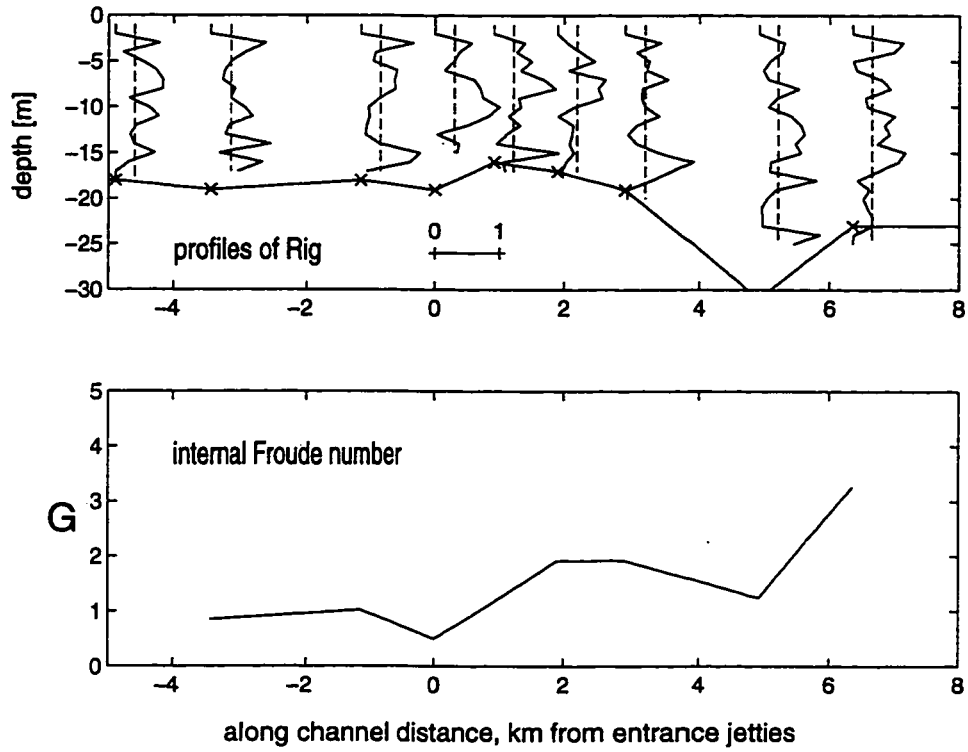

Figure 3.2: Gradient Richardson number and total Froude number flood onset. The dotted lines overlaid on the profiles indicate $Ri_{gt} = 0.3$, or critical stability – most of the section is stable. Total internal Froude number F is supercritical near the landward end where ebb currents are strongest.

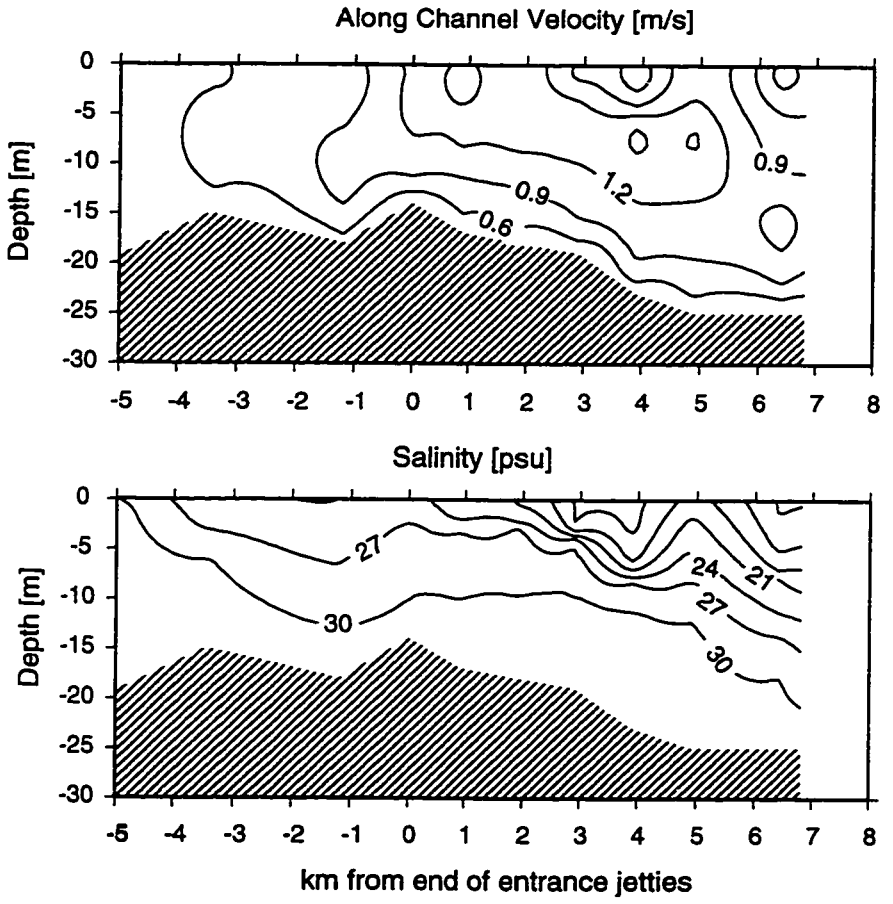

Figure 3.3: Along channel current and salinity section, early flood. Salinity still increases monotonically toward the bottom, but currents are strongest (to the right, $u > 0$) at mid depth.

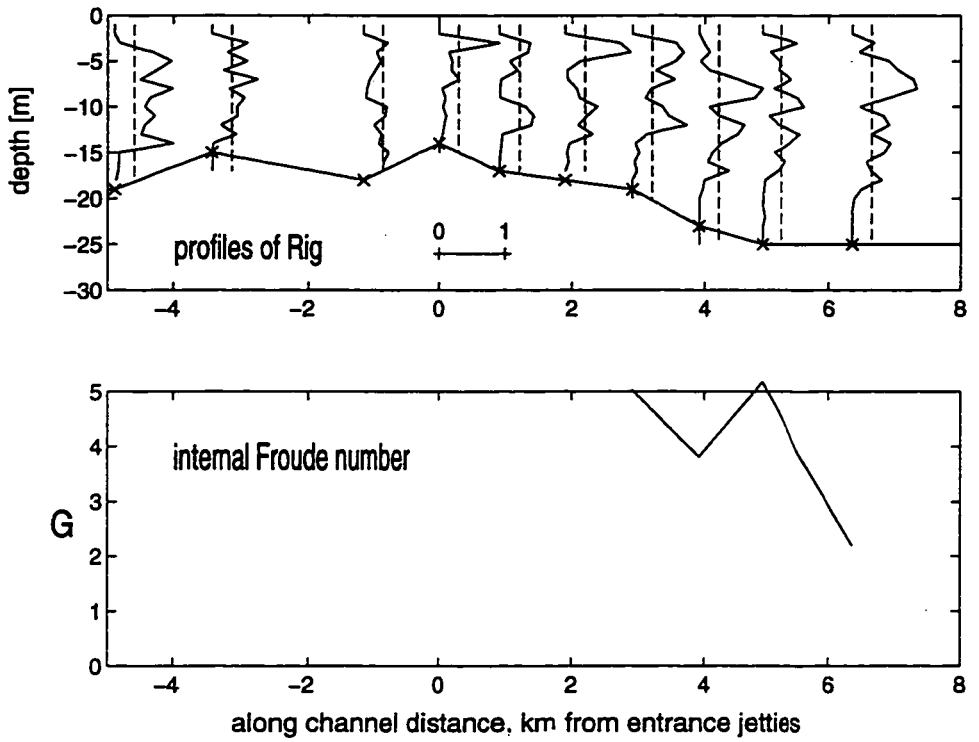

Figure 3.4: Gradient Richardson number and total Froude number, early flood. There is a mid-depth band of $Ri_g t > 0.3$, representing a thick pycnocline. F is supercritical everywhere in this section.

layer flow is due to a combination of baroclinic forcing (which increases with depth), turbulent mixing at the original layer interface and friction at the river bottom. The mixing creates a thick interfacial layer, and bottom friction retards the flood current, forcing the maximum current up into the interfacial layer [Geyer, 1985, 1988]. Note that the region of currents > 1.2 ms-1 (figure 3.3a) roughly coincides with a salinity band of 18-30 psu (figure 3.3b). The mid-depth current accelerates upon passing the slight constriction of the entrance jetties, and accelerates further over the sill. The current then dives over the sill and reaches its maximum velocity in the constriction at Jetty A. These effects, although not directly predicted by hydraulic control theory, demonstrate the importance of the constrictions.

The salinity section (figure 3.3b) suggests the presence of a blocked plunge line related to the the strong inflow [Largier, 1992]. Such fronts were observed during this section, being advected with the flood currents. The presence of salmon sport fishermen in the area indicates the convergence of nutrients, plankton and salmon on the fronts. Above the sill, the 18-24 psu salinity contours all come to the surface within a two kilometer long region. Two-layer flow is thus seen only landward of the sill, where G is strongly supercritical (figure 3.4b). Profiles of Ri_{gt} measured at peak flood (figure 3.4a) indicate slightly higher stability than at flood onset. There appears to be a stable mid-depth layer overlying well-mixed water for all profiles landward of the sill. The stable layer is somewhat thinner over the sill, which may indicate topographically enhanced mixing.

3.4 Time Series Measurements

Two-layer circulation in an estuarine channel can be predicted under sinusoidal tidal forcing and in the absence of friction [Helfrich, 1995]. At slack water, estuarine baroclinic circulation should dominate, giving a two layer flow (surface seaward, bottom landward) at the onset of either flood or ebb. Strong tidal currents can overwhelm

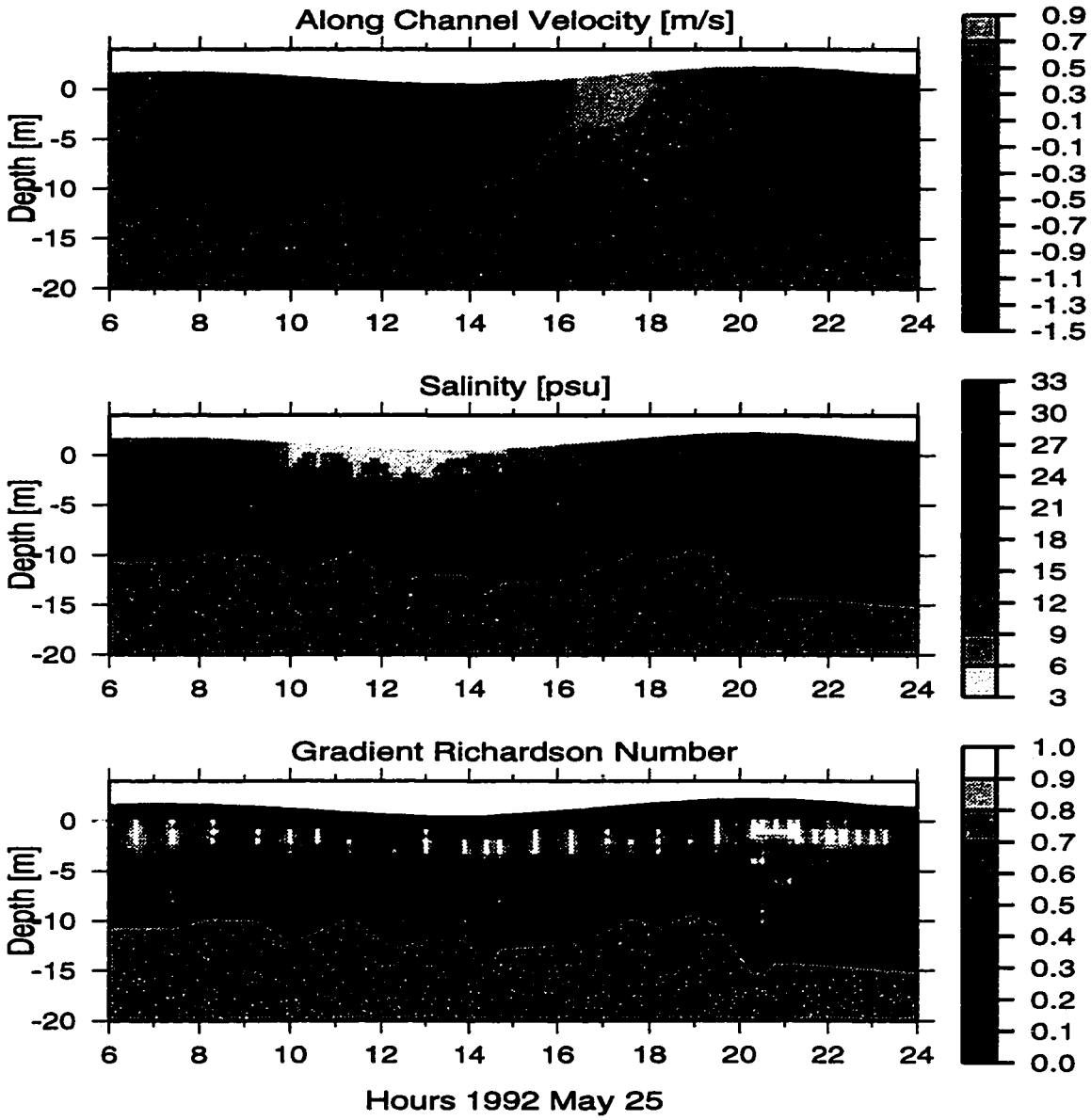

Figure 3.5: Time series of u, s, and Ri_{gt}

this circulation, giving unidirectional flows at peak flood and peak ebb. For sinusoidal forcing, peak ebb and peak flood currents should be the same strength. In the absence of bottom friction, ebb currents should be strongest near the surface and flood currents should be strongest at the bottom. The fresh water advected seaward on ebb is expected to thicken the surface layer, while the dense flood current should thicken the lower layer. In the absence of interfacial mixing, each layer should maintain a uniform density (Ri_{gt} nearly zero) and the interface should be quite stable (Ri_{gt} nearly one).

Time series of salinity and velocity were measured on May 25, 1992 at four stations near Buoy 10, just landward of the crest of the sill (figure 1.3). This is the site of both intensified flood currents and ebb plume lift-off, and is therefore a good place to study intra-tidal variability. We were able to measure time series varying in length from 12 to 18 hours or 1/2 to 3/4 of a diurnal tidal cycle. The longest time series was collected at station D, near the south side of the channel.

The measured along-channel currents at station D (figure 3.5a) show the effect of both strong river forcing and bottom friction. Peak ebb currents (1200 PST and 2400 PST) are about 50 percent stronger than peak flood currents (1800 PST). Ebb currents are stronger in the upper layer, but are significant at all depths. Ebb onset is sudden and almost simultaneous throughout the water column, creating unidirectional currents instead of the predicted two-layer flow (0900 PST and 2100 PST). Both the strength and sudden onset of the ebb currents are due to the strong river flow, which enhances the ebb current but opposes the flood. In contrast, flood onset takes over an hour to propagate from the bed to the surface. The flood current, being driven by denser oceanic waters, starts in the lower layer (1400 PST). As described above, bottom friction impedes lower layer flow, pushing the maximum flood current upward with time. The time series shows the full vertical progression of the flood current.

The salinity time series (figure 3.5b) and the Ri_{gt} time series (3.5c) show evidence of interfacial mixing. The salinity interface, which moves up and down tidally, is about 5-10 m thick, depending on the stage of the tide. This interfacial layer coincides with

a persistent stable layer in the Ri_{gt} time series. Due to a reduction in vertical shear, the stable layer thickens to fill the water column at slack water. Thus the system alternates between stable and well mixed on a quarter-diurnal period. This combination of quarter and semi diurnal signals in Ri_{gt} indicates internal tidal asymmetry and lies outside the assumptions of hydraulic control theory [Jay and Musiak, 1996].

Both the along channel section at peak flood (figure 3.3a) and the time series (figure 3.5a) suggest the importance of bottom friction and interfacial mixing to along-channel transport. In the classical two-layer model, most flood transport is in the saltier lower layer, so significant amounts of salt are advected landward. The observed transport is concentrated higher in the water column and carries less salt. Thus the estuary should be significantly fresher than would be predicted from a two-layer model with the same exchange volume.

3.5 Lateral Variations

In our low-order comparison of observations and the predictions of hydraulic control theory, we ignored lateral variations and examined only the effects of turbulent mixing and time varying barotropic currents. However, currents in the Columbia River entrance also vary laterally due to channel curvature and other topographic effects. The time series discussed above was measured south of mid-channel, near the inside edge of the curve (station D). Salinity and velocity time series measured on the north side of the same channel section (station A) were qualitatively similar to those from station D, but represent different physical circumstances. Station D is near mid-channel, where the water is deep and the currents fast. Station A is in much shallower water, and the currents are slower. These differences are clearly seen in a comparison between internal Froude number time series calculated at the two stations (figure 3.6). For both measured time series, there is a clear pattern of long supercritical periods during ebb and flood, interspersed with brief subcritical periods

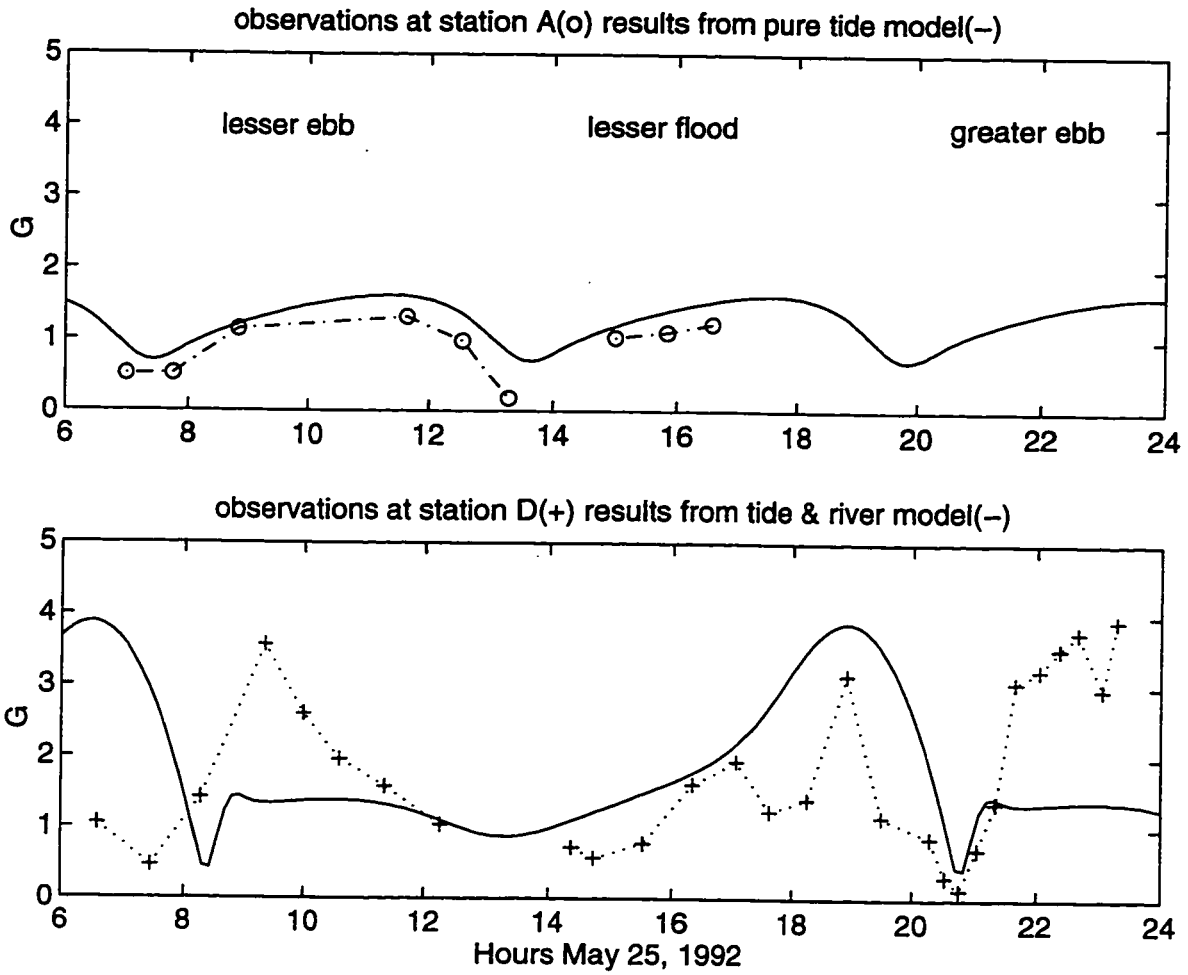

Figure 3.6: Time series of total internal froude number at stations A and D

at slack water. At station A, G varies between 0.5 near slack water and 1.5 at peak flood and ebb (figure 3.6a). At station D, the amplitude of the supercritical Froude numbers varies with tidal period, being about 3 on lesser ebb, 2 on flood and up to 4 on greater ebb (figure 3.6b). The dramatic difference between the two time series is due to both spatial and temporal variations in barotropic forcing strength (which includes the effect of depth). These temporal variations, due to the strong river flow and unequal semidiurnal tides, have a significant effect on local dynamics.

Compare the two measured time series of G with results from Helfrich's [1995] fric-

tionless model. Our observations were made about 1 km seaward of the constriction, and should be qualitatively comparable with model predictions of G at the constriction. Model input parameters are: time dependence γ, tidal forcing strength q_{b0} and mean current q_m (*e.g.* a river current). The magnitude of γ depends on the definition of the length scale L; it has a precise mathematical definition in a model, whereas in a real channel, L must be estimated from topography. In this section of the channel, $\gamma \approx 4-6$, which is comparable with Helfrich's choice of $\gamma = 4$. Total forcing strength can be expressed (Helfrich, personal communication) as

$$q_b(t) = q_{b0}\sin(\omega t) + q_m \tag{3.4}$$

In a real channel, q_{b0} and q_m are estimated from the tidal current speed and the total water depth (2.14). At station A, $q_{b0} \approx 0.85$ and $q_m \approx 0.15$, whereas at station D, $q_{b0} \approx 1.2$ and $q_m \approx 0.2$. Measured G at these stations are compared with two model runs. Helfrichs original model used $\gamma = 4$ and $q_{b0} = 1.0$, parameters which approximate the average tidal barotropic forcing in the Columbia River entrance, but do not include the river currents. At our request, Dr. Helfrich made a special model run using the same tidal forcing as above, with the addition of $q_m = 0.3$ to represent strong river flow.

Although $q_{b0} \approx 1$ at both stations, indicating strong barotropic forcing, a subtle difference in forcing can lead to significant differences in G. If $q_b > 1$ at any time, the barotropic currents can overcome the baroclinic forcing, so that one layer is pinched off and the net flow becomes unidirectional. As h_i in the opposing layer becomes very small, the layer Froude number

$$\mathrm{F_i} = \frac{u_i}{\sqrt{g' h_i}} \tag{3.5}$$

becomes quite large. This effect is apparent in the model results (figure 3.6b) at 0700 hours and 1900 hours, shortly after peak flood.

Comparisons between model and observation are shown in figure 3.6. The measured G time series from station A closely resembles the model results without river

forcing (figure 3.6a), whereas the observations at station D are more comparable with the model results including river currents (figure 3.6b). This difference shows the importance of lateral variations in along-channel circulation. There are also significant differences between the observations at station D and the river-forced model results, which indicate the complementary effects of current speed and layer depth in calculating the layer Froude numbers. The large observed peaks in G at station D (+ signs) are attributed to the strength of the river-enhanced peak ebb current (large u_1 – large F_1). The modeled G time series (solid line) has peaks with amplitudes close to those measured at station D, but the maximum theoretical G leads peak ebb by about 3 hours. These maxima occur at the end of flood, as the bottom layer is pinched off by the oncoming ebb (small h_2 – large F_2). This pinching-off may be tempered by the addition of bottom friction (Chapter 5). Both observations and model results are valid, but slight differences in the method of calculating G produce significantly different results.

In summary, comparison between observations and model results reveals three significant differences. First, the lack of mixing effects gives an incorrect prediction of the flood velocity profile, which would lead to an over-estimate of landward salt transport. Second, significant lateral variations cannot be recreated by a two-dimensional model. However, it might be possible to model the internal hydraulic properties of each streamline individually, and present them in parallel to approximate the three-dimensional flow. Third, even in very similar flows, subtle differences in the method of calculating G may produce different views of the internal hydraulics. This effect does not imply a limitation in the usefulness of a model, but only a caution about interpretation.

3.6 Conclusions

The physics of plume formation in the Columbia River entrance can be partially explained in terms of hydraulic control theory. The basic importance of sills and constrictions is clear, as indicated by the ebb plume lift off and flood current intensification between the sill and constriction. The time dependent hydraulic control model of Helfrich [1995] predicts qualitative features of the flow, but there are some significant quantitative differences between theory and observation.

The presence of a river current causes the following effects: Ebb is stronger and longer in duration than flood. Ebb onset is sudden and simultaneous at all depths (one-layer flow). Two-layer flow is observed only at the start of flood.

Bottom friction and turbulent mixing cause the following effects: The layer interface is of finite thickness (> 5m) at all stages of the tide. The interface thickness increases to the water depth (≈ 20m) at slack water and decreases at peak flood and peak ebb; mixing varies at twice the tidal frequency. Bottom friction impedes flood currents in the lower layer, so flood mass transport occurs at mid-depth or above. Therefore, flood currents should advect less salt landward than would be predicted from a two-layer model.

These are the observed lateral variations in along-channel circulation: Time series of salinity and velocity measured at opposite sides of the channel are qualitatively similar. Observed time series of internal Froude number vary laterally by a factor of 3 at peak ebb, because of lateral variations in depth and subtle lateral variations in velocity and density. Measured G at the north side of the channel appears to be affected only by tides. Observed G on the south side of the channel has large peaks attributed to the strength of the river-enhanced ebb current.

Chapter 4

FRICTION AND MIXING IN LAYERED FLOWS

Friction and vertical mixing in layered flows is a complex subject that has been studied using a wide variety of field and laboratory observations and numerical models of varying dimension. Many of the observations seem, at first glance, unrelated to each other. Laboratory experiments reveal beautiful Kelvin-Helmholtz instabilities, while field observations provide vertical current profiles and measures of the pycnocline thickness. The job of the estuarine modeler is to connect these disparate observations. This task has generally been attempted using detailed turbulent closure models, but I suggest an alternate approach, using two and three-layer models with parameterized vertical entrainment between the layers. These models are developed in chapters 5 and 6.

One purpose of the present chapter is to find estimates of interfacial mixing and bottom friction for these models. Laboratory studies (§4.2) demonstrate the link between vertical instabilities and interfacial entrainment and provide a parameterization of entrainment rates. Field observations (§4.3) reveal the varying thickness of the density interface between two moving layers and suggest a means to estimate that thickness. An analytic study (§4.4) shows the effects of bottom friction on a moving layer under an inactive layer.

The second purpose of this chapter is to explain some observations in the Columbia River (§4.5) by comparison with existing models of the effects of vertical mixing. These models use a second order turbulent closure scheme [Mellor and Yamada, 1982] and simulate along-channel circulation quite well, but they require a great deal of computer time. A three-layer model may be able to simulate interesting features of

circulation more efficiently.

4.1 Density Currents and Exchange Flows

The best known types of layered flow are surface density currents, bottom density currents and exchange flows (figure 4.1). These essentially baroclinic flows have been thoroughly studied in laboratories and models, and aid our understanding of estuarine circulation. However, strong barotropic currents in estuaries may overwhelm the baroclinic circulation, so that the observed circulation is layered but unidirectional. In a tidal estuary, surface and bottom density currents and baroclinic exchange flows may be observed only for very brief periods near slack water.

A surface density current (figure 4.1a) is formed when lower density water is released near the surface of a basin of denser water. The lighter water propagates away from its point of origin; the current develops a thick head, pushing a sharp front and followed by a thinner more diffuse tail [Simpson, 1972]. Strong entrainment just behind the head maintains this characteristic shape. A bottom density current (figure 4.1b) is formed when denser water is released near the bottom of a basin of lighter water; it closely resembles a surface density current, but is affected by bottom friction as well as interfacial mixing. In an estuary with moderate tidal and fluvial currents, early ebb circulation resembles a surface density current and early flood circulation resembles a bottom density current. Only the flood current is strongly affected by bottom friction, so there is an ebb/flood asymmetry in internal circulation patterns.

When two infinite basins of dense (saline) and less dense (fresh) water are joined by a narrow channel, the surface density current from the fresh basin slides over the bottom density current from the salt basin. This process may continue indefinitely, and the steady circulation is a two-layer exchange flow. The heads of the density currents are transient, and therefore not visible in figure 4.1c. The behavior of exchange flows in the presence of channel constrictions is predicted by internal hydraulic control

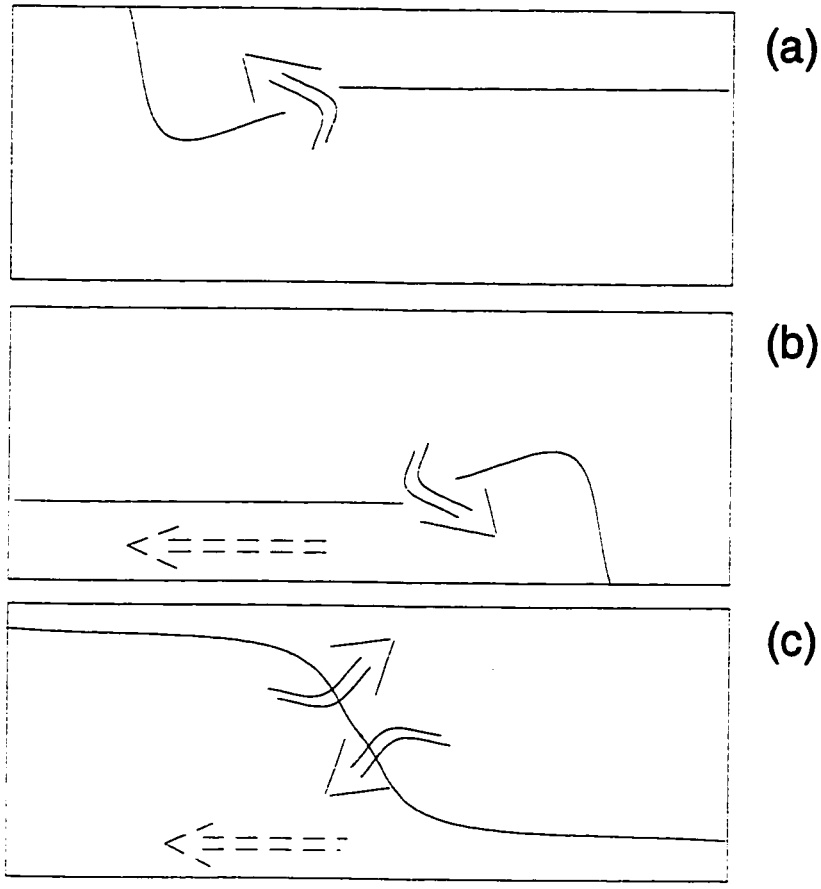

Figure 4.1: Turbulent effects in three types of two-layer flow. The surface density current (a) propagates right to left over a deep, nearly motionless layer. It entrains water behind its head (curved arrow) and is unaffected by bottom friction. The bottom density current (b) propagates left to right underneath a motionless surface layer. It entrains water (curved arrow) and is retarded by bottom friction (straight arrow). The exchange flow (c) is a combination of surface and bottom currents. There is two-way entrainment between the layers (curved arrows) and the bottom layer is retarded frictionally (straight arrow).

theory [Armi and Farmer, 1986; Farmer and Armi, 1986]. This theory assumes inviscid flow so Bernoulli energy is conserved, but geophysical exchange flows on many scales are affected by bottom friction and by interfacial mixing. Armi and Farmer [1986] extended the theory of exchange flows to include steady barotropic currents, so their results approximate the peak flood and peak ebb stages of the tidal cycle.

4.2 Interfacial Instabilities and Entrainment

Laboratory experiments of density currents reveal both the details of interfacial instabilities, and the overall growth rate of the currents. The measured growth rate may be used to parameterize the growth of density currents in a numerical model.

Several laboratory studies of interfacial instabilities in stratified flows have been published. In nearly laminar flows (low Reynold's number) instabilities develop as shown schematically in figure 4.2 [Zhu and Lawrence, 1996]. This figure shows a salt wedge advancing left to right over a sill. Upstream of the sill (to the left), shears are relatively weak, and cusp-like Holmboe instabilities propagate in both directions along the interface. These Holmboe instabilities are not seen in estuaries, where the Reynold's number is much higher. As the salt layer accelerates over the sill, it develops strong Kelvin-Helmholtz instabilities, filling up to 1/2 of the water column [Lawrence, 1990; Garcia and Parsons, 1996]; these billows overturn into a large roll at the head of the salt intrusion. Pawlak and Armi [1996] observed similar patterns downstream of a lateral channel constriction; the instabilities may be triggered by any topographic disturbance to the flow. In experiments with a surface density current, Yonemitsu *et al.* [1996] saw the same pattern as in figure 4.2 but upside-down. Echo sounder plots from the estuaries of the Columbia and Fraser Rivers also reveal strong Kelvin-Helmholtz billows generated by lateral constrictions [Geyer and Smith, 1987; Jay and Musiak, 1996].

Pawlak and Armi [1996] noted the effect of sidewall friction on the instabilities

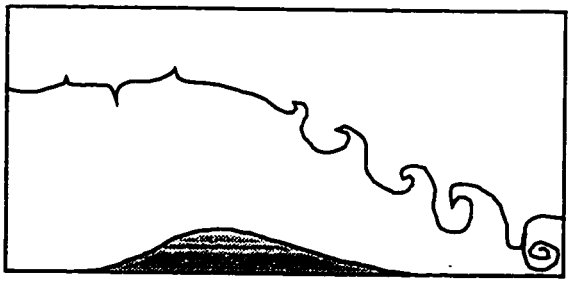

Figure 4.2: Interfacial instabilities in a salt wedge flow, after Zhu and Lawrence [1996]. The salt wedge is moving left to right and accelerates over the sill. Small points are Holmboe instabilities, which propagate in both directions along the interface. Large curls are Kelvin-Helmholtz instabilities, which cause mixing between the salt and fresh water.

described above, using a dense current propagating through a lateral constriction in the laboratory. The flow became supercritical and unstable downstream of the narrows, as measured by total internal Froude number G^2 and the stability Froude number F_Δ^2:

$$G^2 = \frac{u_1^2}{g'h_1} + \frac{u_2^2}{g'h_2} > 1 \tag{4.1}$$

$$F_\Delta^2 = \frac{\Delta u^2}{g'H} > 1 \tag{4.2}$$

where u_i are layer speeds, h_i are layer thicknesses and g' is reduced gravity. The vertical shear between the layers is Δu, and the total water depth is H. The measured values of F_Δ^2 and G^2 increased downstream of the narrows, but significantly less than predicted by inviscid theory. Pawlak and Armi [1996] attribute the difference to sidewall friction, which is less significant in geophysical flows.

A model of estuarine transport cannot resolve the details of these instabilities, so a modeler needs a way to parameterize their effects. In most laboratory experiments, the density current is thin, fast moving, and more turbulent than the ambient water. When the Kelvin-Helmholtz billows collapse, they entrain mass into the turbulent layer [Grubert, 1989], which grows noticeably thicker as it moves. For a surprising variety of geophysical flows, the rate of entrainment is proportional to the mean speed of the flow. This "entrainment hypothesis" [Turner, 1986] makes it possible to

model the growth of a density current without considering the details of interfacial turbulence.

Density currents observed in laboratory experiments tend to grow linearly with time [Hacker *et al.*, 1996], at a rate which depends on a Reynold's number, a Richardson number, or both. In some density currents, entrainment is restricted to the region of Kelvin-Helmholtz billows just behind the head of the current [Simpson, 1972; Hacker *et al.*, 1996]. However, the current may also grow by entrainment along its whole length. For example, Ellison and Turner [1959] studied a density current that traveled down a sloping floor under the influence of gravity (figure 4.3). The current grew by turbulent entrainment of the ambient water, and its growth rate was proportional to its speed.

$$\frac{\partial h}{\partial t} = U \cdot E = U \cdot \frac{0.08 - 0.1 Ri_o}{1 + 5 Ri_o}, Ri_o < 0.8 \tag{4.3}$$

where h is the thickness of the gravity current at a given location, and U is its speed relative to the stationary ambient fluid [Turner, 1986]. The bulk Richardson number for the density current is Ri_o

$$Ri_o = \frac{g' h \cos\theta}{U^2} \tag{4.4}$$

The Richardson number is essentially the ratio of potential energy gained by lifting a parcel of water to the kinetic energy available to lift the parcel. A large Ri_o indicates a stable water column, in which vertical motion is inhibited. In this experiment, vertical mixing and entrainment stop at a critical Richardson number of 0.8. The scaling factor, E, varies between 0 and 0.08, indicating gradual growth of the density current. This entrainment velocity both increases the thickness and decreases the density of the density current.

Price and Baringer [1994] used equation 4.3 to model entrainment into dense outflows from the Mediterranean Sea, the Norwegian-Greenland Sea and the Weddell Sea. Although the densest source water comes from the Mediterranean, the oceanic bottom water formed by the Mediterranean outflow is significantly less dense than

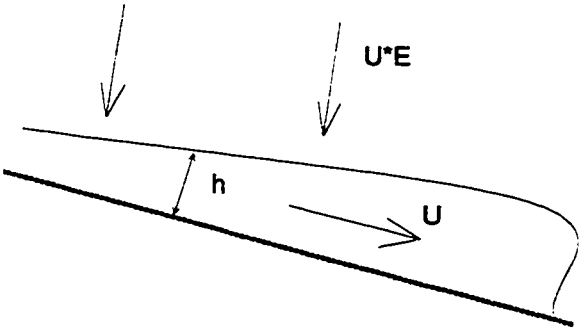

Figure 4.3: Gravity driven density current under a deep stationary layer, after Ellison and Turner [1959]. The current grows by entrainment of ambient water, and $\frac{\partial h}{\partial t} = U \cdot E$.

the bottom water formed from the polar outflows. The final density of the bottom water is determined both by the density of the original outflows and by the density of the ambient water, and eastern Atlantic water is less dense than northern Atlantic water. While modeling the different outflows, Price and Baringer [1994] found that mixing is strongly correlated with bottom slope, and thus concentrated in areas like the shelf break. Their model results correlated well with observations, implying that equation 4.3 is consistent with geophysical flows. This parameterization may also be appropriate for my new model of vertical mixing in a tidally-driven exchange flow.

4.3 Pycnocline Thickness

Field observations of the estuarine pycnocline (region of strong vertical density gradients) reveal that it moves vertically and changes thickness over the tidal cycle. The relationship between observed pycnocline thickness and vertical shear may be used to estimate pycnocline thickness from a two-layer model.

Turbulent flows entrain still water. In laboratory experiments, a turbulent density current grows by entraining ambient water. In estuarine flows, shear instabilities grow on the interface between the landward-moving salt layer and the seaward-moving fresh layer. This mid-depth band of turbulence entrains water from above and be-

low, reducing vertical gradients in velocity and density and forming a finite-thickness interface between the layers. The growth and characteristics of the density interface (pycnocline) have been extensively studied in the field.

On May 25, 1992, a set of measurements were made in the Columbia River entrance channel near Buoy 10 (figure 1.3). Field work may be done in this area only during neap tide, as spring tides are too violent for small vessel operations. One set of four time series extends over a full 12-hour tidal cycle; revealing both spatial and temporal variations in pycnocline thickness. Salinity contours are used to identify the pycnocline; the 8-28 psu contours, in intervals of 4 psu, are plotted in the top row of figure 4.4. The pycnocline is the region of strong vertical gradients in salinity which lies above the 24 psu salinity contours. It grows by 4 to 8 meters over a 6-hour ebb, so the growth rate is of order 10^{-4} m $\cdot$ s^{-1}. Its maximum thickness is about 1/2 of the water depth [Cudaback and Jay, 1996].

The second row of 4.4 shows average along-channel speed above and below the 22 psu contour (solid and dashed lines, respectively); peak ebb (negative currents) is around 1200 hours and peak flood (positive currents) is near 1800 hours. On ebb, seaward currents in the upper layer are much faster than currents in the lower layer ($u_2 < u_1 - 0.4$). Early in flood (1500 hours), landward currents are faster in the bottom layer ($u_2 \approx u_1 + 0.2$), but peak flood currents are strongest at the surface ($u_1 > u_2 + 0.2$). This vertical progression of the flood currents is due to bottom friction.

The pycnocline thickness and vertical shear may be used to estimate the stability of the water column. The gradient Richardson number Ri_g, discussed in chapter 3, is the ratio of the vertical density gradient to the square of the vertical shear, which we can measure on a sub-meter scale. The bulk Richardson number Ri_b relates the same quantities on the scale of the whole water column; large values of Ri_b indicate a stable water column. It is formulated as follows: imagine two layers, each of uniform density, in which currents vary along-channel, but not vertically. Initially, the gradient

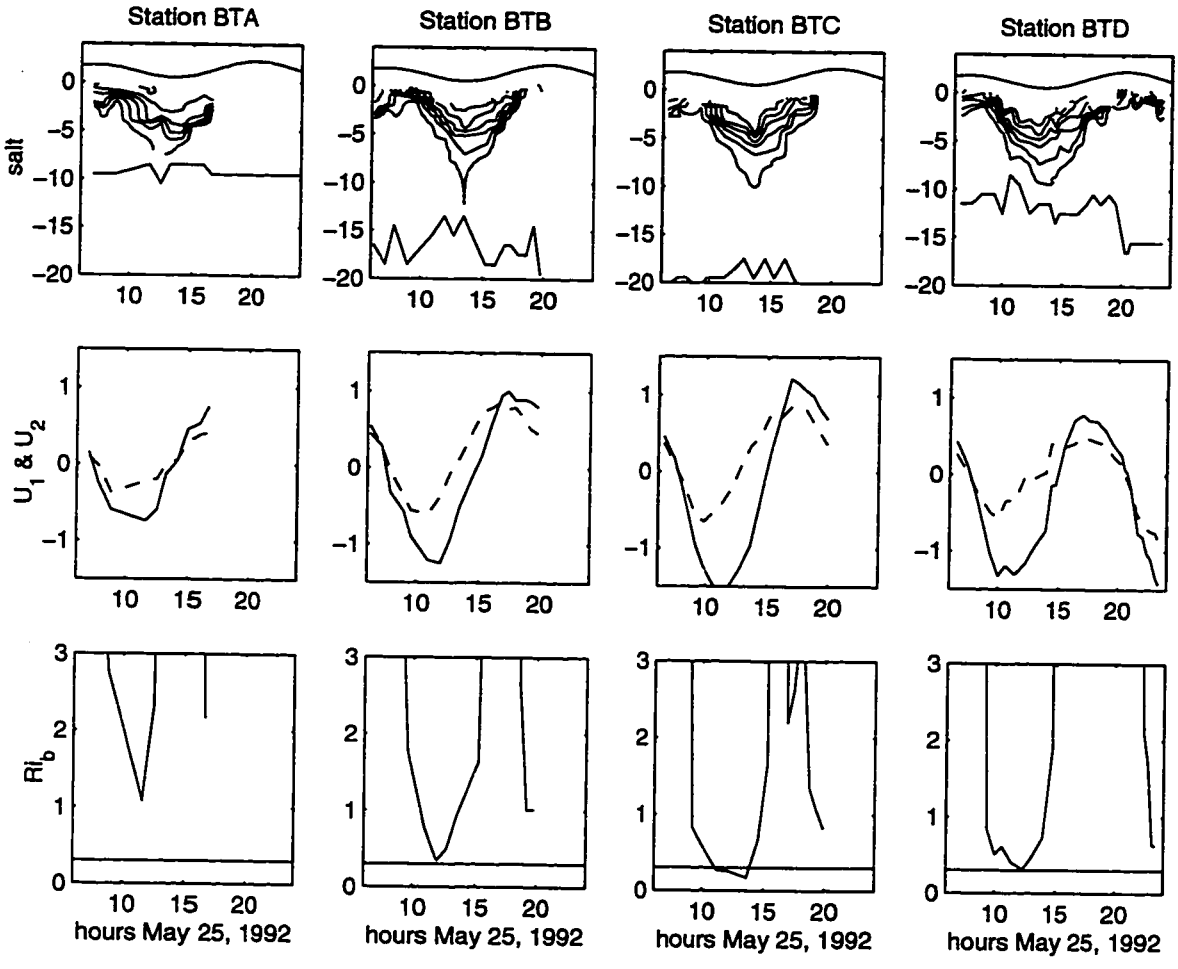

Figure 4.4: Observed pycnocline in the CR entrance channel over a tidal cycle. First row: 8-28 psu salinity contours (in steps of 4 psu) show that the pycnocline grows rapidly on ebb and thins on flood. Second row: layer-averaged currents above and below the 22 psu isohaline, positive currents are landward. Upper layer currents (u_1, solid line) are stronger than lower layer currents (u_2, dashed line) at both peak flood and peak ebb. For a brief period on late flood, $u_2 > u_1$. Third row: bulk Richardson number calculated from pycnocline thickness and vertical shear. Ri_b is critical on ebb, strongly supercritical on flood.

Richardson number

$$Ri_g = \left(\frac{-g}{\rho_0}\frac{\partial \rho}{\partial z}\right) / \left(\frac{\partial u}{\partial z}\right)^2 \tag{4.5}$$

is zero in each layer, and infinite at the (infinitely thin) layer interface. Shear induced turbulent mixing creates Kelvin-Helmholtz instabilities at the interface, which eventually form a stable pycnocline of finite thickness. Ri_g is now zero in each of the two original layers, and finite in the mixing zone. The density and velocity in the pycnocline tend to vary linearly with depth [Geyer and Smith, 1987], so Ri_g is constant throughout the pycnocline, and the bulk Richardson number, Ri_b, may be expressed thus:

$$Ri_g \approx \frac{g\delta\rho}{\rho_0}\frac{\delta z}{(\delta u)^2} = \frac{g'\delta z}{(\delta u)^2} = Ri_b \tag{4.6}$$

Mixing is driven by vertical shear and inhibited by the vertical density gradient; these factors balance at a critical Richardson number $Ri_b \approx Ri_{\text{crit}}$ but the exact value of Ri_{crit} is under debate.

Critical values of Ri_b have been measured both in the lab and the field, with values between 0.25 and 1. In a laboratory experiment, Koop and Browand [1978] noted that shear-induced vortices in a stratified flow stopped growing when Ri_b reached 0.3; this value has been used in some numerical models [Helfrich, 1995; Monismith and Fong, 1996]. Geyer and Smith [1987] found $Ri_{\text{crit}} = 0.25 - 0.33$ in the Fraser River, British Columbia. This value applies only to ebb, when vertical shear-induced mixing is strongest, and near a lateral constriction which may enhance mixing. As the Fraser has very similar dynamics to the Columbia River, we expect to observe similar mixing characteristics. In the Hudson River, where tides and currents are somewhat weaker, Peters [1997] measured changes in vertical mixing over a spring-neap tidal cycle. Spring tides caused stronger vertical mixing, so measured gradient Richardson numbers in the pycnocline were around 0.25 on spring, and closer to 1 on neap.

Observations in the Columbia River entrance channel reveal strong tidal variations in Ri_b (figure 4.4, bottom row). Strong vertical mixing causes the pycnocline to grow

rapidly on ebb, and $Ri_b < 1$. As $Ri_b \approx 0.3$ only briefly at peak ebb, the critical Richardson number must be $Ri_{\text{crit}} \approx 1$ in this river. On flood, the vertical shear between the layers is greatly reduced and there is little or no vertical mixing, so Ri_b is essentially infinite.

The bulk Richardson number may be used to estimate pycnocline thickness δz from a two-layer model. If Ri_{crit} is known, equation 4.6 may be rearranged thus:

$$\delta z \approx \frac{Ri_{\text{crit}}(\delta u)^2}{g'} \tag{4.7}$$

For most estuarine flows, strong stratification may be assumed, so $g' = g\delta\rho/\rho_0 \approx 0.1$. Surface currents of 1-2 $\text{m}\cdot\text{s}^{-1}$and a stationary bottom layer give $\delta u \approx 1\ \text{m}\cdot\text{s}^{-1}$. During ebb in the Columbia River, $Ri_{\text{crit}} \approx 1$, so pycnocline thickness $\delta z \approx 10$ m. Weaker initial stratification or higher shear results in a thicker pycnocline. This method may be used to estimate pycnocline thickness on ebb; with some larger assumed value of Ri_b, flood thickness may also be approximated.

Monismith and Fong [1996] created a one-dimensional model of vertical mixing in stratified tidal flows using the Mellor-Yamada turbulent closure scheme, and also used equation 4.7 to estimate pycnocline thickness. They assumed that the bottom layer was well mixed, and that the upper layer was only intermittently turbulent. They found that bottom friction increased the shear between the layers and aided the growth of the pycnocline. Shear between the layers was strongest during strong flood and ebb currents, so the pycnocline grew thicker and thinner twice during the tidal cycle. This result is consistent with observations. However, the lower layer also got deeper over several tidal cycles, due to irreversible mixing at the pycnocline. According to this model, the whole water column would eventually be well mixed and the pycnocline would be right at the surface. In an estuary, the whole pycnocline rises on flood and falls on ebb (figure 4.4, Cudaback and Jay [1996]). This reversible motion is not replicated by Monismith and Fong [1996].

In chapter 5, a two-layer model will be discussed, in which pycnocline thickness is

calculated from layer speeds. This model supports the importance of bottom friction to interfacial mixing [Monismith and Fong, 1996].

4.4 *Bottom Friction*

Pratt [1986] discusses the effect of bottom friction on the hydraulic control on flows through deep ocean passes. His analytic model includes a standard parameterization of bottom friction, and his results may be compared with two layer model results in chapter 5. Pratt's model has a moving layer underneath a thick inactive layer, and estuarine flows have two active layers, so the comparison is imperfect. However, there are useful similarities between the two types of flows. In any layered flow, bottom friction changes the location and sometimes the number of control points.

Pratt [1986] starts with the one-layer equations for momentum and mass conservation

$$u\frac{\partial u}{\partial x} + g'\frac{\partial h}{\partial x} = -g'\frac{\partial b}{\partial x} - \frac{C_d u^2}{h} \tag{4.8}$$

$$h\frac{\partial u}{\partial x} + u\frac{\partial h}{\partial x} = -\frac{uh}{w}\frac{\partial w}{\partial x} \tag{4.9}$$

where h is layer thickness, u is its speed, and g' is reduced gravity. Channel topography is represented by b, the height of the bottom above a flat reference layer and by channel width w. Bottom friction is assumed to be quadratic in u, and proportional to the roughness coefficient C_d. If these equations are combined to remove $\partial u/\partial x$, layer thickness may be expressed as

$$\frac{\partial h}{\partial x} = \frac{\frac{\partial b}{\partial x} + F^2(C_d - \frac{h}{w}\frac{\partial w}{\partial x})}{1 - F^2} \tag{4.10}$$

where $F^2 = u^2/g'h$ is the layer Froude number. For either a sill or pure constriction, the flow may be hydraulically controlled ($F^2 = 1$) at a single location. The interface slope $\partial h/\partial x$ must be finite even when $F^2 - 1 = 0$, so at the control point:

$$\frac{\partial b}{\partial x} - \frac{h}{w}\frac{\partial w}{\partial x} = -C_d \tag{4.11}$$

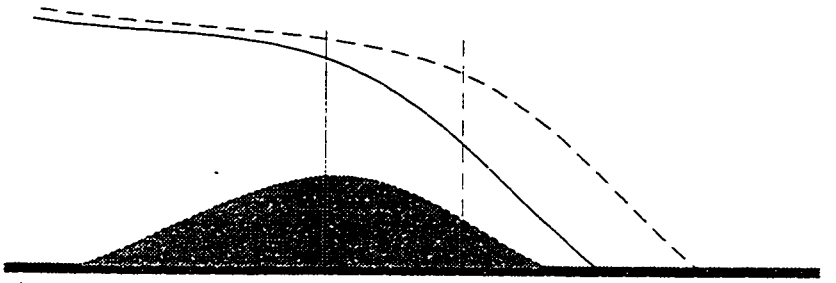

Figure 4.5: The effect of bottom friction on a one-layer flow (left to right) over a sill, after Pratt [1986]. In the absence of bottom friction, the flow is controlled directly over the sill crest The solid curve is the layer interface, the solid vertical line marks the control point. Bottom friction (dashed lines) moves the control point downstream to the point where $\partial b/\partial x = -C_d$, which Pratt calls the 'critical slope'.

As C_d is always positive, equation 4.11 indicates that the flow is controlled where the bottom slopes downward or the channel walls move farther apart – downstream of the control points for frictionless flow (figure 4.5). This displacement of the control point also has the effect of making the layer thicker, which is consistent with conservation of transport. Bormans and Garrett [1989] noted that, in the eastern part of the Strait of Gibraltar, the lower layer is quite deep, and only the upper layer is active. The upper layer acts like a one-layer flow, as described by Pratt [1986], and the friction between this current and the water beneath it moves the control point downstream (eastward). The parameterization of bottom friction in equation 4.8 may also be used in a two or three layer model.

Interfacial friction, which affects the momentum of the layers, has been less studied than interfacial entrainment, which causes mass exchange between the layers. Interfacial friction may be expressed in the momentum equation in a similar way to bottom friction; this formulation implies that the two water layers slide over each other like rigid blocks. The coefficient of friction between adjacent water layers is much less than that between water and the bottom, so the effect on momentum is slight. Nevertheless, interfacial friction can reduce the transport of salt water into and fresh water out of the estuary, and should be considered in layer models [Geyer

and Smith, 1987].

This section concludes the review of parameterizations which may be of use in a layer model. The following section discusses some alternate models and their resemblance to observations in the Columbia River entrance channel.

4.5 Columbia River Currents

Observed currents and density in the Columbia River entrance channel reveal the effects of vertical mixing and bottom friction. Many observations can be explained using existing models with high vertical resolution [Geyer, 1985; Valle-Levinson and Wilson, 1994; Chao and Paluskiewicz, 1991]. However, a simpler layer model, incorporating only the essential physics, may also work well.

Figure 4.6 shows a time series of along-channel current profiles from a station near the crest of a sill in the Columbia River entrance channel. Positive currents are landward. The series starts late on flood, with weak landward currents at all depths. As the ebb starts, water speed goes suddenly to zero at all depths, then surface currents increase to about 1.5 $m \cdot s^{-1}$at peak ebb shortly after 1100 hours. The oncoming flood opposes near bottom currents, until about 1500 hours, when baroclinic forces dominate the circulation. For a short time, the circulation is two-layered and consistent with two-layer hydraulic models [Armi and Farmer, 1986; Helfrich, 1995]. As the flood accelerates, bottom friction retards the near bottom currents, so the strongest currents are seen in the pycnocline [Geyer, 1985, 1988; Cudaback and Jay, 1996]. Strong flood currents push the surface fresh layer upriver and strong ebb currents push the salt layer out to sea, so the water column is nearly homogeneous near peak flood and peak ebb. The velocity profile is then determined by bottom friction alone, and currents increase smoothly toward the surface.

Three published models demonstrate certain aspects of the along channel circulation described above. Geyer [1985] replicated the mid-depth velocity maximum in

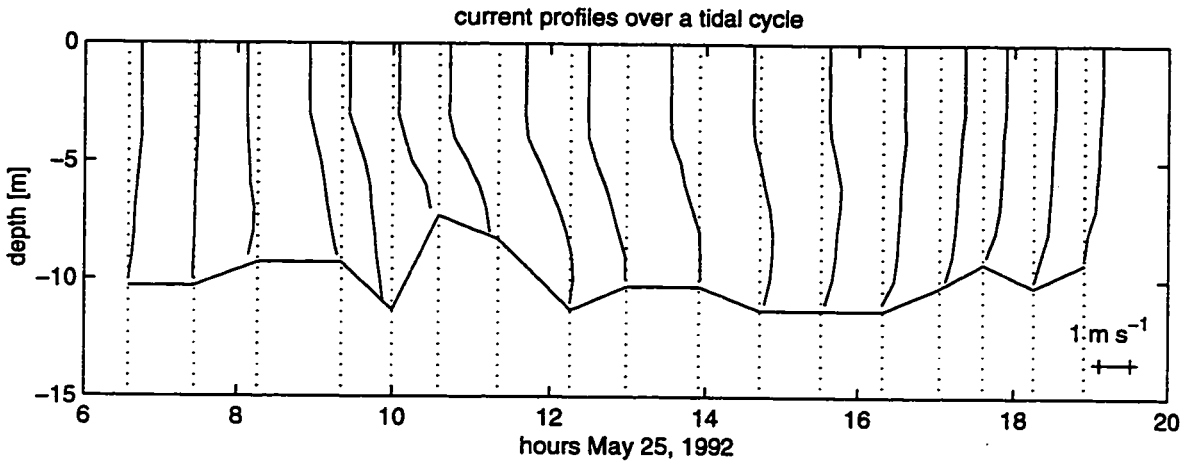

Figure 4.6: Observed current profiles over the tidal cycle. Ebb currents are always strongest at the surface. Early flood currents are strongest near the bottom, and peak flood currents are strongest at the surface. The difference between flood and ebb is an example of tidal asymmetry in internal circulation.

early flood currents using empirical data fits to a profile model. Valle-Levinson and Wilson [1994] and Chao and Paluskiewicz [1991] used two- and three-dimensional turbulence closure models to simulate circulation in all or part of the tidal cycle.

4.5.1 Early Flood: Mid-depth Maximum Current

Figure 4.7 shows circulation and salinity in two along-channel sections taken at early flood. Baroclinically driven flood currents should be strongest near the bottom, but observed currents are strongest at mid-depth, just landward of the sill. The observed three-layer circulation is due to a combination of effects – interfacial mixing develops a thick pycnocline, and bottom friction retards the lower layer, so the fastest currents are seen at mid-depth.

Geyer [1985] observed a similar pattern in the Fraser River, British Columbia. As does the Columbia River, the Fraser has two well-mixed layers separated by a thick pycnocline with a nearly linear salinity gradient. Geyer [1985] developed a vertical profile model of early flood currents currents using the Bernoulli energy to describe

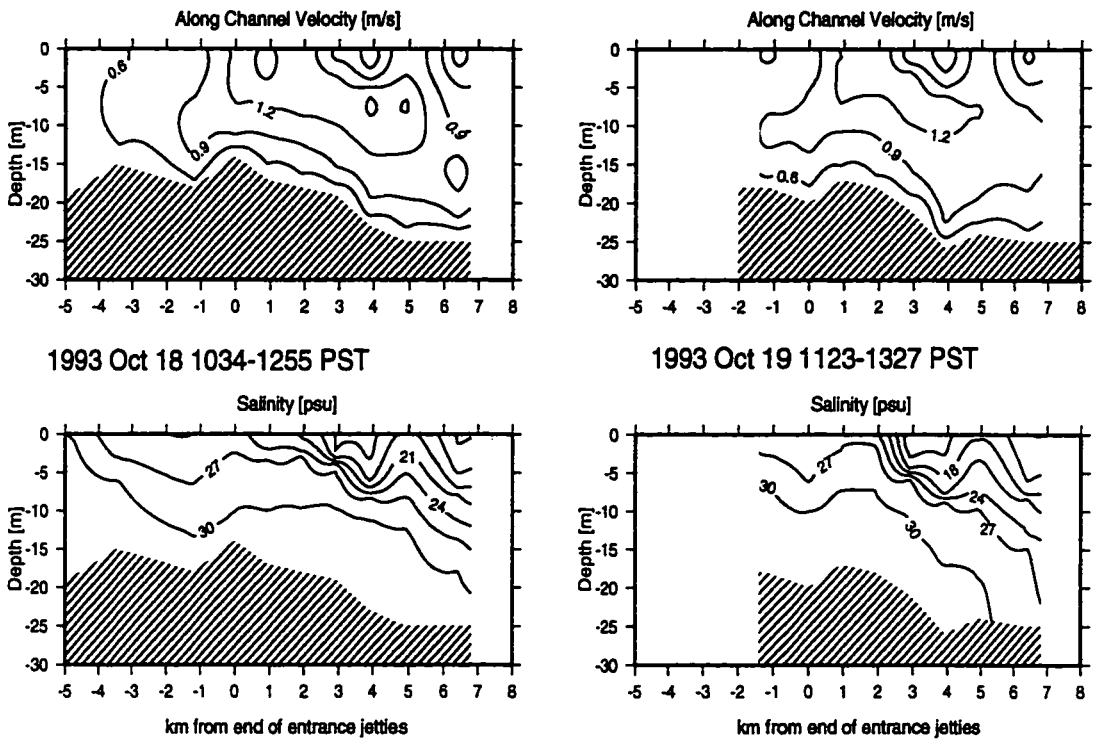

Figure 4.7: Along channel sections on early flood. Landward currents (to the right) are strongest at mid-depth, and slightly landward of both the sill and a lateral constriction at km 4. Salinity increases monotonically with depth.

inviscid currents above the velocity maximum and viscous boundary layer theory in the lower layer. The model requires delicate empirical adjustment of parameters representing mixing and bottom friction to re-create measured profiles.

An alternate approach to simulating this circulation pattern is a detailed multi-dimensional representation of mixing. As estuaries are salt-stratified, salinity is often modeled instead of density. The general equations for the conservation of momentum and salinity are:

$$\frac{\partial \mathbf{u}}{\partial t} + \mathbf{u} \cdot \nabla \mathbf{u} = -\frac{1}{\rho_0} \nabla p + \frac{\partial}{\partial z}[A_v \frac{\partial \mathbf{u}}{\partial z}] \tag{4.12}$$

$$\frac{\partial S}{\partial t} + \mathbf{u} \cdot \nabla S = \frac{\partial}{\partial z}[K_v \frac{\partial S}{\partial z}] \tag{4.13}$$

where $\mathbf{u}$ is the momentum vector and S is salinity. Vertical mixing is represented by the vertical eddy diffusivity A_v and the diffusivity of salt K_v (horizontal mixing is assumed to be negligible relative to vertical mixing). The values of A_v and K_v are estimated from local shear and stratification using a second moment turbulence closure scheme [Mellor and Yamada, 1982]. The vector equations may be applied in two dimensions (along-channel and vertical) [Valle-Levinson and Wilson, 1994] or three dimensions [Chao and Paluskiewicz, 1991].

Valle-Levinson and Wilson [1994] used a two-dimensional model to simulate the effects of vertical mixing on along channel circulation over an isolated sill in 20 meters of water. They simulated circulation through the entire tidal cycle, and their results in general are consistent with observations in the Columbia River. Their simulated flood circulation is especially interesting. Model runs with $A_v = 0$ and $K_v = 0$ resulted in strong bottom currents throughout the flood. When vertical mixing was added, the resultant flood currents were strongest at mid-depth. The mid depth maximum appears when barotropic currents are $\approx 0.3 - 0.5$ m $\cdot$ s^{-1}. This occurs near the end of flood with moderate barotropic tidal currents (0.4 m $\cdot$ s^{-1}), and on early flood with stronger tidal currents (0.8 m $\cdot$ s^{-1}). In the latter case, peak flood currents increased monotonically toward the surface. These results are consistent with observations in

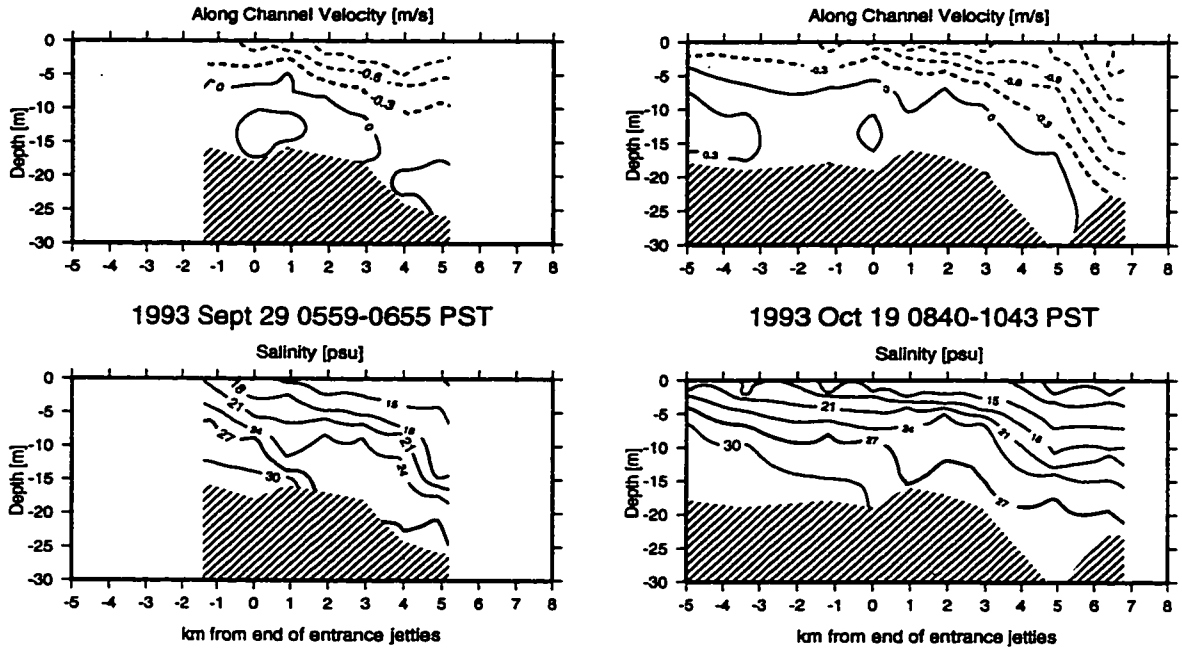

Figure 4.8: Along channel sections measured at the end of ebb. The 27 psu isohaline is significantly deeper than the -0.3m $\cdot$ s^{-1}velocity contour, indicating enhanced vertical mixing at the sill.

the Columbia River entrance channel, which is also 20 meters deep and subject to very strong barotropic currents (1-2 m $\cdot$ s^{-1}).

4.5.2 Late Ebb: Surface Density Currents

At the end of ebb, circulation in the Columbia River entrance channel is almost purely baroclinic – this is the only stage of the tide which is not dominated by barotropic currents. The waning ebb current may be pictured as a surface density current, which entrains water at the salt/fresh interface, but is unaffected by bottom friction. Figure 4.8 shows two along-channel sections taken at the end of ebb in fall of 1993. There is a moderate sill with its crest at km 1-2 and a sharp constriction due to a lateral jetty at km 4. In both sections, the ebb currents are confined to an upper layer, which is about 5 m thick near the seaward end, and 10-15 m thick at the landward end. The pycnocline in both sections is much thicker than the jet, and thickest just landward of

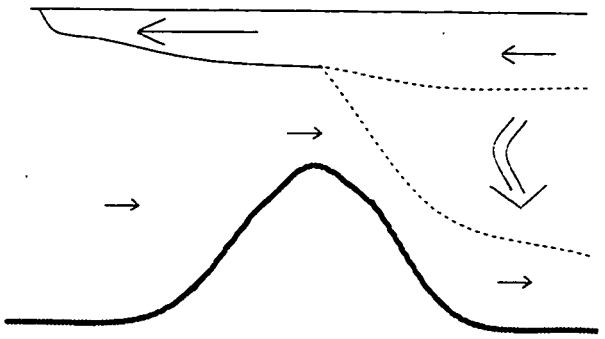

Figure 4.9: Schematic from Chao and Paluskiewicz [1991], showing downward entrainment of fresh water upstream of a sill. The mixing zone is denser and more slowly moving than the surface jet.

the sill; note especially the gap between the 24 and 27 psu isohalines. This observation is consistent with late ebb circulation modeled by Valle-Levinson and Wilson [1994] and also with a surface density current modeled by Chao and Paluskiewicz [1991], figure 4.9.

Chao and Paluskiewicz [1991] used a three-dimensional primitive equation model to study the hydraulics of a density current near an isolated sill. A surface density current was released at one end of the model channel and allowed to run to steady state with no barotropic current. If mixing was allowed, there was downward entrainment upstream of the sill and the salt-fresh interface lost definition. Figure 4.9 is a copy of their figure 2(d), flipped left to right so that fresh water is to the right. The thin upper layer represents the initial current of fresher water, and the wide curving arrow represents downward entrainment of fresh water, which creates a thick layer of intermediate density, upstream of the sill. Note that currents are fastest in the thin upper layer, and near zero in the mixing zone. The agreement with observations is quite good.

The multi-dimensional models of Valle-Levinson and Wilson [1994] and Chao and Paluskiewicz [1991] replicate many important aspects of circulation in the Columbia River entrance channel, but these models are computation intensive. A simpler layer model can isolate certain aspects of the physics and possibly replicate the essential

circulation features.

4.6 Discussion: Toward a Three-Layer Model

Many observations in the Columbia River entrance channel are consistent with a two-layer model of estuarine circulation, but two observations indicate the presence of a third layer. First, the pycnocline has a finite thickness, which varies over a tidal cycle. Pycnocline thickness may be estimated from either a two-layer or a three-layer model (chapters 5 and 6). Second, the the strongest early flood currents are observed in the pycnocline. This current profile is essentially a three-layer circulation, and it is impossible to replicate with a two-layer model.

This vertical displacement of the flood current can have a significant effect on along-channel transport of salinity. In the two-layer exchange model, most flood transport is in the saltier lower layer, but the observed transport is concentrated higher in the water column and carries less salt. Thus the estuary will be fresher than would be predicted from a two-layer model with the same exchange volume.

In chapters 5 and 6, I shall discuss two models of time-dependent layered flow through a narrow channel. In both models, layer thickness and speed vary along-channel and with time, in response to channel topography and an imposed barotropic tidal current. Each model represents slightly different effects of bottom and interfacial friction.

The two-layer model in chapter 5 clarifies the dynamics of layered flow and illustrates the numerical procedures [Helfrich, 1995]. In this model, interfacial friction is parameterized analogously to bottom friction; the two layers are seen as blocks of water sliding past each other. Bottom and interfacial stresses are parameterized as:

$$\frac{\tau_b}{\rho_2} = \frac{C_d|u_2|u_2}{h_2} \tag{4.14}$$

$$\frac{\tau_{12}}{\rho_2} = C_i|u_2 - u_1|(u_2 - u_1) = -\frac{\tau_{21}}{\rho_1} \tag{4.15}$$

where ρ_i, u_i and h_i are the densities, speeds and thicknesses of two layers, with layer 1 at the surface. C_d and C_i are the coefficients of bottom and interfacial friction, and τ is a shear stress. The interfacial stresses on the two layers are equal and opposite. From the two-layer model results, the pycnocline thickness is estimated using equation 4.7:

$$\delta z \approx \frac{Ri_{\text{crit}}(\delta u)^2}{g'} \tag{4.16}$$

where Ri_{crit} is a critical bulk Richardson number estimated from observations. This formulation, when applied to a time-dependent model, implies that the pycnocline thickness adjusts instantaneously relative to the tidal time scale.

The middle layer of the three-layer model (chapter 6) represents the pycnocline, and grows by entrainment from the other two layers. Implicit in this approach is the entrainment hypothesis [Turner, 1986], that the growth of a turbulent layer is essentially proportional to its speed (or to the shear between adjacent layers in the three layer model). This hypothesis allows me to consider entrainment as a bulk property of the flow, without resolving details of turbulent mixing. The lab work of Ellison and Turner [1959] provides one useful parameterization of mass entrainment, analogous to the growth of a bottom density current (equation 4.3). In equation 4.4, if the bottom slope, θ, is taken to be zero, and U is as the shear between two moving layers, the Richardson number Ri_o looks quite like our Ri_b. A few things must be remembered when applying (4.3) to exchange flow in a channel. First, estuarine exchange flows are driven by along-channel barotropic and baroclinic forcing, while the density currents studied by Ellison and Turner [1959] are driven by gravity down a sloping bottom. The different dynamics may cause a subtle difference in the turbulent entrainment between layers. Second, the density current grows at the expense of the ambient fluid, whereas the mixing layer grows at the expense of both the lower and the upper layers. Entrainment from above and below must be modeled separately,

thus:

$$\frac{\partial h_2}{\partial t} = e_{\text{above}} + e_{\text{below}} \tag{4.17}$$

where where h_2 is the thickness of the pycnocline, and

$$e_{\text{above}} = (u_2 - u_1) \cdot \frac{0.08(u_2 - u_1)^2 - 0.1(g'h_2/2)}{(u_2 - u_1)^2 + 5(g'h_2/2)} \tag{4.18}$$

$$e_{\text{below}} = (u_3 - u_2) \cdot \frac{0.08(u_3 - u_2)^2 - 0.1(g'h_2/2)}{(u_3 - u_2)^2 + 5(g'h_2/2)} \tag{4.19}$$

The three-layer model uses these entrainment velocities to represent the growth of the pycnocline and parameterizes bottom friction using equation 4.14.

The layer models described above should provide new insight on both pycnocline growth and vertical current structure. Success of the three-layer model will be measured by its ability to recreate the observed mid-depth maximum in the early flood current.

Chapter 5

THE TWO-LAYER COLUMBIA RIVER MODEL

Many aspects of estuarine circulation are consistent with a two-layer model. Geyer [1985] and Helfrich [1995] have published time dependent two layer models, and I have adapted Karl Helfrich's inviscid model for my use. The model starts from the equations of momentum and continuity for two layers with a rigid lid. By taking the vertical shear between the layers, the surface pressure is eliminated and the model may be driven with an imposed barotropic transport. Both bottom and interfacial friction may be included in the model, and pycnocline thickness may be estimated from model results. The three-layer model introduced in chapter 6 was based on this two-layer model.

5.1 Model Development.

A two-layer model requires conservation of momentum and mass in each layer, a total of four equations. A rigid lid approximation is then used to reduce the number and complexity of the equations. We start with the momentum equations for two layers which interact frictionally with each other and the bottom.

$$\frac{\partial u_1}{\partial t} + u_1 \frac{\partial u_1}{\partial x} = -g\frac{\partial}{\partial x}(h_1 + h_2 + h_s) - \frac{\partial}{\partial x}\frac{P}{\rho_1} - \frac{\tau_{12}}{\rho_1 h_1} \tag{5.1}$$

$$\frac{\partial u_2}{\partial t} + u_2 \frac{\partial u_2}{\partial x} = -g\frac{\partial}{\partial x}(\frac{\rho_1}{\rho_2}h_1 + h_2 + h_s) - \frac{\partial}{\partial x}\frac{P}{\rho_2} - \frac{\tau_{21} + \tau_b}{\rho_2 h_2} \tag{5.2}$$

where the subscripts are layer indices, layer 1 being at the surface (figure 5.1). Layer speeds are u_i, layer thicknesses are h_i, and h_s is the elevation of the bottom above a flat reference datum. Densities ρ_i are constant in both space and time, and u_i and h_i

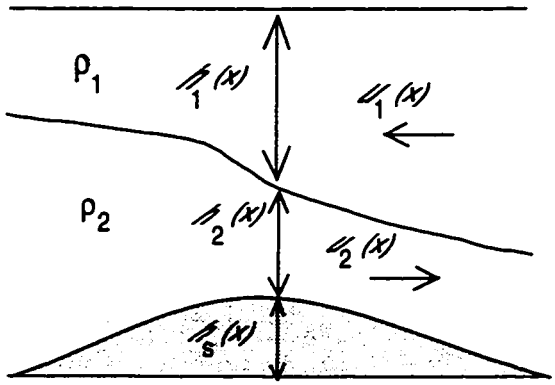

Figure 5.1: Definition sketch for two-layer model.

vary along channel and with time.

Bottom friction is parameterized in a standard way as,

$$\frac{\tau_b}{\rho_2} = C_b|u_2|u_2 \tag{5.3}$$

where C_b is a bottom roughness coefficient. Interfacial friction is parameterized analogously to bottom friction:

$$\frac{\tau_{12}}{\rho_2} = C_i|u_2 - u_1|(u_2 - u_1) = -\frac{\tau_{21}}{\rho_1} \tag{5.4}$$

where C_i is a coefficient of friction between the two water layers, and the interfacial stresses on the two layers are equal and opposite. This model implies that the two layers act as solid blocks sliding against each other. The values of C_b and C_i will be discussed below.

As in all hydraulic control theory, we make the hydrostatic, Boussinesq and rigid lid approximations. For the flow to be hydrostatic, along-channel variations in depth and width must be gradual. The Boussinesq approximation allows us to ignore vertical density gradients except in the baroclinic pressure. The rigid lid approximation indicates that surface displacements are insignificant relative to displacements of the layer interface; a physical rigid lid must exert a finite pressure P to hold surface flat. In this case, both total flow depth H and along channel transport q_b must be

conserved.

$$H = h_1 + h_2 + h_s \tag{5.5}$$

$$q_b = a_1 \cdot u_1 + a_2 \cdot u_2 \tag{5.6}$$

$$\frac{\partial H}{\partial x} = \frac{\partial H}{\partial t} = \frac{\partial q_b}{\partial x} = 0 \tag{5.7}$$

where each layer has area $a_i = w \cdot h_i$. In channels whose depth and width varies significantly [Jay, 1991], transport may vary along channel, but spatially invariant transport must be assumed in this model formulation. Note that the bottom elevation is included in the total flow depth, but not in the transport equation. The rigid-lid conditions allow us to reduce the number of unknowns; instead of three equations each for momentum and continuity, we can solve two equations each.

Now take the vertical shear between the two layers to eliminate the surface pressure gradient [Helfrich, 1995], and define the vertical shear $s = u_2 - u_1$, giving

$$\frac{\partial s}{\partial t} = -\frac{\partial}{\partial x}\left(\frac{u_2^2}{2} - \frac{u_1^2}{2}\right) + \frac{g(\rho_2 - \rho_1)}{\rho_2}\frac{\partial h_1}{\partial x} - C_i|s|s\left(\frac{1}{h_2} + \frac{1}{h_1}\right) - \frac{C_b|u_2|u_2}{h_2} \tag{5.8}$$

In equation 5.8, the surface pressure gradient is multiplied by $(1/\rho_2 - 1/\rho_1)$, which is negligibly small under the Boussinesq approximation.

The layer velocities u_i can be expressed in terms of shear $s = u_2 - u_1$ using equation 5.6, thus:

$$u_1 = \frac{q_b + a_1 s - As}{A} \tag{5.9}$$

$$u_2 = \frac{q_b + a_1 s}{A} \tag{5.10}$$

Total transport $q_b(t)$, which may be a combination of tidally varying and steady transport, is now used to drive the model.

The continuity equation for each layer is

$$\frac{\partial}{\partial t}(wh_i) + \frac{\partial}{\partial x}(wh_i u_i) = 0 \tag{5.11}$$

where i is the layer index. Channel width w, layer thickness h_i and speed u_i all vary with distance x along the channel.

Equations 5.8 and 5.11 can be nondimensionalized using an internal wave speed $\sqrt{g'H}$ for u_i, total water depth H for h_i and topographic scale L for x. The time scale T for tidal variations is about half a tidal cycle, and this provides a new length scale: the distance traveled by an internal wave over a half tidal cycle $T\sqrt{g'H}$. If this distance is much longer than the topographic scale L, internal adjustments are very rapid and tidal motion may be ignored in the hydraulic control problem. Helfrich [1995] expresses this concept using his factor γ,

$$\gamma = \frac{T\sqrt{g'H}}{L} \tag{5.12}$$

where $g' = g(\rho_2 - \rho_1)/\rho_2$ is reduced gravity. If $\gamma > 30$, the problem may be treated as steady state [Armi and Farmer, 1986]. In typical estuarine channels, $\gamma \approx 1 - 10$, and in the Columbia entrance channel, $\gamma \approx 4 - 6$, so both hydraulic and time-dependent effects are significant.

The result of this non-dimensionalization is:

$$\frac{1}{\gamma}\frac{\partial s}{\partial t} = -\frac{\partial}{\partial x}\left(\frac{u_2^2}{2} - \frac{u_1^2}{2}\right) + \frac{\partial h_1}{\partial x} - \frac{LC_i|s|s}{H}\left(\frac{1}{h_2} + \frac{1}{h_1}\right) - \frac{LC_b|u_2|u_2}{H \cdot h_2} \tag{5.13}$$

$$\frac{1}{\gamma}\frac{\partial h_1}{\partial t} = -\frac{1}{w}\frac{\partial}{\partial x}(wh_1u_1) \tag{5.14}$$

where layer speeds u_i are now defined in terms of q_b and s, equations 5.9 and 5.10. Only one continuity equation is needed, because the other layer thickness is trivial. Karl Helfrich generously provided me with a copy of his model code in FORTRAN; I translated the code into MATLAB and added terms for bottom and interfacial friction.

Boundary conditions in this model do not represent the salt and fresh basins. Rather, the initial condition is a layer interface which is close to the surface at the seaward end and near the bottom at the landward end, so that the along-channel density gradient is implicit. The radiation boundary condition, discussed in chapter

6, ensures that information leaves the model domain and does not re-enter it, with the result that the ends of the interface do not move much. An interface which initially drops straight from the upper seaward corner to the lower landward corner of the model domain develops a smooth curve due to channel topography.

5.2 Channel Topography

Several topographic features in the Columbia River entrance channel may act as hydraulic controls (figure 1.3). The seaward end of the channel is constricted by the entrance jetties, which establish the overall inflow width of about 3 km. Mean flow depth is about 20 meters. Landward of these jetties, there is a moderate sill with its crest at Buoy 10. The seaward slope of the sill is quite gradual, but the landward slope drops about 10 meters in the 1.5 kilometers between Buoy 10 and Jetty A. Lateral Jetty A was built to constrict the flow, so that fast currents would scour the bottom and reduce the need for dredging; the deepest point in the channel is just off the end of this jetty, where the channel is about 2 km wide. For modeling purposes, the channel topography may be represented as a moderate sill just seaward of a lateral constriction.

Figure 5.2 shows results of two-layer model runs to steady state, for purely baroclinic forcing and no interfacial or bottom friction. The Columbia River entrance channel is represented in the left column; lighter water is to the left, consistent with a northward view of the channel. The salinity interface drops sharply through the narrows, indicating hydraulic control there, but the interface is apparently unaffected by the sill. This result was predicted by Farmer and Armi [1986], who noted that a the sill crest on the dense side of a constriction could be flooded, so that the exchange flow would be controlled only at the narrows. Field observations also show control at Jetty A.

Farmer and Armi [1986] have made a careful study of hydraulic control in the

presence of a sill/constriction combination. Their work has been devoted to the Straits of Gibraltar, a classic example of hydraulic control in nature. This channel has a shallow sill on the Atlantic (less dense) side of a moderate constriction. In figure 5.2, the right column represents the Straits of Gibraltar, with denser water to the right. The distortions of the interface indicate that this flow is controlled at both sill and narrows, but the sill has a greater effect on the interface. Farmer and Armi [1986], figure 13, show a hydraulic jump west of the sill, which is not replicated in my model due to different boundary conditions. The constriction in my model run is somewhat narrower than that used by Farmer and Armi [1986], and has a more significant effect on the interface. These model results indicate that hydraulic control in the Columbia River may be adequately modeled using just a lateral constriction.

5.3 Scaling

Several model parameters must be set to represent properties of the Columbia entrance channel; and some of the parameters are interdependent. Two fixed parameters are bottom depth H, which is 15-25 meters, and the M_2 tidal period, 12.42 hours. Reduced gravity $g' \approx 0.01$, so the internal wave speed $\sqrt{g'H}$ is 1-1.5 $\mathrm{m \cdot s^{-1}}$and $T\sqrt{g'H} \approx 20$ kilometers. Two model input parameters, γ and the aspect ratio L/H, are related thus:

$$\gamma \frac{L}{H} = \frac{T\sqrt{g'H}}{L} \frac{L}{H} \approx 1000 \tag{5.15}$$

The behavior of the model now hinges upon our choice of L. If L is small, γ must be large, so the model interface will move the length of the model channel each period – this can lead to some instability. However, if L is large, the strength of both bottom and interfacial friction increases by a factor of L/H.

In the real channel, there are a few possible choices for L. Jetty A, the most significant topographic constriction, is less than 200 m wide, but the effect of the jetty extends farther. The 10 m depth contour on a nautical chart suggests a scale

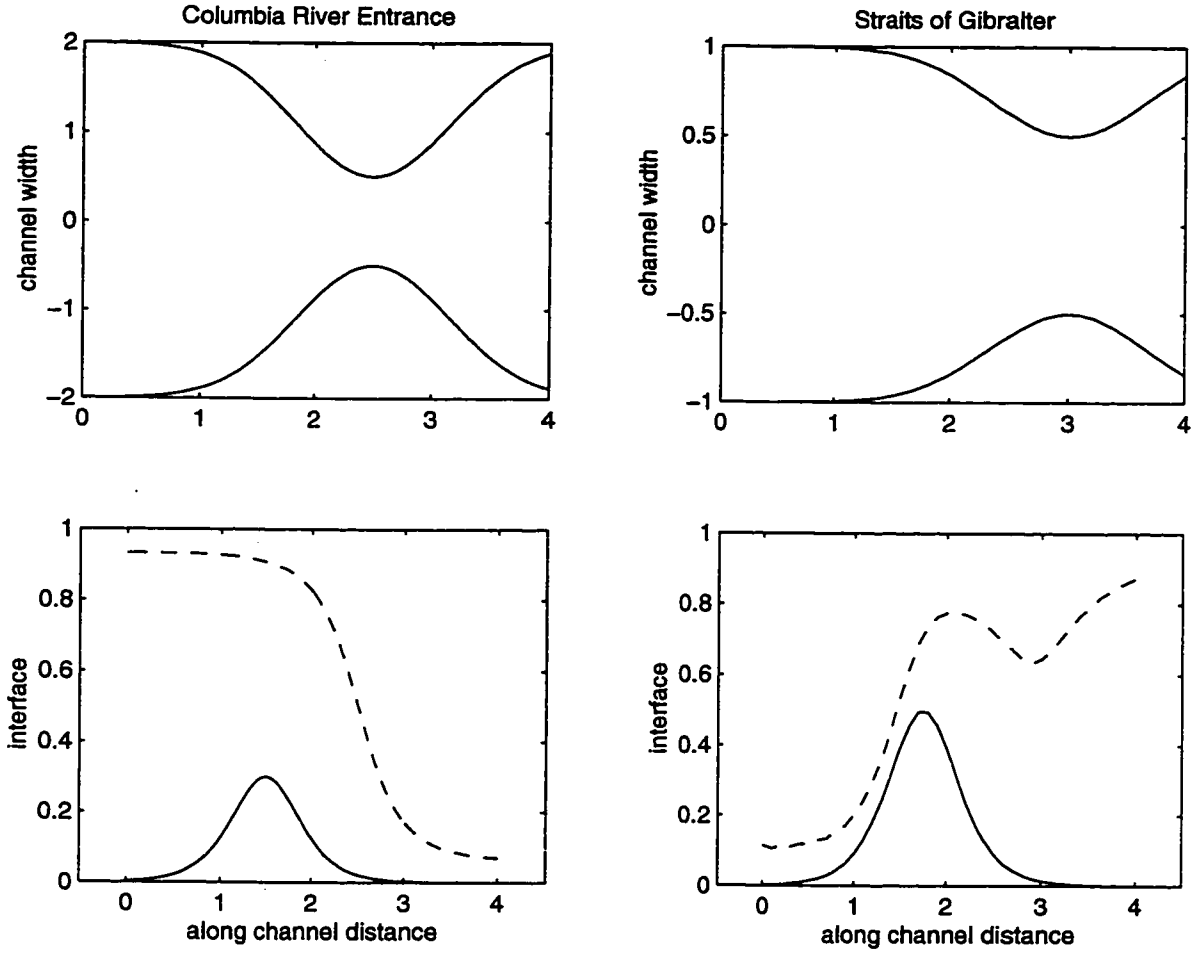

Figure 5.2: Interface positions for unforced exchange through combinations of sill and narrows. Top row shows plan views of the channel constriction for the Columbia River entrance channel and the Straits of Gibraltar. Bottom row shows section views; solid lines are sills, dashed lines are the layer interfaces. Column 1 Columbia River Entrance: dense water is to the left, and the the sill is on the dense side of the narrows; the flow is controlled only at the narrows. Column 2, Straits of Gibraltar: dense water is to the right, and the sill is on the light side of the narrows; the flow is controlled both at sill and narrows.

of 1-2 km. As the hydrostatic approximation requires that $L/H >> 1$, the minimum aspect ratio appropriate to this model is $L/H = 100$; this choice requires that $\gamma = 10$. Another option for topographic scaling is the length of the entrance channel from the ends of the entrance jetties to Jetty A, $L \approx 5$ km. This gives $L/H = 250$ and $\gamma = 4$.

Depth averaged tidal current speeds in the real channel are 1-2.5 $m \cdot s^{-1}$, and fluvial currents are 0.1-0.5 $m \cdot s^{-1}$. Barotropic current speeds are thus represented nondimensionally as

$$q_b(t) = q_{b0} \sin 2\pi t + q_m \tag{5.16}$$

where tidal current $q_{b0} \approx 1 - 2$ and mean current $q_m \approx 0.1 - 0.5$.

The coefficients of bottom and interfacial friction have been estimated from prior studies. Geyer [1985] estimated C_b from the bed properties of the Fraser River, British Columbia, which is quite similar to the Columbia River. He found that $C_b \approx 3 \cdot 10^{-3}$, which is consistent with prior estimates. Giese and Jay [1989] found $C_b \approx 8 \cdot 10^{-3}$ appropriate for the Columbia River entrance. Geyer then parameterized interfacial friction as momentum entrainment, and chose an entrainment coefficient to match the time evolution of salinity in the salt wedge. His value of $C_i \approx 2 \cdot 10^{-5}$ seems appropriate for my model, as the friction between adjacent water parcels must be much less than the friction between water and bottom. Geyer found that interfacial friction had little influence on continuity and almost no influence on momentum. The primary role of interfacial exchange is to create an interfacial layer of intermediate density. The effects of various values of C_b and C_i will be tested in the following sections.

5.4 Bottom Friction

The following model results were calculated using $q_{b0} = 1.5$ and $q_m = -0.3$, representing the approximate conditions under which my data (chapter 4) were collected. The aspect ratio $L/H = 250$ and time scale factor $\gamma = 4$; the model narrows constrict the flow by a factor of 3, and represent the whole entrance channel of the Columbia

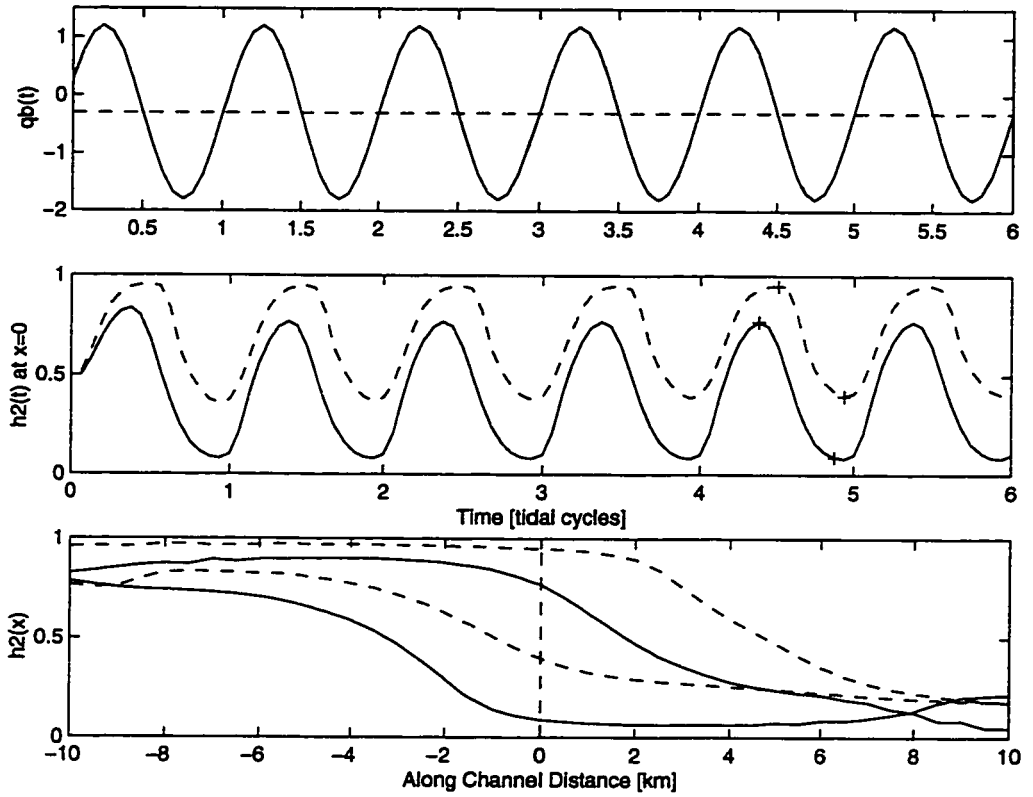

Figure 5.3: Two Layer Model Results. Imposed tidally-varying barotropic transport (a) causes vertical oscillation of the interface at the narrows (b). Vertical oscillation is much reduced in the presence of bottom friction (dashed line) relative to the frictionless case (solid line). Interface position as a function of along-channel distance is shown in (c). The two solid lines show the maximum landward and seaward excursions of the interface in the frictionless model, and the dashed lines show the excursions in the presence of bottom friction. Note that bottom friction both raises the interface and reduces its range of motion.

River.

Figure 5.3 compares model results with and without bottom friction. The top two plots are along channel transport and interface height at the narrows, both as a function of time. In (a), the imposed transport is sinusoidal, positive landward, and there is a small constant outflow (mean flow < 0). In (b), the interface responds with vertical oscillations at the narrows, lagging the transport by less than 90°. In the absence of bottom friction (solid line) the interface oscillates through most of the water column; it drops somewhat more sharply than it rises, due to the reinforcement of ebb

currents by the mean river current. In the presence of bottom friction, $C_b = 3 \cdot 10^{-3}$, (dashed line), the range of motion of the interface is greatly reduced, and the interface is consistently higher in the water column.

The maximum interface height at the narrows, shortly after the peak of each flood, corresponds to the extreme landward excursion of the salt wedge; the minimum height shows the extreme seaward excursion. Two representative times for each case were chosen from subplot (b) and marked with small crosses around 4.4 tidal periods and 4.9 periods. Note that the maximum landward excursion in the frictional case occurs slightly later than in the frictionless case. In subplot (c) the interface positions at these times are plotted as a function of space. In the absence of bottom friction (solid lines), the interface moves about as far landward of the narrows as it does seaward. With bottom friction (dashed lines) the interface is significantly offset, landward and upward, and its range of motion is halved. At all stages of the tide, bottom friction moves the interface landward relative to its frictionless position.

These results are consistent with the results of Pratt [1986] in figure 4.5. As currents in the lower layer are strictly landward, the effect of bottom friction on the lower layer is similar to the effect on a single layer underneath an inactive layer [Pratt, 1986] – in both cases the control is moved landward of the topographic control, and the lower layer is thickened.

5.5 Total Internal Froude Number

The total internal Froude number,

$$\mathrm{G}^2 = \frac{u_1^2}{g' h_1} + \frac{u_2^2}{g' h_2} \tag{5.17}$$

may easily be calculated from model results, and compared with observations made near Buoy 10 in the Columbia River entrance channel (figure 1.3). The time-series of G in figure 5.4 were phase shifted so that model transport aligned with observed

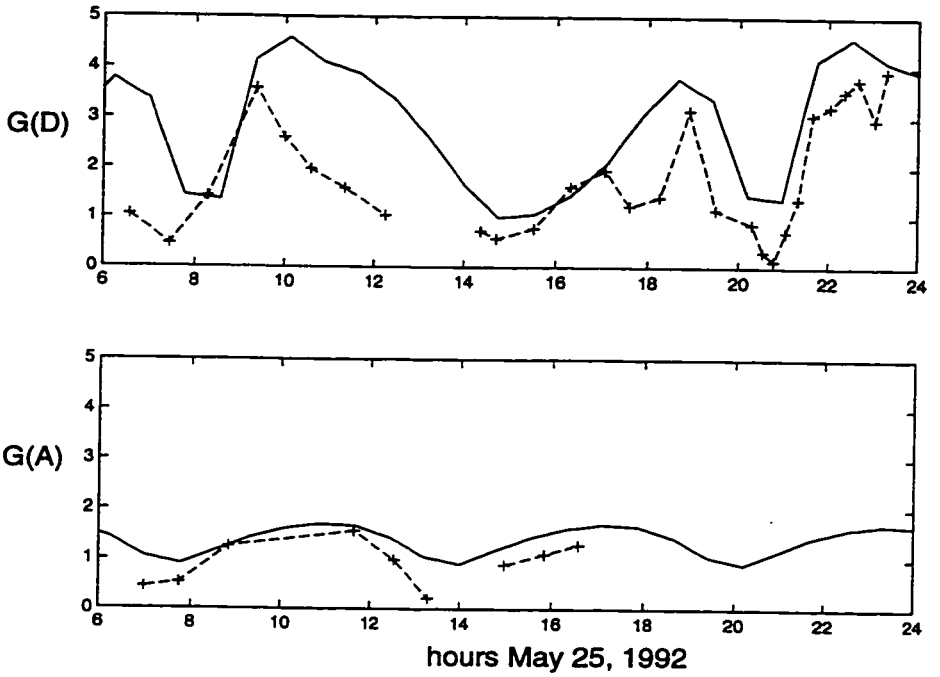

Figure 5.4: Comparison of observed and modeled Froude numbers. Top: Station D compared with model using $q_{b0} = 1.5, q_m = -0.3, C_b = 3 \cdot 10^{-3}$. Bottom: Station A compared with model using $q_{b0} = 1, q_m = 0, C_b = 0$.

transport. The internal Froude number is very sensitive to minor changes in model parameterizations, and to lateral variations in observed circulation.

Model results with tidal and fluvial transport and bottom friction ($q_{b0} = 1.5, q_m = -0.3, C_b = 3 \cdot 10^{-3}$) compare well with observations from station D, at the south side of the channel (figure 5.4, top). This result contrasts with frictionless model results shown in figure 3.6. The addition of bottom friction phase shifts the largest peaks in the G time series and dramatically improves agreement with these observations. At stations A, on the north side of the channel, shallower water reduces the strength of along-channel circulation, and this is reflected in the observed G time series (figure 5.4, bottom). These observations are best matched with model results using purely tidal forcing and no bottom friction ($q_{b0} = 1, q_m = 0, C_b = 0$). This condition is, of course, non-physical. The excellence of the fit indicates an important limitation in

interpreting model results. The data from station A alone could be taken to support the frictionless model, but the data from station D indicate the importance of bottom friction. Any model must be interpreted with great care, and coincidental data fits should not be over-interpreted. The differences between stations A and D also indicate that the real world is not purely one-dimensional. It may be that different stream lines have different hydraulic control properties.

5.6 Interfacial Friction and Mixing

The two-layer model was run with various values of interfacial friction. For $C_i = 4 \cdot 10^{-5}$, there was no discernible effect either on current speed or on interface position [Geyer, 1985]. Interfacial friction becomes significant only when $C_i > 10^{-3}$, which is absurd; real friction between water masses must be significantly less than bottom friction. For any realistic value of interfacial friction, the model shows no effect. Therefore, in the three-layer model (chapter 6), interfacial friction will not be used.

Interfacial friction has little effect on the momentum balance, but vertical entrainment across the layer interface is significant. If entrainment is assumed to be much quicker than the tidal time cycle, the pycnocline thickness can be estimated from two-layer model results using the bulk Richardson number, as described in chapter 4.

$$\delta z \approx \frac{Ri_b(\delta u)^2}{g'} \tag{5.18}$$

where δz is the pycnocline thickness, $\delta u = u_2 - u_1$ is the shear between the layers. The reduced gravity $g' = g(\rho_2 - \rho_1)/\rho_2$ is set to one in the model non-dimensionalization.

When the pycnocline thickness is estimated from two-layer model results, total along-channel transport must be conserved. As the top and bottom layer become thinner due to the growth of the pycnocline, they must speed up to conserve transport. The vertical shear between the upper and lower layers increases thus:

$$u_2' - u_1' = \frac{8h_2h_1(u_2 - u_1)}{8h_2h_1 - \delta z(h_2 + h_1)} > u_2 - u_1 \tag{5.19}$$

where primes indicate layer speeds adjusted for the pycnocline thickness [Jay and Smith, 1990b]. Transport conservation combined with equation 5.18 gives a third-order polynomial which may be solved for δz.

For the model results in figure 5.5(a and b), the pycnocline thickness was calculated using $Ri_b = 0.3$ at all stages of the tide. Observations in the Columbia and Fraser rivers suggest that Ri_b actually varies tidally, and may be much larger at peak flood. Use of a constant, low value of Ri_b may underestimate the flood pycnocline thickness. However, this formulation (equation 5.18) assumes that the pycnocline has reached its maximum thickness for a given flow condition. On ebb, the salt and fresh water may mix while moving through the estuary, so the pycnocline is at its maximum thickness. On flood, the salt water approaches the from the deeper ocean, and the pycnocline may not be fully developed. These considerations indicate that the model may overestimate the pycnocline thickness on flood.

Two-layer model results both with and without bottom friction are compared with observed salinity from the Columbia River entrance channel. Observations were made near the south side of the main navigational channel, at Buoy 10 in the entrance channel (figure 1.3), where the mean water depth was 12 meters. Model results have been scaled by the water depth and phase shifted so that model barotropic transport coincides with real flood and ebb transport.

In figure 5.5a, the interface from the frictionless model lies below the observed pycnocline, and the model pycnocline is too thick on flood and too thin on ebb. By contrast, the model pycnocline with bottom friction (figure 5.5b) fits observations quite well. The reduced speed of the lower layer raises the pycnocline to the observed level. On flood, bottom friction reduces vertical shear, and the model pycnocline is about 2 m thick. This is slightly thicker than observed, but within a plausible error. On ebb, bottom friction increases the vertical shear, causing significant vertical mixing. During this period, the pycnocline is much thicker and more diffuse (about 8 m), consistent with observations. At least on ebb, bottom friction causes an increase

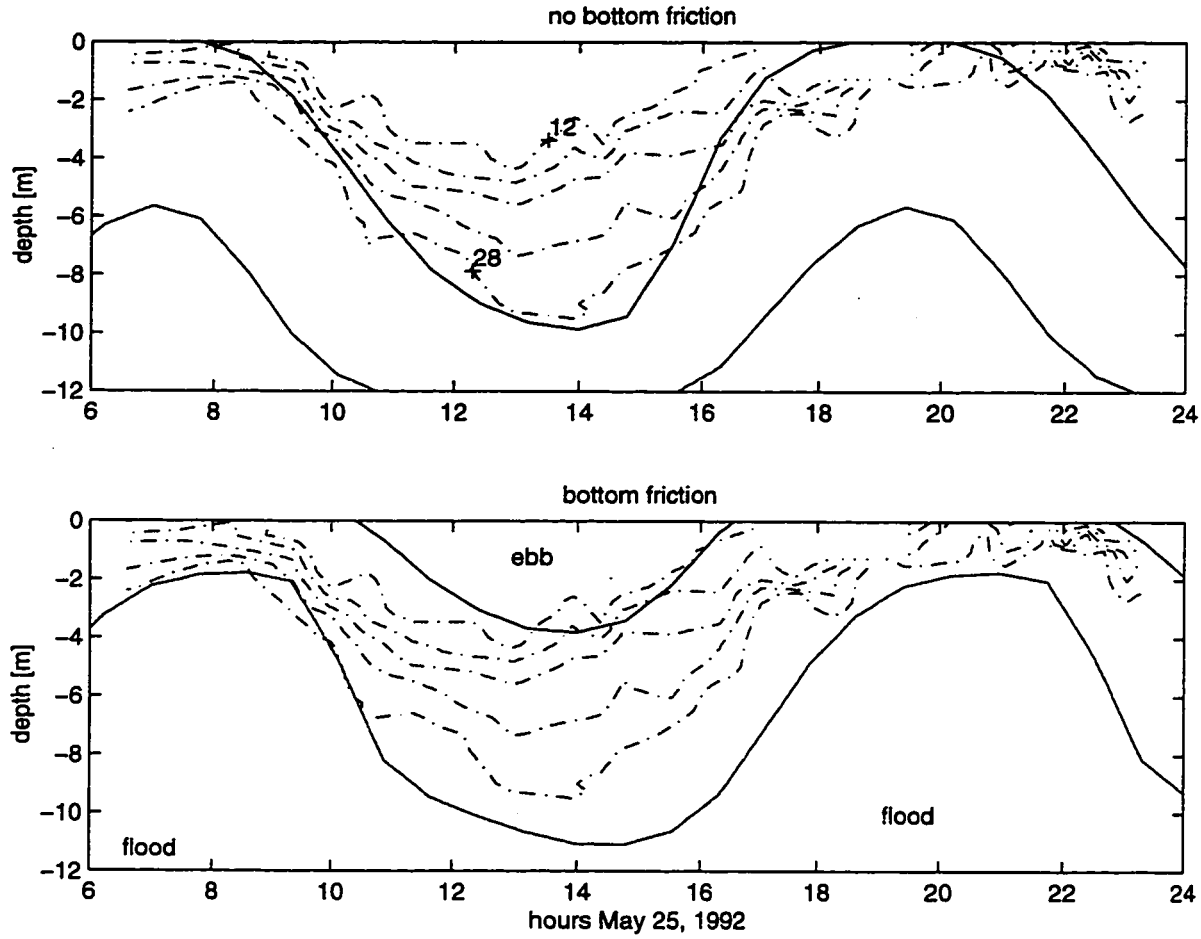

Figure 5.5: Salinity contours (-. lines) from an 18 hour time series in the Columbia River entrance channel are compared with numerical model results. In the absence of bottom friction, the pycnocline (solid lines in subplot a) too low in the water column; it is too thin on ebb and too thick on flood. Model results with bottom friction (b) represent the pycnocline much better.

in pycnocline thickness, consistent with the model of Monismith and Fong [1996].

5.7 Conclusions

The behavior of this two-layer model provides useful information for the three-layer model in chapter 6. First, the hydraulic properties of the flow may be predicted using a simple channel constriction – the small sill seaward of Jetty A is less significant [Farmer and Armi, 1986]. Either the small scale constriction of Jetty A or the large scale constriction of the entrance channel may be considered. Second, two model input parameters must be related to each other. The distance traveled by an internal wave over half a tidal cycle is $T\sqrt{g'H}$, the topographic length scale is L and γ is the ratio of the two. The aspect ratio of the model channel is L/H. Both the tidal period and the water depth are fixed, so $\gamma L/H \approx 1000$ is fixed. Third, a bottom friction coeffient of $C_b = 3 \cdot 10^{-3}$ provides excellent agreement with observations. Bottom friction pushes the layer interface upward in the water column, and reduces its tidal motion [Pratt, 1986]. Bottom friction also increases vertical shear on ebb and decreases shear on flood, so the pycnocline grows thicker and thinner over the tidal cycle [Monismith and Fong, 1996]. Fourth, interfacial friction has no discernible effect on the momentum balance or interface position, and will not be used in the three-layer model.

Chapter 6

THREE-LAYER MODEL DEVELOPMENT

Many aspects of estuarine circulation may be represented by a two-layer exchange model in which a seaward-moving fresh layer overlies a landward-moving salt layer. However, my observations in the Columbia River entrance channel show that bottom friction and interfacial mixing significantly affect the circulation. The two layers are separated by a pycnocline (salinity interface) which grows quickly on ebb and thins on flood, but always has a finite thickness. On early flood, the strongest currents are seen in the pycnocline as a mid-depth jet. This current distribution reduces salinity transport into the estuary.

To help explain these observations, I developed a numerical model of along-channel circulation in an estuarine channel. The model combines internal hydraulic control theory with parameterizations of bottom friction and interfacial mixing. The model has one spatial dimension (along channel), with three layers. The middle layer represents the pycnocline and grows by turbulent entrainment from the other two layers. The model is time-dependent and can simulate either tidal variations or the approach to a steady state. The details of the vertical velocity profile are not resolved, but the layer model runs quickly and may be used to replicate many different combinations of topography and forcing.

The model domain represents a physical channel between basins of salt and fresh water, and the along-channel salinity gradient is implicit in the initial slope of the layer interfaces. The initial layer interfaces are near the surface at the seaward end and near bottom at the landward end of the channel. Radiation boundary conditions allow information to propagate out of, but not into the model domain. Due to

these conditions, the layer interfaces near the boundaries are almost flat and do not change position significantly. All adjustments of the interfaces occur near the channel constriction in the center of the model domain.

Each layer conserves momentum according to the Navier-Stokes equation, and the bottom layer is retarded frictionally. The layer equations are subtracted from one another to represent the conservation of vertical shear. When the rigid-lid approximation is made, along-channel transport is incorporated into the dynamic equations. This barotropic transport represents tidal and riverine currents.

The effect of vertical mixing is represented in the continuity equation. It is assumed that the top and bottom layers mix to form water of intermediate density, which represents the pycnocline. This middle layer thus grows at the expense of entrainment from the other two layers, but may also shrink due to lateral advection. The layer interfaces represent isopycnals, so there is no density entrainment into the pycnocline. Momentum entrainment between adjacent layers has the same effect as interfacial friction: reducing the vertical shear. Interfacial friction was found in chapter 5 to have an insignificant effect on the momentum balance [Geyer, 1985], so is not included in the three layer model.

6.1 Momentum Equations

A three-layer model requires conservation of momentum and mass in each layer, a total of six equations. A rigid lid approximation is then used to reduce the number and complexity of the equations.

We start with the momentum equations for three layers:

$$\frac{\partial u_1}{\partial t} + u_1 \frac{\partial u_1}{\partial x} = -g\frac{\partial}{\partial x}(h_1 + h_2 + h_3 + h_s) - \frac{\partial}{\partial x}\frac{P}{\rho_1} \tag{6.1}$$

$$\frac{\partial u_2}{\partial t} + u_2 \frac{\partial u_2}{\partial x} = -g\frac{\partial}{\partial x}(\frac{\rho_1}{\rho_2}h_1 + h_2 + h_3 + h_s) - \frac{\partial}{\partial x}\frac{P}{\rho_2} \tag{6.2}$$

$$\frac{\partial u_3}{\partial t} + u_3 \frac{\partial u_3}{\partial x} = -g\frac{\partial}{\partial x}(\frac{\rho_1}{\rho_3}h_1 + \frac{\rho_2}{\rho_3}h_2 + h_3 + h_s) - \frac{\partial}{\partial x}\frac{P}{\rho_3} - \frac{\tau_b}{\rho_3 h_3} \tag{6.3}$$

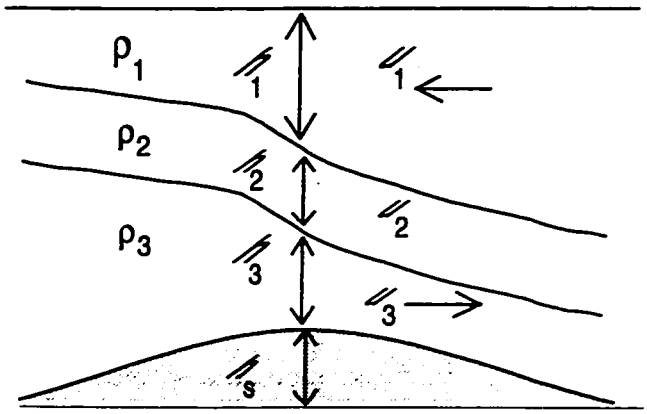

Figure 6.1: Definition sketch for three-layer model.

where the subscripts are layer indices, layer 1 being at the surface (figure 6.1. Layer densities ρ_i are constant in space and time. Layer thicknesses h_i and currents u_i vary both along-channel and with time. Surface pressure is P and h_s is the elevation of the bottom above a flat reference datum. Note that in channel flow with an uneven bottom, both the hydrostatic pressure and the potential energy due to lifting a water parcel over an obstacle are included in the force equations (L. Armi, personal communication). Bottom friction is parameterized in a standard way as,

$$\frac{\tau_b}{\rho_3} = C_b|u_3|u_3 \tag{6.4}$$

where C_b is a bottom roughness coefficient C_b. Based on the results of Geyer [1985] and the model in the previous chapter, interfacial friction is not included in this model.

We make the rigid-lid approximation, that surface displacements are insignificant relative to displacements of the layer interface. A physical rigid lid must exert a finite pressure P to hold surface flat. In this case, both total flow depth H and along channel transport q_b must be conserved.

$$H = h_1 + h_2 + h_3 + h_s \tag{6.5}$$

$$q_b = a_1 \cdot u_1 + a_2 \cdot u_2 + a_3 \cdot u_3 \tag{6.6}$$

$$\frac{\partial H}{\partial x} = \frac{\partial H}{\partial t} = \frac{\partial q_b}{\partial x} = 0 \tag{6.7}$$

where each layer has area $a_i = w \cdot h_i$, and the bottom elevation is included in the total flow depth, but not in the transport equation. The rigid-lid conditions allow us to reduce the number of unknowns; instead of three equations each for momentum and continuity, we can solve two equations each.

Helfrich (1995) drove his rigid-lid two-layer model with a barotropic tidal transport. He took the vertical shear between the two layers, to eliminate the surface pressure gradient; a similar technique can be applied for three layers. First, subtract the layer equations from each other, and define vertical shears $U_{21} = u_2 - u_1$ and $U_{32} = u_3 - u_2$. The Boussinesq approximation allows neglect of terms like $\frac{\partial}{\partial x}(\frac{P}{\rho_i} - \frac{P}{\rho_{i-1}})$, giving:

$$\frac{\partial}{\partial t}U_{21} = -\frac{\partial}{\partial x}(\frac{u_2^2}{2} - \frac{u_1^2}{2}) - g\frac{\partial}{\partial x}(h_1\frac{\rho_1}{\rho_2} - h_1) \tag{6.8}$$

$$\frac{\partial}{\partial t}U_{32} = -\frac{\partial}{\partial x}(\frac{u_3^2}{2} - \frac{u_2^2}{2}) - g\frac{\partial}{\partial x}(h_1(\frac{\rho_1}{\rho_3} - \frac{\rho_1}{\rho_2}) + h_2(\frac{\rho_2}{\rho_3} - 1)) - \frac{C_b|u_3|u_3}{h_3} \tag{6.9}$$

The left hand side of each equation includes a shear term, while the right hand side has layer velocities. Layer velocities must be expressed in terms of shears, by incorporating the transport equation (6.6). If total transport is expressed in terms of each layer speed separately, then each layer speed may be expressed in terms of the shears, thus:

$$u_1 = (q_b - a_2 \cdot U_{21} - a_3(U_{32} + U_{21}))/A \tag{6.10}$$

$$u_2 = (q_b + a_1 \cdot U_{21} - a_3 \cdot U_{32})/A \tag{6.11}$$

$$u_3 = (q_b + a_1(U_{21} + U_{32}) + a_2 \cdot U_{32})/A \tag{6.12}$$

where $A = a_1 + a_2 + a_3$ is the total cross section of the channel. Now the terms representing advective acceleration may be expressed as functions of total transport and shear between the layers. This formulation allows us to drive the model by

specifying barotropic forcing term q_b at all times.

$$q_b(t) = q_{b0} sin(2\pi t/T) + q_m \tag{6.13}$$

where $q_{b0} = u_{b0}/\sqrt{g'H}$ is the tidal barotropic current speed, scaled by an internal wave speed, and q_m is the scaled steady barotropic current, due to the river flow. The M_2 tidal period is T. When the model is run, both q_m and q_{b0} are user-specified, so q_b may be zero, steady or time-dependent.

Equations 6.8 and 6.9 are dimensional, but for modeling purposes it is convenient to nondimensionalize. Layer speeds u_i should be scaled relative to an internal wave speed $\sqrt{g'H}$, but as there are three layers, there could be two relevant values of reduced gravity g'. With the strong stratification seen in the Columbia River estuary, we set $\rho_1 \approx 1000$ kg $\cdot$ m^{-3}, $\rho_2 \approx 1010$ kg $\cdot$ m^{-3}, and $\rho_3 \approx 1020$ kg $\cdot$ m^{-3}; thus

$$g' \approx g\frac{\rho_2 - \rho_1}{\rho_2} \approx g\frac{\rho_3 - \rho_2}{\rho_3}$$

so the same scale speed may be used in each layer. The layer interfaces are defined as isopycnals, so the layer densities and g' are constant with time. The relevant horizontal dimension is the length of a sill or constriction L (1-5 km, depending on the feature of interest), and the vertical dimension is water depth H (about 20 meters). The appropriate time scale is the tidal time period T, which can be empirically related to the topographic scale using:

$$\gamma = \frac{T\sqrt{g'H}}{L} \tag{6.14}$$

which is the distance traveled by an internal wave over a half tidal cycle divided by the topographic scale [Helfrich, 1995]. If $\gamma > 30$, internal adjustments to tidal forcing are very rapid, so the hydraulic problem may be treated as steady state [Armi and Farmer, 1986]. If $\gamma << 1$, the internal tidal motion is much shorter than the sill, and internal hydraulics are no longer relevant. In typical estuarine channels, $\gamma \approx 1 - 10$, and in the Columbia entrance channel, $\gamma \approx 4 - 6$, so both hydraulic and time-dependent effects are significant.

The result of this non-dimensionalization is:

$$\frac{1}{\gamma}\frac{\partial}{\partial t}U_{21} = -\frac{\partial}{\partial x}(\frac{u_2^2}{2} - \frac{u_1^2}{2}) + \frac{\partial h_1}{\partial x} \tag{6.15}$$

$$\frac{1}{\gamma}\frac{\partial}{\partial t}U_{32} = -\frac{\partial}{\partial x}(\frac{u_3^2}{2} - \frac{u_2^2}{2}) + \frac{\partial}{\partial x}(h_2 + \frac{\rho_1}{\rho_2}h_1) - \frac{C_b L}{H}\frac{|u_3|u_3}{h_3} \tag{6.16}$$

where layer speeds u_i are now defined in terms of forcing q_b and vertical shears U_{21} and U_{32}. The baroclinic term has a minus sign because the vertical shear is defined as $u_i - u_{i-1}$. The g' has conveniently dropped out of all terms, and the bottom friction coefficient must be multiplied by L/H. The tidal period also drops out of the expression for $q_b(t)$ (equation 6.13).

We now have two momentum equations (6.15 and 6.16), in which the layer velocities must be expressed using equations 6.10 through 6.12. Now we need two continuity equations to describe the problem completely.

6.2 Continuity Equations

For the three-layer model, imagine two layers separated by a very thin interface. Vertical shear between the layers drives turbulent overturns and creates water of intermediate density. The creation of this water is represented as entrainment from the top and bottom layers into the middle layer. Mixing is irreversible; intermediate density water cannot turn back into fresh or salt water, so the vertical entrainment is one-way. However, lateral advection in the middle layer removes this intermediate density water from the model domain, so the layer does not grow indefinitely.

In the absence of vertical entrainment,the continuity equation for each layer is

$$\frac{\partial}{\partial t}(wh_i) + \frac{\partial}{\partial x}(wh_i u_i) = 0 \tag{6.17}$$

where i is the layer index. Channel width w, layer thickness h_i and speed u_i all vary with distance x along the channel. Vertical mixing creates water of intermediate density, and causes the pycnocline (layer 2) to grow at the expense of the top and

bottom layers, so

$$\frac{\partial h_i}{\partial t} = -\frac{1}{w}\frac{\partial}{\partial x}(w h_i u_i) \pm \text{entrainment} \tag{6.18}$$

This equation is also nondimensionalized using H for h_i, $\sqrt{g'H}$ for u_i and $T = \gamma L/\sqrt{g'H}$, so the entrainment term is multiplied by $L/(H\sqrt{g'H})$. Channel width w is scaled by the width at the narrows. In the Columbia River entrance channel, $H \approx 20$ meters and $g' \approx 0.1$, so $\sqrt{g'H} = O(1)$, and $L/H = O(10^3)$. As entrainment is one-way from the upper and lower layers into the middle layer, the nondimensional continuity equations for the three layers are slightly different:

$$\frac{1}{\gamma}\frac{\partial h_1}{\partial t} = -\frac{1}{w}\frac{\partial}{\partial x}(w h_1 u_1) - \frac{L}{H} e_{\text{above}} \tag{6.19}$$

$$\frac{1}{\gamma}\frac{\partial h_2}{\partial t} = -\frac{1}{w}\frac{\partial}{\partial x}(w h_2 u_2) + \frac{L}{H}(e_{\text{above}} + e_{\text{below}}) \tag{6.20}$$

$$\frac{1}{\gamma}\frac{\partial h_3}{\partial t} = -\frac{1}{w}\frac{\partial}{\partial x}(w h_3 u_3) - \frac{L}{H} e_{\text{below}} \tag{6.21}$$

The entrainment is one-way on ebb; the pycnocline gets thinner due to lateral advection on flood.

There are many possible parameterizations of vertical entrainment; I chose a function of a nondimensional bulk Richardson number, based on experimental work by Ellison and Turner [1959]. They studied entrainment into a bottom density current, but their empirical formulation is also appropriate for pycnocline growth.

$$e_{\text{above}} = |u_2 - u_1| \cdot \frac{0.08 - 0.1 \cdot Ri_{\text{above}}}{1 + 5 \cdot Ri_{\text{above}}} \tag{6.22}$$

$$e_{\text{below}} = |u_3 - u_2| \cdot \frac{0.08 - 0.1 \cdot Ri_{\text{below}}}{1 + 5 \cdot Ri_{\text{below}}} \tag{6.23}$$

where

$$Ri_{\text{above}} = \frac{h_2/2}{(u_2 - u_1)^2}, \quad Ri_{\text{below}} = \frac{h_2/2}{(u_3 - u_2)^2}$$

This entrainment function has a plausible shape (figure 6.2), with a clear cutoff when Ri_{above} or Ri_{below} reaches a critical value of 0.8. However, a laboratory result of this kind (for a fully-turbulent flow) may have to be modified or generalized for high

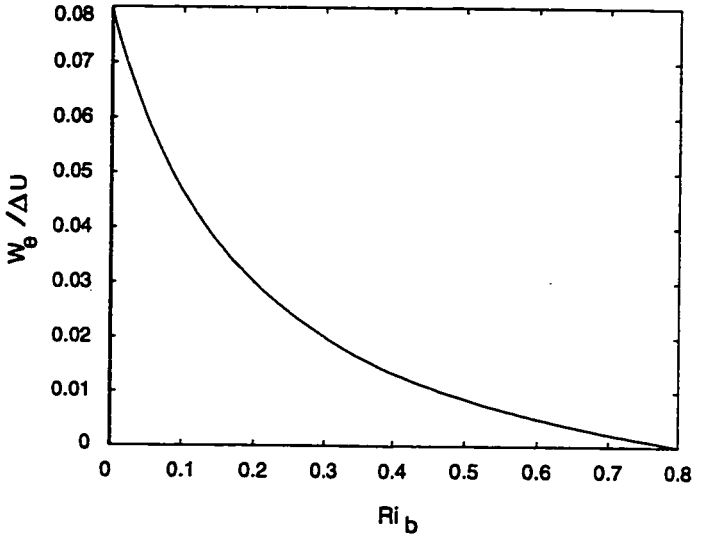

Figure 6.2: Entrainment velocity as a function of bulk Richardson number; maximum W_e is 0.08 times the vertical shear, ΔU after Ellison and Turner [1959].

Reynold's number geophysical flows. This will be discussed in chapter 7. As total transport is conserved, we need only two continuity equations, and the choice of which to eliminate appears to be aesthetic. Numerically, however, large instabilities may develop where a given layer gets very thin. Choice of continuity equations is, therefore, an important numerical issue (section 6.4). Note that there are four differential equations to solve, whereas the two-layer problem requires only two equations.

6.3 Implementation

This model was coded in MATLAB, following the methods used in Helfrich's FORTRAN model. First channel topography is specified; the sides of the channel are vertical and there may be a sill or constriction or both. The user specifies the amplitude of the constriction (cc) and/or sill (cs), and the topography is defined thus:

$$w = 1 + cc \cdot [1 - \exp(-\alpha^2(x - x_c)^2)] \tag{6.24}$$

$$h_s = cs \cdot sech^2(\beta(x - x_s)) \tag{6.25}$$

where x is the (nondimensional) along-channel distance. Channel width $w = 1$ at $x = x_c$, the narrowest point; similarly sill height $h_s = 0$ at $x = x_s$.

The values of x, cc, cs, α and β depend on the channel being emulated. The Straits of Gibraltar are short, deep, and very sharply constricted. To represent a similar topography, Helfrich [1995] used $-2 < x < 2$ and $cc = 4$, so his model channel was four units long, one unit deep and constricted by a factor of 5. The Columbia entrance channel is a few kilometers long and only 20 meters deep, so it has a much higher aspect ratio than the Straits of Gibraltar. The channel is constricted by about a factor of 3 between the entrance jetties and Jetty A, so $cc \approx 2$ for the three-layer model. There is a moderate sill seaward of the constriction in the Columbia, but as noted in chapter 5, this sill has no effect on the two-layer hydraulics. The following calculations include the lateral constriction only.

Helfrich uses radiation boundary conditions

$$\frac{\partial \phi}{\partial t} - c\frac{\partial \phi}{\partial x} = 0$$

where ϕ is any variable (speed or layer thickness) and c is a phase speed near the boundaries, calculated according to Orlanski [1976]. This condition allows information (and water) to propagate out of, but not back into the model domain. Thus, for the two-layer model, the layer interface near the boundaries tends to the maximal steady exchange solution. For the three layer model, the interface positions near the boundaries tend to change relatively little from the initial conditions.

The physical boundary conditions, such as density at either end of the model domain are not specified in this model. Rather, they are be implicit in the initial conditions. In the two-layer case, the initial layer interface should be high on the seaward (dense) end of the channel, and low on the landward (less dense) end. The initial interface represents the steady solution with no barotropic forcing, and its shape depends on channel topography. For a straight channel, the interface is a straight line, whereas channel constrictions distort the interface into a smooth s-curve. Initial shear

must also be specified, so that seaward-moving fresh water overlies landward moving salt water; $|u_{\text{bottom}} - u_{\text{top}}| = 1$ is a good starting point. In my coordinate system, landward currents are positive, so $u_{\text{bottom}} > 0$ and $u_{\text{top}} < 0$.

The initial conditions for the three-layer model are analogous to those for the two-layer model. The shears U_{21} and U_{32} are each half of the two-layer shear. Initial layer interfaces may either parallel the single interface from the two-layer case, or diverge from it. I have experimented with both straight and curved interfaces, and found that steady solution to the three-layer model gives interfaces which are s-curved and approximately parallel. Accordingly, curved parallel interfaces are used as initial conditions in all model runs.

6.4 Numerical Stability

Two versions of the three layer model were made, with slightly different time stepping schemes and different stability. Both models used the same physics and channel topography and the same time stepping scheme to solve the momentum equation. The models used different schemes to solve the continuity equation and different formulations of bottom friction.

There are two basic criteria for stability of a layer model. First, a water parcel must not propagate across an entire cell in a single time step, or mass will be transmitted more rapidly than the information needed for the next time step. This gives rise to the Courant-Friedrichs-Lewy (CFL) stability criterion:

$$c\frac{\Delta t}{\Delta x} < 1 \tag{6.26}$$

where c is a typical water propagation speed. For this model, $c \approx q_{b0} \approx 1$, so the CFL criterion simply requires that $\Delta t < \Delta x$. For both models, I used $\Delta t = 0.05\Delta x$.

The second stability criterion is that a given cell cannot be depleted in a single time step, or a layer may acquire negative thickness. In practice, stability is threatened any time a layer gets very thin ($h_i < 0.01$). Solving the continuity equation seems

to preserve the stability of a given layer, but this is done for only two of the three layers. The third layer thickness is calculated from the total water depth. It would seem appropriate to solve continuity for the thin layers, but all three layers can be thin. The surface layer is thin at the seaward end of the channel, the bottom layer is thin at the landward end of the channel, and the middle layer can be thin everywhere. I made two versions of the model using different time stepping schemes for different combinations of layers.

Both versions of the three-layer model use a two-step Lax-Wendroff time stepping scheme for the momentum equations [Press *et al.*, 1992], but they have different schemes for continuity. The 'Lax' model uses the Lax-Wendroff scheme for continuity. The continuity equation was solved for layers 2 and 3; the thickness of layer 1 was calculated from the total water depth. The 'Upwind' model used an upwind differencing scheme for the continuity equations. In upwind differencing, the expression of the spatial derivative depends on the direction of the current, so that each grid point is compared to the one 'upwind' of it. The continuity equation was solved for layers 1 and 3; steady entrainment was required to keep layer 2 from collapsing.

The two models perform quite similarly, and both replicate the mid-depth jet in the flood current. The Upwind scheme was more stable in the presence of strong bottom friction. Both models are unstable for for $\gamma > 1$. As noted in the previous chapter $\gamma L/H \approx 1000$, so the models should be run with an aspect ratio ($L/H \approx 1000$) which represents the full length of the estuary.

Chapter 7

THREE LAYER MODEL RESULTS

The purpose of this model is to replicate the tidally-varying circulation in the Columbia River, with particular interest in the vertical distribution of along-channel currents. Peak ebb currents should be strongest near the surface. Early flood currents should be strongest near the bottom and move upward through the water column so that peak flood currents are strongest at the surface. There should be a brief period during which flood currents show a mid-depth maximum. The pycnocline should rise and fall with the tides, and be thicker on ebb than on flood.

7.1 Initial Tests

Preliminary model tests were run to isolate the effects of barotropic forcing and vertical entrainment. For these tests a moderate channel constriction was used ($cc = 2$, figure 7.1a). First, the model was run to a steady state with no imposed barotropic current and no entrainment into the middle layer (figure 7.1b). The middle layer collapses, leaving a two-layer maximal exchange flow [Armi and Farmer, 1986]. This collapse is due to significant lateral advection out of the middle layer and is consistent with laboratory experiments (P. MacCready, personal communication). Two-layer exchange is a natural and stable result for inviscid flow driven by a streamwise density gradient or a tilted layer interface.

Next, a vertical entrainment was added. The observed pycnocline in the Columbia River entrance grows by $\approx 10^{-4}$ m $\cdot$ s^{-1}on ebb, whereas the maximum growth rate implied by equations 6.22 and 6.23 is $0.08 \cdot U$, or about 0.08 m $\cdot$ s^{-1}. The laboratory

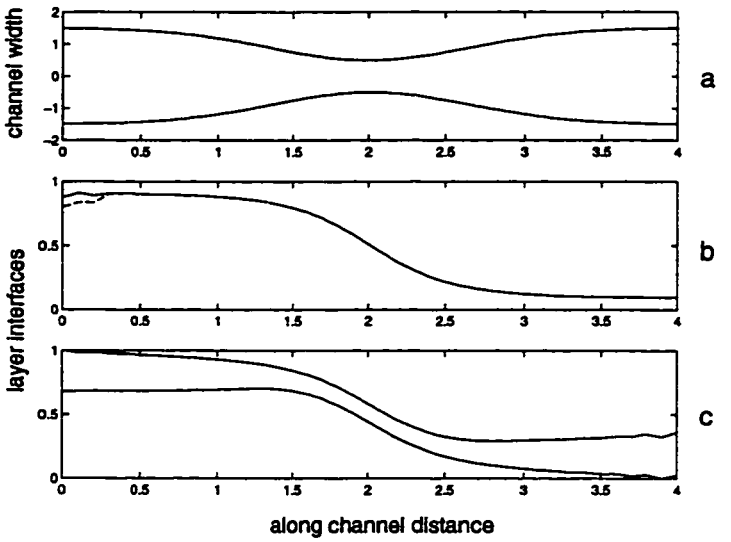

Figure 7.1: Three layer model results, no barotropic transport. Plan view of the channel is in (a); vertical sections are in (b) and (c). In the absence of vertical entrainment (b), the middle layer collapses and the result is a two-layer maximal exchange. Vertical entrainment (c) is strongest near the model boundaries, so the pycnocline is thinnest at the channel constriction.

experiment used a fully turbulent flow, into which entrainment is quite rapid. By contrast, the turbulence in a geophysical flow is localized to layer interfaces, so an estuarine pycnocline grows more slowly than does a laboratory flow. The entrainment function was accordingly multiplied by 0.01-0.02, which gives a plausible pycnocline thickness in the model. The model run in figure 7.1c used an entrainment scaling of 0.012. The resulting pycnocline is thin near the constriction and thick near the edges of the model domain, due to control at the constriction; this shape is identical to that found by K. Winters (personal communication) using a three-dimensional turbulence closure model. The shape of the pycnocline may be explained in terms of along-channel variations in vertical shear. Near the seaward (landward) end of the model the top (bottom) layer becomes very thin and moves rapidly. Vertical shear in these areas is quite strong, causing rapid entrainment into the pycnocline. Near the constriction, both upper and lower layers are thick and slow moving, so vertical entrainment is much slower there.

The model was run without entrainment in the last model test, but with a tidally varying imposed barotropic transport ($\gamma = 1$). Again, the middle layer collapsed, and the three-layer results closely resemble two-layer results with similar parameters (figure 7.2). Each subplot shows a time series (four tidal cycles) of interface positions at the narrows. Channel topography is as above ($cc = 2$). The strength of the forcing is different for each plot; q_{b0} is 0.5, 1 and 2. The two-layer results (solid lines representing a single interface) show that the landward and seaward migration of the interfaces is expressed as a vertical oscillation at the narrows; the oscillation increases approximately linearly with q_{b0}. Note that even for $q_{b0} = 2$, the interface does not reach the surface or bottom, as it would for a steady $|q_m| = 1$.

Three-layer model results are plotted as dashed lines representing both layer interfaces in figure 7.2. For each model run, the interfaces were given an initial separation of $h_2 = 0.05$, and the middle layer collapsed within one tidal cycle. In the range of forcing found in the Columbia River entrance channel ($q_{b0} = 1 - 2$), the three-layer model without entrainment is in reasonable agreement with the two-layer model.

7.2 The Three Layer Columbia River

The following model runs represent the Columbia River entrance channel, using the Lax version of the model. The channel dimensions, tidal currents and river flow are based on observations. The channel constriction has an e-folding scale of 4 kilometers (aspect ratio $L/H = 200$), and constricts the flow by about a factor of 3 ($cc = 2$ and $\alpha = 1.07$, equation 6.24). In the Columbia River entrance channel, the tidal excursion is about 4 times the topographic scale ($\gamma = 4$), but this model is stable only for $\gamma = 1$.

The next three figures show results for different combinations of barotropic forcing and bottom friction. For figure 7.3, the model was run with a strong, purely tidal current ($q_b0 = 1.2, q_m = 0$), and no bottom friction ($C_b = 0$). For figure 7.4, bottom friction was added ($C_b = 3 \cdot 10^{-3}$), and for figure 7.5 a steady barotropic river current

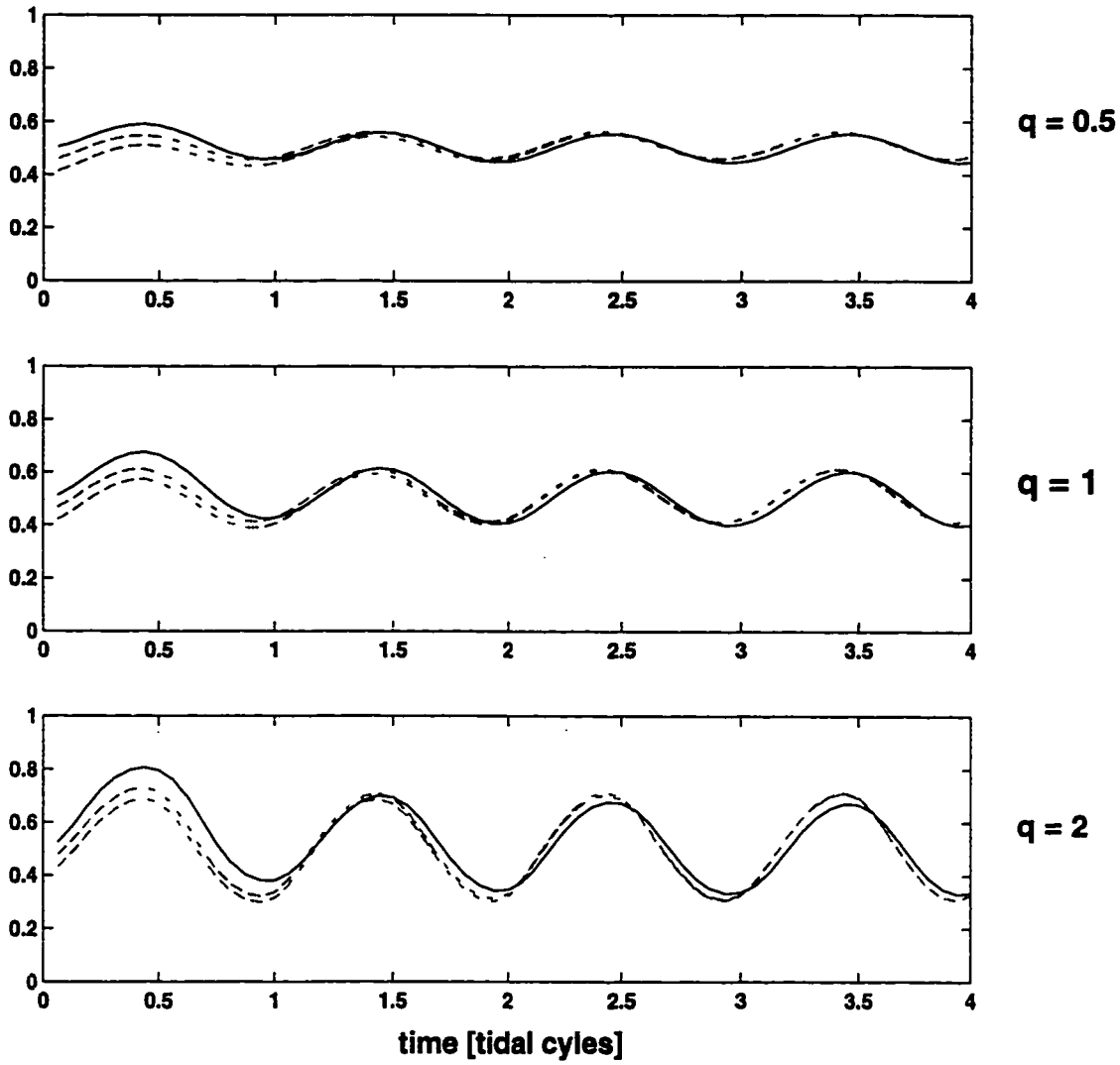

Figure 7.2: Three-layer model results with no entrainment into the middle layer. Dashed lines are vertical positions of layer interfaces at constriction, plotted against time. Increasing tidal barotropic forcing increases the vertical oscillation of the layer interfaces. Solid lines are the interface in an analogous two-layer model.

was added ($q_b 0 = 1.2, q_m = -0.3, C_b = 3 \cdot 10^{-3}$). In each figure, all subplots represent vertical sections, with the horizontal axis being along-channel and fresh water to the right. The two layer interfaces are overlaid with velocity vectors. Each row represents a different stage of the tidal cycle: slack water, peak flood, slack water and peak ebb, respectively.

A model result with tidal barotropic forcing and vertical entrainment, but no bottom friction is shown in figure 7.3. The overall shape of the pycnocline resembles the two-layer interface predicted by Armi and Farmer [1986] for a maximal exchange flow, and the whole pycnocline rises and falls slightly with the tides. The pycnocline is generally thin near the constriction and thick near the edges of the model domain, as discussed above. The current vectors in each layer follow the tidal currents. At both slack waters (row 1 and row 3), there is a simple two-layer exchange flow. At peak flood (row 2), currents are strongest in the bottom layer and slightly weaker in the middle layer. At peak ebb (row 4), the current profile is reversed, being strongest in the upper layer. There is clear symmetry between the flood and ebb circulation patterns.

The addition of bottom friction (figure 7.4) breaks down the symmetry between flood and ebb. The whole pycnocline is displaced upward and landward relative to the frictionless case, as seen also in the two-layer model 5.3 and in the analytic model of Pratt [1986]. Bottom friction slows the bottom layer(layer 3) and has the greatest effect at the landward end of the model channel, where layer 3 is thinnest and fastest. Relative to the frictionless case, reduced transport in layer 3 raises the pycnocline, and reduced shear between layers 2 and 3 inhibits pycnocline growth. Bottom layer currents are weak at all stages of the tide, so the two-layer exchange is no longer apparent at slack water. At peak flood (row 2), currents are fastest in the pycnocline, landward of the constriction. This is the mid-depth jet which inspired the three-layer model.

The addition of steady barotropic transport to represent the river flow (figure 7.5)

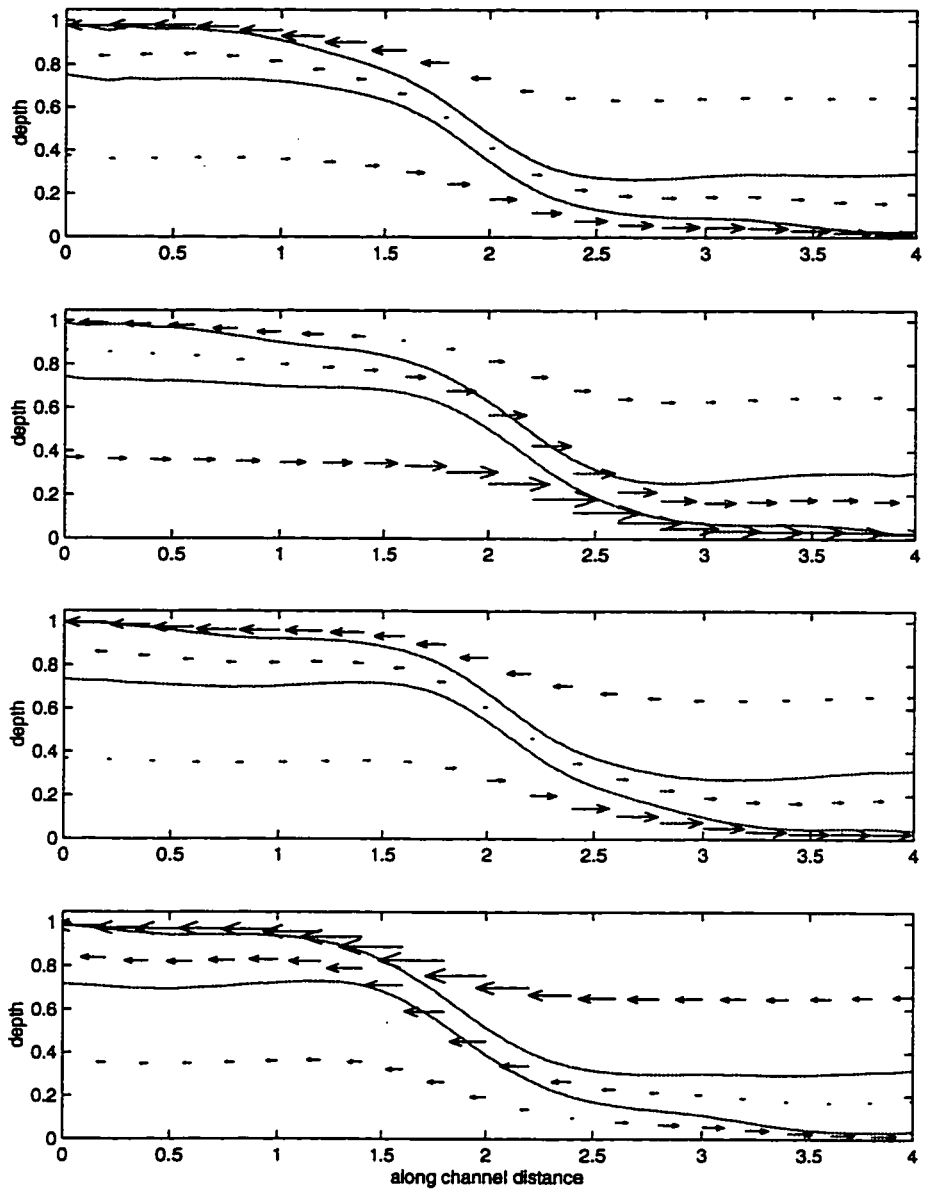

Figure 7.3: 3-layer model result with mass entrainment into the pycnocline, frictionless, imposed tidal barotropic transport $q_{b0} = 1.2, q_m = 0$. Subplots are along-channel sections representing slack water, flood, slack water and ebb. Flood and ebb circulation are symmetric.

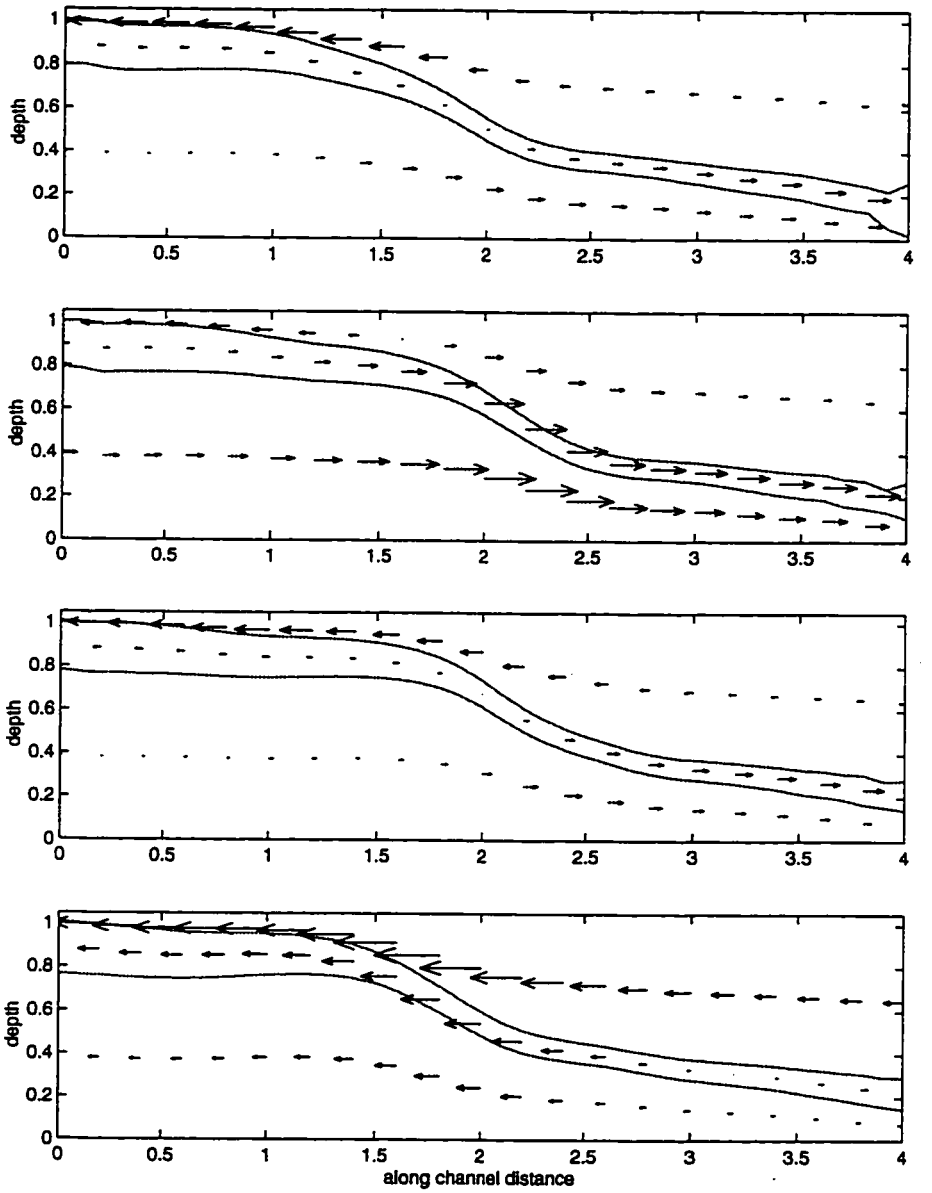

Figure 7.4: 3-layer model result with mass entrainment into the pycnocline, bottom friction $C_b = 3 \cdot 10^{-3}$, imposed tidal barotropic transport $q_{b0} = 1.2, q_m = 0$. There is a weak mid-depth maximum in the flood currents at the landward end of the channel, and the flood/ebb symmetry has broken down.

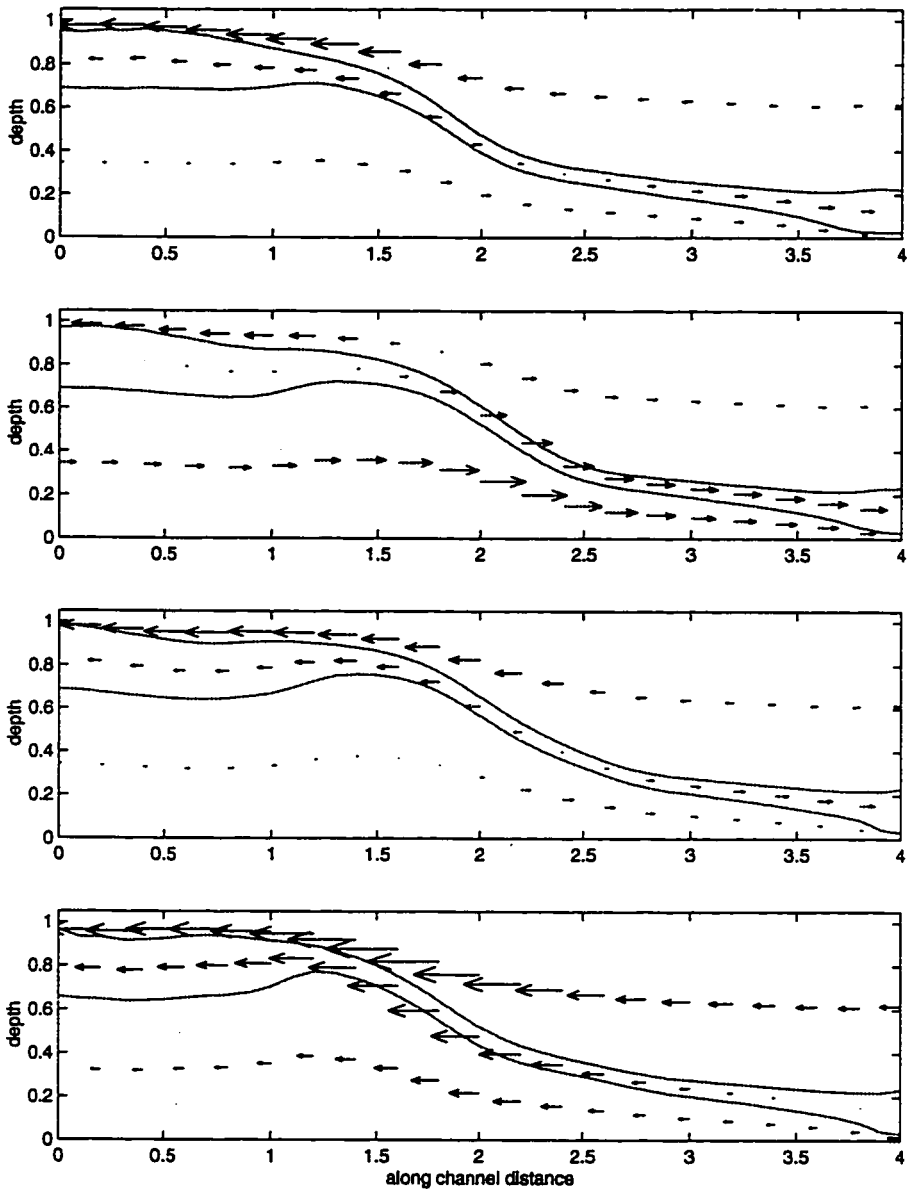

Figure 7.5: 3-layer model result with mass entrainment into the pycnocline, bottom friction $C_b = 3 \cdot 10^{-3}$, imposed tidal and fluvial barotropic transport $q_{b0} = 1.2, q_m = -0.3$. Circulation is only slightly different from previous case.

has a less dramatic effect on model results. Due to the river currents, ebb currents are stronger and flood currents weaker than the purely tidal case. Stronger ebb currents cause enhanced vertical mixing near the seaward end of the channel, and some bore propagation along the lower interface. Peak flood currents are still strongest in the pycnocline. By contrast wth the classical two-layer model [Armi and Farmer, 1986; Farmer and Armi, 1986], there is no symmetry between ebb and flood.

7.3 Tidally Averaged Volume Transport

Three layer model results are the thickness and speed of each layer, which vary along-channel and with time. Volume transport in a given layer is wh_iu_i, where w is channel width and u_i and h_i are the layer speed and thickness. The tidal average of the layer volume transports shows the importance of vertical stratification and the river flow (figure 7.6). Transport out of the estuary in the upper layer dominates the tidally averaged picture.

Figure 7.6a shows tidally averaged interface positions and layer transports for $q_{b0} = 1.2, q_m = -0.3$ and $C_b = 3 \cdot 10^{-3}$. When tidal motions are averaged out, the pycnocline passes through the center of the model domain and is thinnest at the constriction. Average volume transport is landward in the lower layer and strongly seaward in the surface layer. The difference between the landward and seaward transports is due to the river flow. Transport in the middle layer is weakly divergent. The crucial aspects of this circulation are shown schematically in 7.6b. Along-channel volume transports are indicated by the straight arrows, and vertical entrainment by the curved arrows. Although there is little volume transport in the thinner portions of layers 1 and 3, speeds there are quite high. Strong vertical shears drive entrainment into the pycnocline from layer 1 at the seaward end of the model domain, and from layer 3 at the landward end of the domain.

The total volume transport ($\sum wh_iu_i$) varies with time but must, by the rigid-

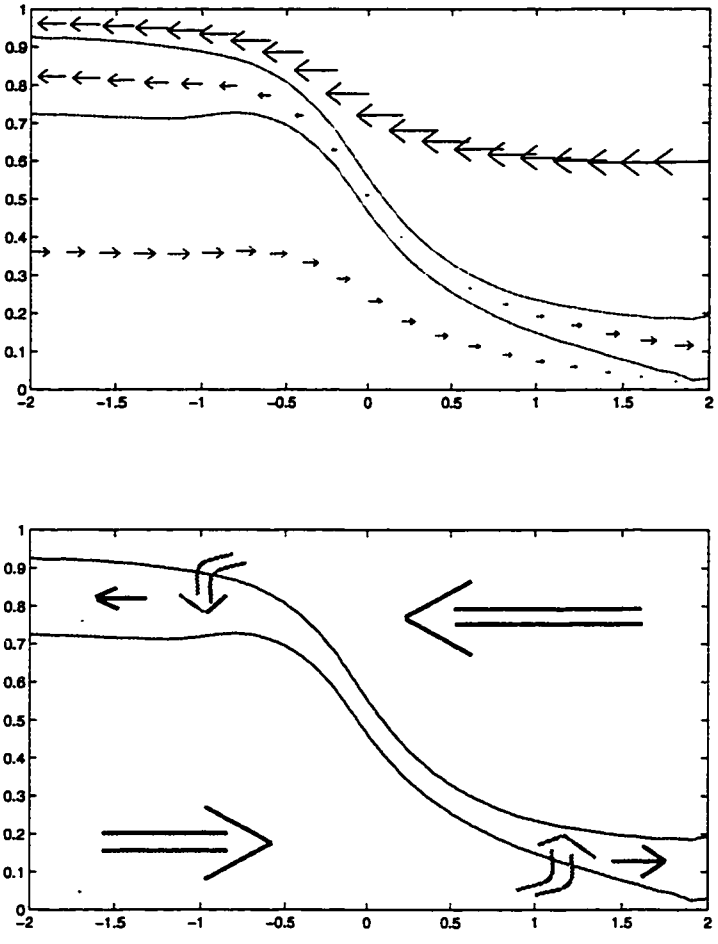

Figure 7.6: Tidally averaged volume transport is landward in the bottom layer, seaward in the surface layer and divergent in the pycnocline. Top: model results using $q_{b0} = 1.2, q_m = -0.3, \gamma = 1$ and $C_b = 3 \cdot 10^{-3}$. Bottom, schematic showing vertical entrainment into the pycnocline as curved arrows.

lid assumption, be conserved along-channel. Its tidal average must be equal to the imposed mean barotropic transport q_m.

7.4 Conclusions

Initial tests of the three-layer model show that, in the absence of vertical entrainment, the middle layer collapses, so the model behaves identically to a two-layer model. Vertical entrainment is strongest near the landward and seaward ends of the model channel, so the pycnocline is thinnest near the constriction, consistent with hydraulic control at the constriction.

The three-layer model provides some useful insights into the effects of bottom friction and river flux on a tidal exchange flow. In a purely tidal case, without bottom friction, there is clear symmetry between the flood and ebb circulation. Ebb currents are strongest near the surface at the seaward end of the channel, and flood currents are strongest near the bottom at the landward end of the channel. The pycnocline moves with the tides, but its basic shape is consistent with a two-layer maximal exchange. When bottom friction is added to the model, this symmetry breaks down. Flood currents, being retarded by bottom friction, are weaker than ebb currents. Near peak flood, the strongest currents are seen at mid-depth, consistent with observations. Conservation of transport in the lower layer raises the pycnocline landward of the constriction, so its shape is no longer symmetric. The addition of river flux has a less significant effect on the symmetry of the flow.

Chapter 8

COMPARISON OF THREE-LAYER MODEL WITH OBSERVATIONS

The three-layer model produces a small mid-depth jet on flood, which is qualitatively consistent with observations. However, the observed early flood currents (figure 3.3) have a mid-depth maximum which extends from the channel constriction to the upstream limit of observation. Observations also reveal a mid-depth maximum in salinity transport at peak ebb and peak flood (figure 8.3); this is not replicated by the three layer model with moderate bottom friction. For better agreement with observations, bottom friction must be increased substantially.

The bottom roughness coefficient used in chapter 7 ($C_b = 3 \cdot 10^{-3}$, [Geyer, 1985]) is well suited to a one-layer model, but less appropriate for a multi-layer model. The bottom roughness coefficient is formulated as

$$C_b = \left(\frac{1}{k} ln \frac{z_m}{z_0}\right)^{-2} \tag{8.1}$$

where $k = 0.41$ is von Karman's constant, $Z_0 = 0.01$ m is a skin thickness for bottom roughness and z_m is the distance above the bottom at which the frictional effect is measured. In figure 8.1 it is apparent that $C_b = 3 \cdot 10^{-3}$ is appropriate for a 20 meter water depth. However, if the effect of bottom friction on the bottom layer alone is considered, a larger roughness coefficient must be used, ($C_b = 4.4 \cdot 10^{-3}$ for $z_m = 5$ m).

Another factor affecting the coefficient of bottom friction is the channel cross section. The real entrance channel of the Columbia River is triangular in section, but it is represented in the model with a rectangular cross section. The model channel

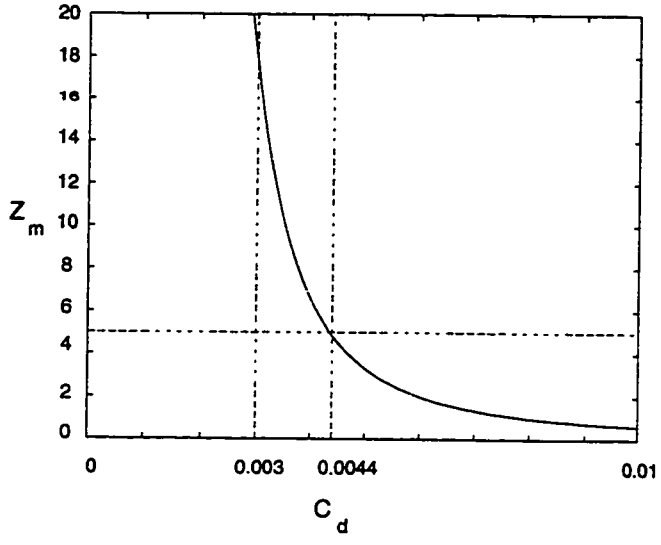

Figure 8.1: The bottom roughness coefficient decreases with distance above the bottom. At $z_m = 20$ meters above the bottom, $C_b = 3 \cdot 10^{-3}$. At $Z_m = 5$ meters above the bottom, $C_b = 4.4 \cdot 10^{-3}$.

thus has twice the area of the observed channel. For model transport to be equal to observed transport, model currents must be half of observed currents. Bottom friction is $C_b|u|u$, so for the same frictional effect, C_b must be multiplied by four, giving $C_b = 1.2 \cdot 10^{-2}$. This value was used for the results which follow.

The aspect ratio of the channel multiplies the terms for vertical entrainment and bottom friction. Bottom friction is more important in a long, shallow channel, as is also true in the real world. The following results use aspect ratio $L/H = 800$, indicating a topographic e-folding length scale of 16 km, so the model channel (length $4L$) is somewhat longer than the estuary. The model pycnocline intersects the surface at the seaward end of the model channel; this represents the leading edge of the plume in the ocean. The results of this model compare very well with observations from the Columbia River entrance channel. Along-channel sections are shown in figure 8.2, and time series are shown in figures 8.4 and 8.5.

8.1 Along-Channel Sections

The modeled along-channel distribution of density and currents compares well with observations. Figure 8.2(top) shows a measured along-channel section of density and current speed from the Columbia River entrance channel on early flood. Fresh water is to the right, the vertical dashed line represents the constriction due to an intruding lateral jetty (Jetty A, figure 1.3), and there is a moderate sill just seaward of the jetty. The observed pycnocline is quite thick near the seaward end of the section and much thinner near the channel constriction, where it drops sharply due to hydraulic control. The along-channel current speed is greatest near jetty A, about 1.4 $m \cdot s^{-1}$at mid depth. The depth of maximum u increases landward, being 5-10 meters at jetty A and 15-20 meters at kilometer 4. The model is driven by an imposed barotropic transport equal to the sum of a tidal reversing current with an amplitude of 1.2 $m \cdot s^{-1}$and a steady river current of -0.3 $m \cdot s^{-1}$.

Model results at peak flood are shown in figure 8.2, bottom. The pycnocline drops gently toward the landward end of the channel, consistent with hydraulic control theory. The thinnest and steepest part of the pycnocline is just landward of the constriction; this offset is due to bottom friction [Pratt, 1986]. As noted in chapter 5, the sill should not affect the internal hydraulics [Farmer and Armi, 1986]. Currents are strongest in the pycnocline, which is the desired result.

8.2 Salinity Transport

8.2.1 Time Series

The modeled tidal variations in salinity transport compare well with observations. Observed along-channel currents (figure 8.3b) are strongest at the surface at peak flood (landward, $u > 0$) and peak ebb (seaward, $u < 0$). This contrasts with the two-layer inviscid model, in which flood currents are strongest at the bottom. Observed

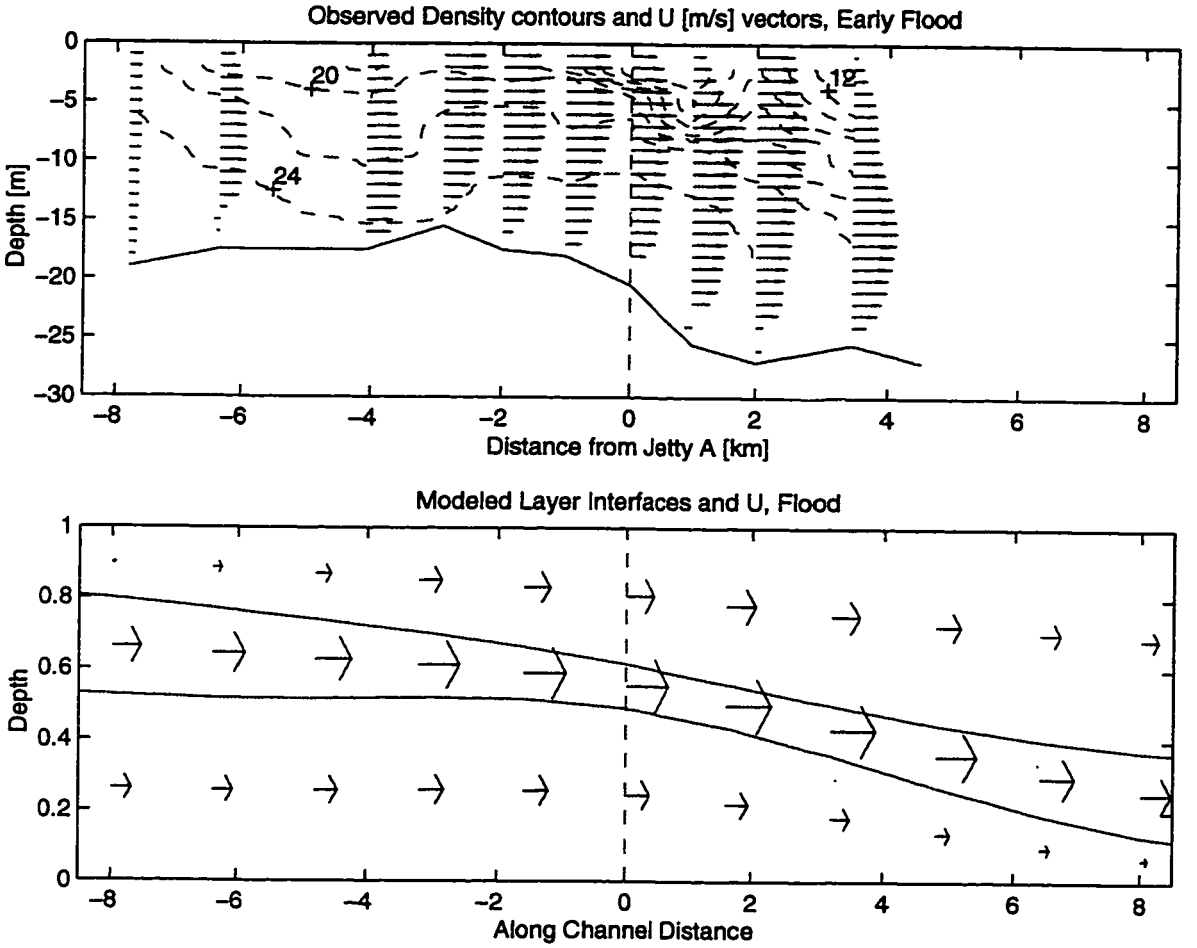

Figure 8.2: Comparison of observations and model, on flood; along channel sections with fresh water to the right.Both observations and model show a clear mid-depth maximum in the currents. The pycnocline is thinnest at the constriction, and drops most steeply just landward of the constriction.

currents move upward through the water column during the course of the flood. At the end of ebb (1400-1500 hours), flood currents are first seen near the bottom, and by peak flood (1700-1800 hours), currents are strongest near the surface. As salinity increases from the top down and currents generally increase from the bottom up, salinity transport ($u \cdot s$) is strongest at mid-depth on both ebb and flood (figure 8.3c). This is local transport, not vertically integrated. The peak seaward transport is -28 psu $m \cdot s^{-1}$, the peak landward transport is 22 psu $m \cdot s^{-1}$and the average transport between times 0727 and 2017 (about one tidal cycle) is 1.5 psu $m \cdot s^{-1}$. Thus, the landward and seaward salinity transport are in rough balance, which is also apparent from the plot. Under conditions of higher runoff, the salt is washed out to sea, and under lower runoff, the salt builds up again, but these observations happen to show a near balance.

The modeled time series of salinity at the narrows (figure 8.4a) is qualitatively similar to observations. The pycnocline is nearest the surface at the end of flood and nearest the bottom at the end of ebb. The range of vertical oscillation is not as great as observed, nor is the pycnocline thicker on ebb and thinner on flood. The behavior of the pycnocline is better simulated by the two-layer model (figure 5.5). However, the two-layer model cannot replicate a mid-depth or near surface maximum in the flood current.

Modeled time series of currents and salinity transport may be represented as contour plots (figure 8.4b,c); these plots have low vertical resolution and must not be over-interpreted. These time series contours simulate the observations quite well. Peak ebb currents (dashed lines) are > 1.5 $m \cdot s^{-1}$at the surface, as observed. Peak flood currents are > 1 $m \cdot s^{-1}$at mid-depth; surface currents are actually slightly faster than bottom currents, but the contour plot does not resolve the difference. Salt transport is strongest (> 24 psu $m \cdot s^{-1}$) at near mid-depth on peak flood and peak ebb, as observed.

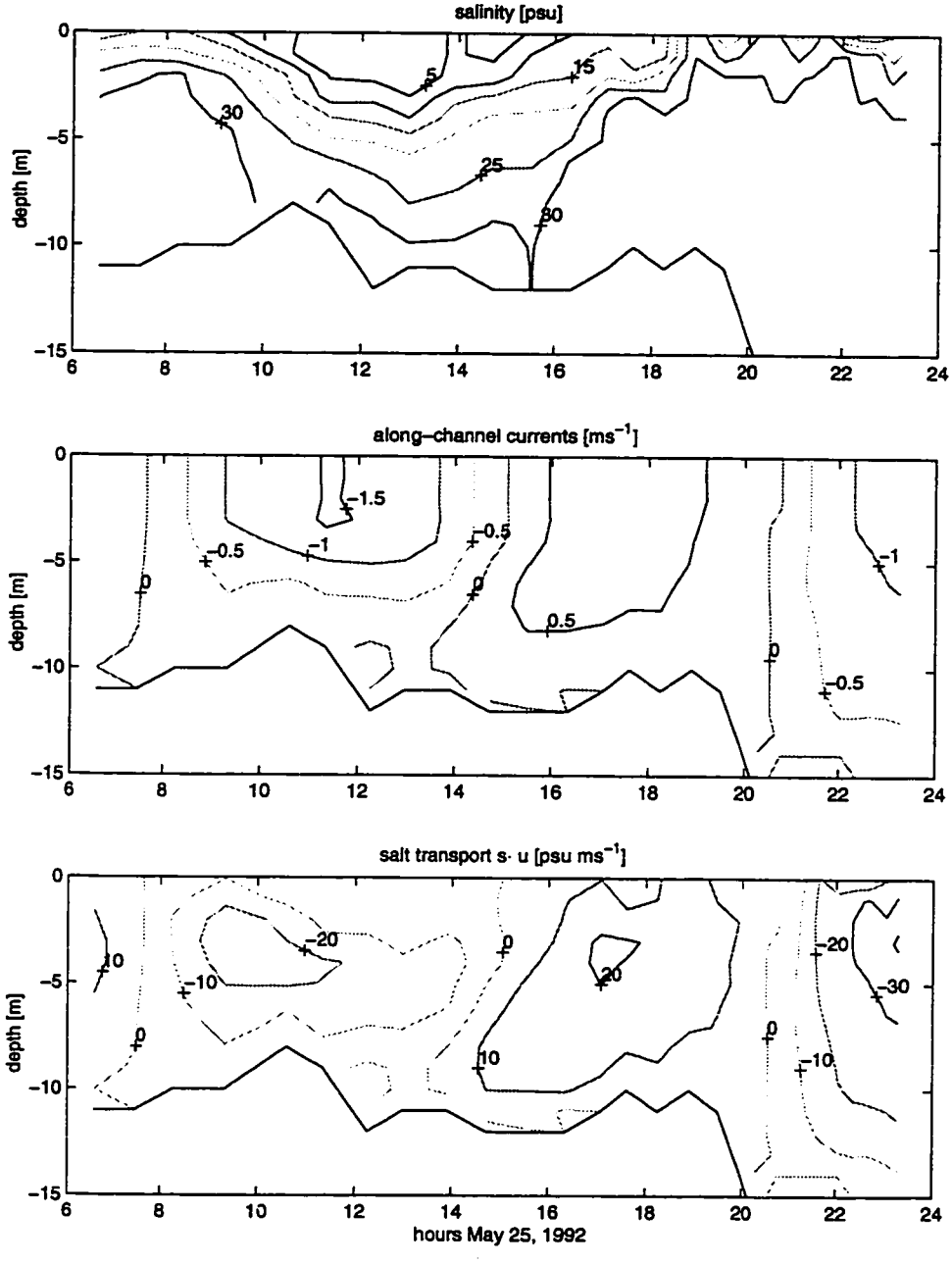

Figure 8.3: Time series of observed salinity (a), currents (b) and salinity transport (c). The pycnocline drops and thickens on ebb, then rises and thins again on flood. Peak flood and ebb currents are strongest near the surface, but early flood currents are strongest near the bottom. Transport is thus strongest at mid-depth on peak flood and peak ebb.

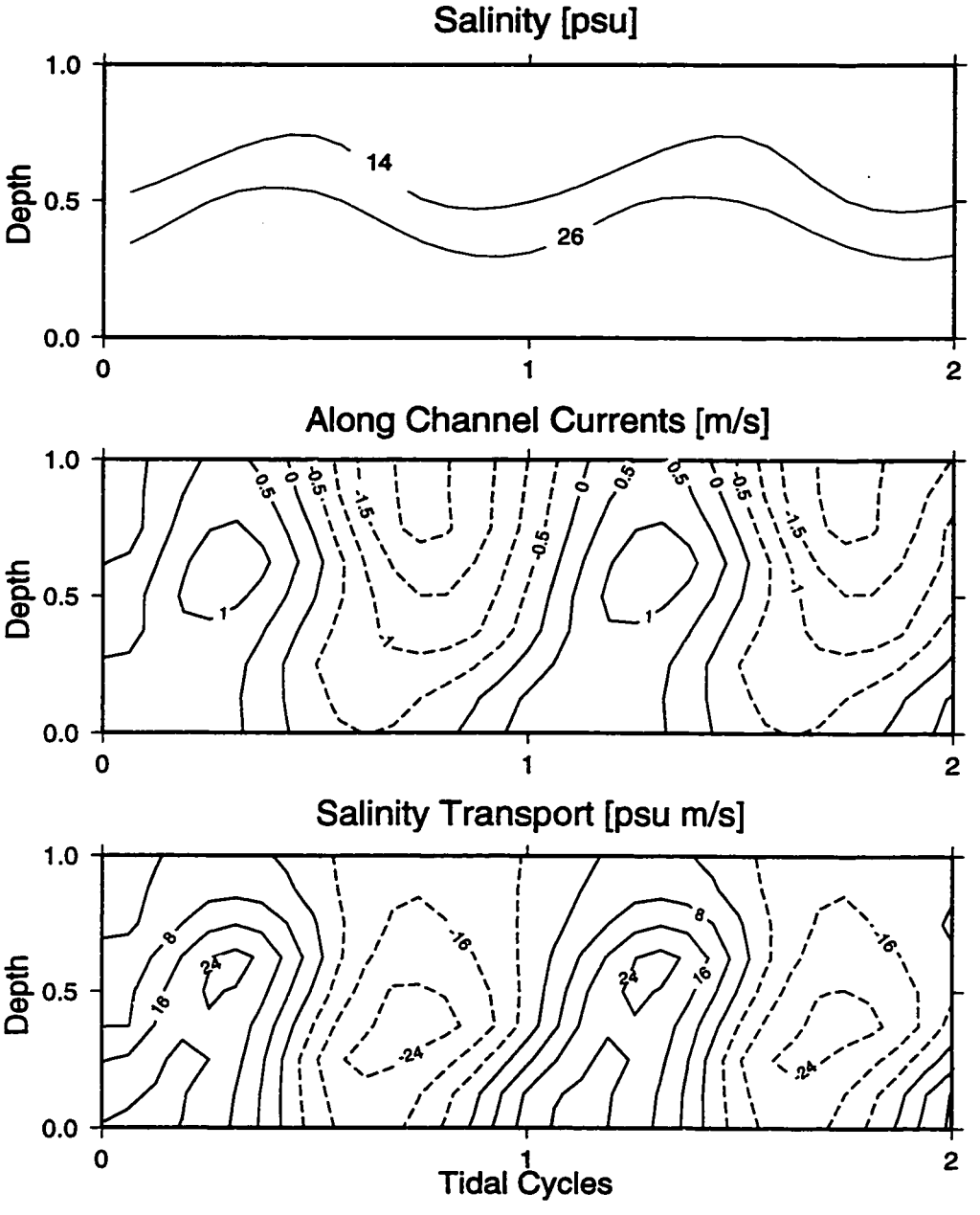

Figure 8.4: Time series of modeled salinity (a), currents (b) and salinity transport (c). The modeled pycnocline does not quite match the observed range of thickness and vertical oscillation. Along channel currents are strongest at the surface on ebb and at mid-depth on peak flood. Salinity transport is strongest at mid-depth, as observed.

8.2.2 Tidally Averaged Salinity Transport

The tidally averaged salinity transport depends upon the balance of imposed tidal currents and river flow. If the imposed barotropic transport reverses tidally (no river flow), salt water is carried into the estuary on flood and fresh water is carried out on ebb, so there is net landward transport of salinity. Net seaward volume transport may or may not drive net seaward transport of salinity. This is similar to the Columbia River estuary, whose salinity and stratification change on a time scale of days to weeks. Salt is washed out to sea by strong runoff and builds up again under low river flow conditions. Over a single tidal cycle, the net salt transport through the entrance channel is usually nonzero.

Tidally averaged salinity transport was calculated for the model runs shown in figures 7.3 through 7.5, and 8.2. assuming that layer salinities were $s_1 = 8$, $s_2 = 20$ and $s_3 = 32$ psu, consistent with observations. Along-channel currents, u_i were multiplied by $\sqrt{g'H} \approx 1 \text{ m} \cdot \text{s}^{-1}$. The vertically averaged salinity transport (in psu $\text{m} \cdot \text{s}^{-1}$) is

$$T_s = (u_1 h_1 s_1 + u_2 h_2 s_2 + u_3 h_3 s_3)/H; \tag{8.2}$$

this is directly comparable with the vertically averaged salinity transport from observations.

The salinity transport observations in figure 8.3 were made when the tidal average salinity transport was near zero; a model with similar tidal and river fluxes should also produce a near-zero salinity transport. In table 8.1, q_{b0} is the imposed tidal transport, which is nondimensional, but equal in magnitude to the observed tidal current, 1.2 $\text{m} \cdot \text{s}^{-1}$. Steady river flux is q_m and the bottom roughness coefficient is C_b. The last three columns represent the maximum landward (flood) salinity transport, the maximum seaward (ebb) transport and the tidal mean. In the absence of bottom friction or river currents, there is significant net salinity transport into the estuary ($T_s(\text{mean}) \approx 0.23 \cdot T_s(\text{flood})$). Moderate bottom friction reduces this transport by

Table 8.1: Salinity transport $\sum(u_i h_i s_i)/H$ [psu m $\cdot$ s^{-1}]. The bottom roughness coefficient, C_b cannot be measured; it only has meaning in a model. The large bottom friction (*) is accompanied by an increased aspect ratio.

	q_{b0}	q_m	C_b	Flood	Ebb	Mean
Model Results	1.2	0.0	0.0	32.9	-15.6	7.6
	1.2	0.0	$3 \cdot 10^{-3}$	32.7	-19.2	5.9
	1.2	-0.3	$3 \cdot 10^{-3}$	25.1	-23.1	0.2
	1.2	-0.3	$12 \cdot 10^{-3}$*	18.6	-20.9	-2.0
Observations	1.2	-0.3	???	16.5	-18.4	≈ 1.5

30%, but does not eliminate it. The addition of a river flow brings the net transport very near zero. When the bottom friction is increased, T_s(flood) and T_s(ebb) are close to the observed values, but there is net seaward salinity transport. The optimal model must include both tidal currents and river flux, and have bottom friction in the range of $C_b \approx (3 - 12) \cdot 10^{-3}$.

Bottom friction reduces mean salinity transport into the estuary, and the amount of transport reduction depends on the number of layers in the model. The thicker the lower layer, the greater the relative effect of bottom friction. So, in the two-layer model, tidally averaged salt transport is reduced by 70%, significantly more than the 20% reduction seen in the three-layer model. A continuously stratified water column would be still less sensitive to bottom friction.

8.3 Bulk Richardson Number

Observations show that the bulk Richardson number is less than 0.3 during ebb, when mixing is strong, and more than 1 on flood. The bulk Richardson number, $Ri_b = h_2/(u_3 - u_1)^2$ was calculated from the three-layer model, and closely simulates the observed bulk Richardson number. In figure 8.5, the first column is observations (see

figure 4.4) and the second column is model results. The rise and fall of the pycnocline is imperfectly modeled, but along-channel currents fit observations remarkably well. Upper layer currents (solid line) are more strongly landward than lower layer currents (dashed line) only for a brief period on late flood. The greatest vertical shear is seen near peak ebb, and $Ri_b < 0.3$ at that time. By contrast with the assumption used to calculate pycnocline thickness from the two-layer model, $Ri_b > 1$ on most stages of the tide. It is intriguing that the best simulation of pycnocline thickness is not the best simulation of Ri_b.

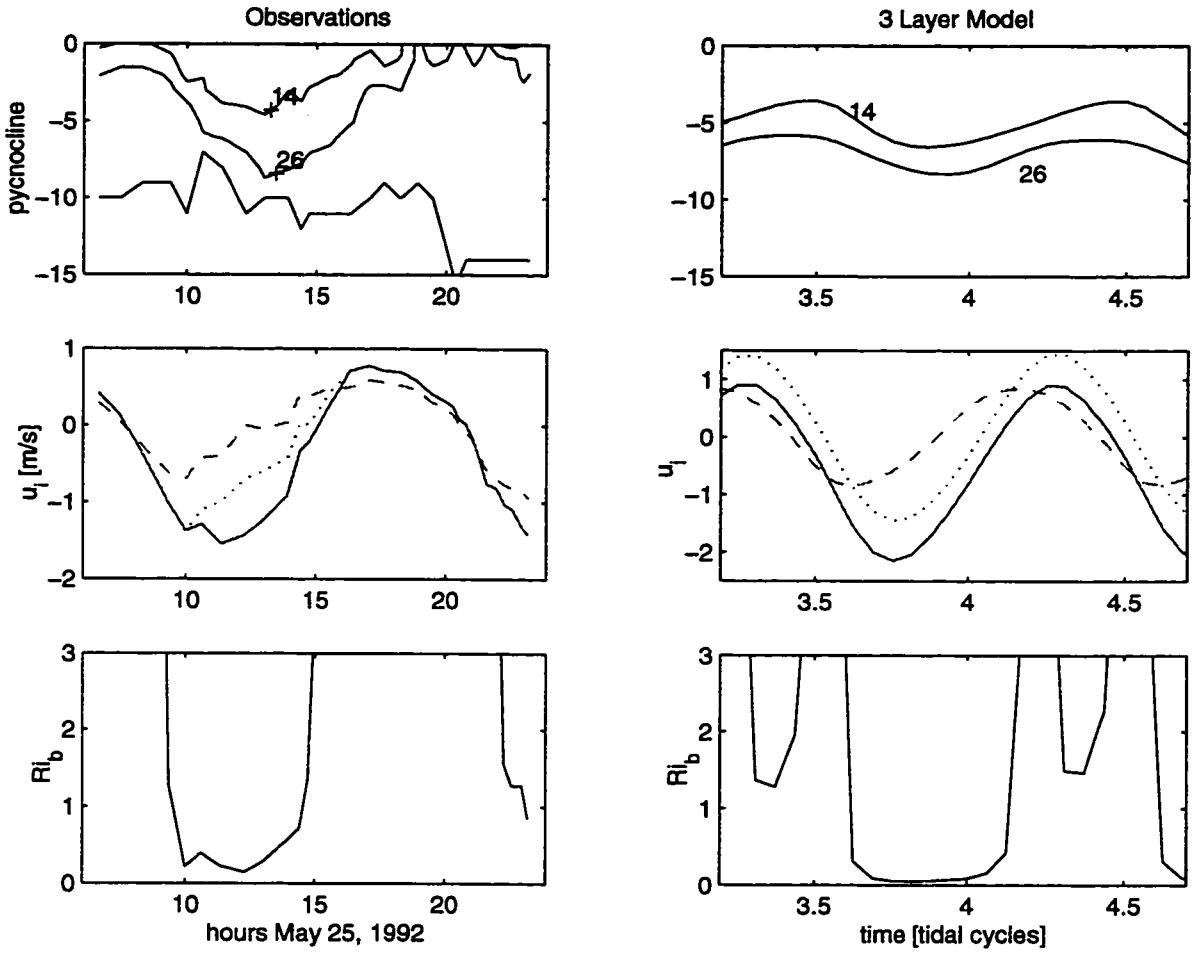

Figure 8.5: Time series of salinity, currents and bulk Richardson number. First column, observations; second column, three-layer model results. The modeled pycnocline is imperfect, but modeled upper (solid line) and lower layer (dashed line) currents closely resemble observations. Ri_b is < 0.3 on ebb and > 3 on flood.

Chapter 9

CONCLUSIONS

The Columbia River has a large, bilogically productive estuary whose ecosystem depends on the balance of salt and fresh water. The river also forms a vast buoyant plume which affects circulation for hundreds of miles along the coast. Both the estuarine salt balance and the initial state of the plume are determined by flow through the narrow entrance channel.

The exchange of salt and fresh water in the entrance channel qualitatively resembles a simple two layer model: a seaward moving fresh layer over a landward moving salt layer. However, the two-layer inviscid model has significant limitations, which I have addressed in three ways in this thesis. First, my observations in the Columbia River entrance channel reveal the effects of bottom friction and vertical mixing on the two-layer exchange flow [Cudaback and Jay, 1996]. Second, a two-layer time-dependent numerical model demonstrates the importance of bottom friction to total transport, and may also be used to estimate the thickness of the density interface (pycnocline). Third, a three-layer numerical model replicates an interesting feature of circulation on a flood tide.

9.1 Observations

Two sets of velocity and density observations were collected in the Columbia River entrance channel; time series data in May 1992 and along-channel sections in the fall of 1993 [Cudaback and Jay, 1996]. The estuary is salt-stratified, so salinity data is often used instead of density data. Time series of salinity show that the pycnocline

moves up and down tidally, being nearest to the surface shortly after peak flood. The pycnocline also grows rapidly due to shear induced mixing on ebb, so it fills more than half the water column shortly after peak ebb. The pycnocline thins and rises again as ebb turns to flood. This contrasts with the two-layer inviscid model, in which the interface between salt and fresh water always has zero thickness.

Along-channel sections on early flood show a mid-depth band of strong currents (a jet). This jet is strongest just landward of the channel constriction, where currents at all depths are fastest (figure 3.3). The vertical structure of the currents is due to a combination of barotropic and baroclinic forces and bottom friction. Baroclinic forces increase toward the bottom, so flood currents would be strongest at the bottom, in the absence of bottom friction. Bottom friction retards the bottom currents, forcing the maximum current up into the pycnocline. The pycnocline acts, to some extent, as a dynamically independent layer, and slides freely between the salt and fresh layers.

9.2 Two-Layer Model

A time dependent two-layer numerical model quantifies the behavior of the pycnocline. Helfrich [1995] published a two-layer inviscid model, to which I added bottom friction and an estimate of pycnocline thickness. The model domain represents a narrow, shallow channel between infinite basins of salt and fresh water. In cross section, the model channel has a flat bottom and vertical sides. Baroclinic forces set up a steady two-way exchange, with a seaward-moving surface fresh layer and a landward-moving bottom salt layer. The layer interface drops toward the landward end of the model domain and has the greatest slope near a lateral constriction, due to hydraulic control. When tidal and riverine currents are imposed, layer speeds and thicknesses vary along-channel and with time. The interface moves landward and seaward with the tides; at a single location this motion is seen as a vertical oscillation.

In the absence of bottom friction, the modeled layer interface at the constriction

is near the bottom shortly after peak ebb, and near the surface shortly after peak flood. Bottom friction reduces the range of oscillation of the interface, so it is always at or above mid-depth. Bottom friction also displaces the whole interface landward (figure 5.3), which may be interpreted as preserving transport in the bottom layer or as a change in internal hydraulic control [Pratt, 1986].

I estimated pycnocline thickness from two-layer model results assuming the bulk Richardson number was nearly critical ($Ri_b = 0.3$). This is consistent with observations of the Columbia and Fraser Rivers: on ebb, shear induced turbulence causes the pycnocline to grow until Ri_b reaches a critical value of 0.3-1. In the absence of bottom friction, the modeled pycnocline is thinner and lower in the water column than observed. The addition of bottom friction raises the pycnocline as described above. Bottom friction also increases vertical shear on ebb, causing the pycnocline to grow rapidly, and decreases the shear on flood, so that the pycnocline collapses again. Monismith and Fong [1996] also noted this effect of bottom friction on pycnocline thickness. The pycnocline calculated from two-layer model results with bottom friction fit the observed pycnocline very well (figure 5.5).

9.3 Three-Layer Model

The two-layer model can simulate pycnocline thickness, but not mid-depth currents. I developed a three-layer model to simulate the observed mid-depth maximum in flood currents. This model is similar to the two-layer model, with the addition of shear-induced mixing. When the middle layer is very thin, strong vertical shears drive turbulent overturns and create water of intermediate density. This effect is represented by entrainment into the middle layer, which represents the pycnocline. The speed of entrainment is based on an empirical function of a bulk Richardson number [Ellison and Turner, 1959]. Entrainment stops when the Richardson number reaches a critical value of 0.8.

In the three layer model, bottom friction breaks the tidal symmetry of internal circulation. With purely tidal currents (1.2 $m \cdot s^{-1}$, peak flood and peak ebb), and no bottom friction, a simple two-way exchange flow is seen at slack before flood and at slack before ebb. Flood currents are strongest at the bottom, weaker at mid-depth and nonexistent at the surface. Ebb currents are strongest at the surface, weaker at mid-depth and nonexistent at the bottom (figure 7.3). Flood circulation is thus the symmetric opposite of ebb circulation. With moderate bottom friction, flood currents are strongest in the middle layer near the landward end of the model channel (figure 7.4). This jet is smaller than that observed in the field, but is qualitatively correct. Ebb currents are strongest in the surface layer, so there is no longer symmetry between ebb and flood. The addition of a river flow to this model, (0.3 $m \cdot s^{-1}$, figure 7.5) changes the mean flow but has a relatively modest effect on internal circulation.

The three-layer model best matches observations when the bottom friction is increased above the values most commonly listed in the literature. This increase is necessitated by the multi-layer nature of the model and by the square channel cross section used in the model. With this larger bottom friction, the three-layer model accurately represents the along-channel and vertical structure of density and currents at most stages of the tide, including a strong mid-depth jet in the flood currents. These results also simulate the mid-depth maximum in ebb and flood salinity transport and the tidal variation in the bulk Richardson number.

BIBLIOGRAPHY

Arita, M. and Jirka, G. H. (1987). Two-layer model of saline wedge. i. entrainment and interfacial friction. *Journal of Hydraulic Engineering*, **113**(10), 1229–1248.

Armi, L. (1986). The hydraulics of two flowing layers with different densities. *Journal of Fluid Mechanics*, **163**, 27–58.

Armi, L. and Farmer, D. M. (1986). Maximal two-layer exchange through a contraction with barotropic net flow. *Journal of Fluid Mechanics*, **164**, 27–52.

Barnes, C. A., Duxbury, A., and Morse, B. (1972). Circulation and selected properties of the Columbia River effluent at sea. In A. T. Pruter and D. L. Alverson, editors, *The Columbia River Estuary and Adjacent Ocean Waters*. University of Washington Press.

Baross, J., Crump, B., and Simenstad, C. A. (1994). Elevated microbial loop activities in the columbia river estuary turbidity maximum. In K. Dyer and R. Orth, editors, *Changing Particle Fluxes in Estuaries: Implications from Science to Management*, pages 459–464. Olsen and Olsen Press, Friedensborg.

Bormans, M. and Garrett, C. (1989). The effects of nonrectangular cross section, friction and barotropic fluctuations on the exchange through the strait of gibralter. *Journal of Physical Oceanography*, pages 1543–1557.

Chao, S.-Y. and Paluskiewicz, T. (1991). The hydraulics of density currents over estuarine sills. *Journal of Geophysical Research*, **96**(C4), 7065–7076.

Cudaback, C. N. and Jay, D. A. (1996). Formation of the Columbia River plume - hydraulic control in action? In D. Aubrey, editor, *Buoyancy Effects on Coastal and Estuarine Dynamics*, pages 139–154. American Geophysical Union.

Cudaback, C. N. and Jay, D. A. (1997). Lateral circulation and forcing in the columbia river entrance channel. *Estuarine, Coastal and Shelf Science*. submitted.

Ellison, T. H. and Turner, J. S. (1959). Turbulent entrainment in stratified flows. *Journal of Fluid Mechanics*, **6**, 423–448.

Farmer, D. M. and Armi, L. (1986). Maximal two-layer exchange over a sill and through the combination of a sill and contraction with net barotropic flow. *Journal of Fluid Mechanics*, **164**, 53–76.

Fischer, H. (1976). Mixing and dispersion in estuaries. *Annual Review of Fluid Mechanics*, **17**, 47–58.

Garcia, M. H. and Parsons, J. D. (1996). Mixing at the front of gravity currents. *Dynamics of Atmospheres and Oceans*, **24**, 197–205.

Garvine, R. (1987). Estuary plumes and fronts in shelf waters: a layer model. *Journal of Physical Oceanography*, **17**, 1877–1896.

Geyer, W. R. (1985). *The time-dependent dynamics of a salt wedge*. Ph.D. thesis, University of Washington, Seattle, Washington.

Geyer, W. R. (1988). The advance of a salt wedge front: observations and dynamical model. In J. Dronkers and W. van Leussen, editors, *Physical Processes in Estuaries*, pages 295–310. Springer-Verlag, New York.

Geyer, W. R. (1990). Time-dependent, two-layer flow over a sill. In L. Pratt, editor, *The Physical Oceanography of Sea Straits*, pages 421–432. Kluwer Academic Publishers, The Netherlands.

Geyer, W. R. (1993). Three-dimensional tidal flow around headlands. *Journal of Geophysical Research*, **98**, 955–966.

Geyer, W. R. and Smith, J. (1987). Shear instability in a highly stratified estuary. *Journal of Physical Oceanography*, **17**, 1668–1679.

Giese, B. S. and Jay, D. A. (1989). Modelling tidal energetics of the columbia river estuary. *Estuarine, Coastal and Shelf Science*, **29**, 549–571.

Grubert, J. P. (1989). Interfacial mixing in stratified channel flows. *Journal of Hydraulic Engineering*, **115**, 887–905.

Hacker, J., Linden, P., and Dalziel, S. B. (1996). Mixing in lock-release gravity currents. *Dynamics of Atmospheres and Oceans*, **24**, 183–195.

Helfrich, K. (1995). Time-dependent two-layer hydraulic exchange flows. *Journal of Physical Oceanography*, **25**, 359–373.

Hickey, B. M., Pietrafesa, L. J., Jay, D. A., and Boicourt, W. C. (1998). The columbia river plume study: subtidal variability in the velocity and salinity fields. *Journal of Geophysical Research*. in press.

Hughes, F. and Rattray, M. (1980). Salt flux and mixing in the columbia river estuary. *Estuarine and Coastal Marine Science*, **10**, 479–493.

Ianniello, J. P. (1977). Tidally induced residual currents in estuaries of constant breadth and depth. *Journal of Marine Research*, **35**, 755–786.

Jay, D. A. (1991). Green's law revisited: tidal long-wave propagation in channels with strong topography. *Journal of Geophysical Research*, **96**, 20585–98.

Jay, D. A. and Musiak, J. D. (1994). Particle trapping in estuarine tidal flows. *Journal of Geophysical Research*, **99**, 446–461.

Jay, D. A. and Musiak, J. D. (1996). Internal tidal asymmetry in channel flows: origins and consequences. In C. Pattiaratchi, editor, *Mixing Processes in Estuaries and Coastal Seas*, pages 219–258. American Geophysical Union.

Jay, D. A. and Smith, J. D. (1990a). Circulation, density distribution and neap-spring transitions in the columbia river estuary. *Progress in Oceanography*, **25**, 81–112.

Jay, D. A. and Smith, J. D. (1990b). Residual circulation in shallow estuaries. part 1: Highly stratified, narrow estuaries. *Journal of Geophysical Research*, **95**(1), 711–731.

Kay, D. J., Jay, D. A., and Musiak, J. D. (1996). Salt transport through an estuarine cross-section calculated from moving vessel adcp and ctd data. In D. G. Aubrey, editor, *Buoyancy effects in estuaries*. American Geophysical Union.

Koop, C. and Browand, F. K. (1978). Instability and turbulence in a stratified flow with shear. *Journal of Fluid Mechanics*, **93**(1), 135–159.

Largier, J. (1992). Tidal intrusion fronts. *Estuaries*, **15**, 26–39.

Lawrence, G. A. (1985). *The hydraulics and mixing of two-layer flow over an obstacle*. Ph.D. thesis, University of California, Berkeley, California. Lab report number UCB/HEL-85/02.

Lawrence, G. A. (1990). On the hydraulics of Boussinesq and non-Boussinesq two-layer flows. *Journal of Fluid Mechanics*, **215**, 457–480.

Mellor, G. L. and Yamada, T. (1982). Development of a turbulence closure model for geophysical fluid problems. *Reviews of Geophysics*, **20**, 851–875.

Monismith, S. G. and Fong, D. A. (1996). A simple model of mixing in stratified tidal flows. *Journal of Geophysical Research*, **101**(C12), 28583–28595.

Morgan, C. A. (1993). *Sink or swim? Copepod population maintenance in the Columbia River estuarine turbidity maxima region*. Master's thesis, University of Washington, Seattle, Washington.

Nelson, J. M. (1988). *Mechanics of flow and sediment transport over nonuniform erodible beds*. Ph.D. thesis, University of Washington, Seattle, Washington.

Officer, C. B. (1976). *Physical oceanography of estuaries (and associated coastal waters)*. J. Wiley and Sons, New York.

Orlanski, I. (1976). A simple boundary condition for unbounded hyperbolic flows. *Journal of Computational Physics*, **21**, 251–269.

Pawlak, G. and Armi, L. (1996). Stability and mixing of a two-layer exhange flow. *Dynamics of Atmospheres and Oceans*, **24**, 139–151.

Pawlak, G. and Armi, L. (1997). Hydraulics of two-layer arrested wedge flows. *Journal of Hydraulic Research*.

Peters, H. (1997). Observations of stratified turbulent mixin in an estuary: neap-to-spring variations during high river flow. *Estuarine, Coastal and Shelf Science*, **45**, 69–88.

Pratt, L. J. (1986). Hydraulic control of sill flow with bottom friction. *Journal of Physical Oceanography*, **16**, 1970–1980.

Press, W. H., Tukolsky, S., Vettering, W., and Flannery, B. P. (1992). *Numerical Recipes in FORTRAN, the Art of Scientific Computing*. Cambridge University Press, 2nd edition.

Price, J. F. and Baringer, M. O. (1994). Outflows and deep water production by marginal seas. *Progress in Oceanography*, **33**, 161–200.

Rouse, H. (1947). *Elementary Mechanics of Fluids*. J. Wiley and Sons, New York.

Sherwood, C. P., Jay, D. A., Harvey, B., Hamilton, P., and Simenstad, C. A. (1990). Historical changes in the columbia river estuary. *Progress in Oceanography*, **25**, 299–352.

Simenstad, C. A., Small, L. F., McIntire, C. D., Jay, D. A., and Sherwood, C. P. (1990). Columbia river estuary studies: An introduction to the estuary, a brief history, and prior studies. *Progress in Oceanography*, **25**, 1–13.

Simenstad, C. A., Jay, D. A., and Sherwood, C. R. (1992). Impacts of watershed management on land-margin ecosystems: The columbia river estuary as a case study. In R. J. Naiman, editor, *New Perspective in Watershed Management*, pages 266–306. Springer-Verlag, New York.

Simpson, J. E. (1972). Effects of the lower boundary on the head of a gravity current. *Journal of Fluid Mechanics*, **53**, 759–768.

Smith, J. and McLean, S. (1984). A model for flow in meandering streams. *Water Resources Research*, **20**, 1301–1315.

Turner, J. S. (1986). Turbulent entrainment: the development of the entrainment assumption, and its application to geophysical flows. *Journal of Fluid Mechanics*, **173**, 431–171.

Valle-Levinson, A. and Wilson, R. E. (1994). Effects of sill bathymetry, oscillating barotropic forcing and vertical mixing on estuary/ocean exchange. *Journal of Geophysical Research*, pages 5149–5169.

Wood, I. R. (1970). A lock exchange flow. *Journal of Fluid Mechanics*, **42**, 671–687.

Yonemitsu, N., Swaters, G., Rajaratnam, N., and Lawrence, G. (1996). Shear instabilities in arrested salt-wedge flows. *Dynamics of Atmospheres and Oceans*, **24**, 173–182.

Zhu, Z. and Lawrence, G. A. (1996). Exchange flow through a channel with an underwater sill. *Dynamics of Atmospheres and Oceans*, **24**, 153–161.

Appendix A

OBSERVED ALONG-CHANNEL SECTIONS

In September and October of 1993, I got some free ship time, and used it to compare circulation in the Columbia River entrance channel with internal hydraulic control theory. We collected about 18 along-channel transects crossing a modest sill in the entrance channel (figure 1.3). Some of the ADCP and CTD data are discussed in chapter 3, which has also been published as Cudaback and Jay [1996]. All of the sections are assembled here for an overview.

Each of the next four figures represents a single (short) day of data collection. The top plot in each figure shows tidal heights for the appropriate day, with the approximate time of each section marked. Each section took about an hour, and the arrow at the bottom of each salinity plot shows the direction of travel.

Four along-channel transects were made on the morning flood, September 28, 1993 (figure A.1). For the first two transects (line 3 at 0600 and line 4 at 0700), the water column was salt-stratified, and the pycnocline moved landward. During this same interval, the flood current intensified, and the location of strongest currents moved upward from 10 meters to 5 meters depth. At peak flood (line 5 at 0800), the strongest flood currents are observed at the surface, and salt water ($>$ 28 psu) has mostly filled the water column. On this section, a strong lateral convergence front was observed around kilometer 5; the 28 psu isohaline intersects the surface at that point, and there are strong along channel gradients in u. As the flood slacks off (line 6 after 1000), currents remain stronger near the surface, and the saltiest water ($>$ 32 psu) has apparently settled into the hole landward of kilometer 2.

On September 29, (figure A.2) observations start at the beginning of flood (line

7, 0600 pst), when the surface is still ebbing and there are weak landward currents at the bottom. The next two sections show the landward motion of the salt wedge (32 psu isohaline, and the upward motion of the maximum flood current. The water column remains stratified over this period.

The observations on October 18 (figure A.3) were made on flood and on early ebb. The early flood transect (line 12, 1130PST) shows the typical mid-depth maximum and is discussed at length in chapter 3. Ebb onset (line 13) is very different from flood onset. Due to the constant pressure of the river currents, the ebb starts simultaneously at all depths, instead of starting gradually from the surface. This signal propagates down the estuary, so that currents are ebbing at all depths landward of kilometer 2, and flooding at all depths seaward of kilometer 2. Later on ebb (line 14), currents are somewhat surface-enhanced due to bottom friction. Note that the salty oceanic water (> 28 psu) has not yet been cleared out of the estuary.

The observations for October 19 (figure A.4) follow the transition from very late ebb to peak flood, and results are quite similar to other flood periods. At the very beginning of flood, currents are weakly landward at the bottom, and strongly seaward at the surface, and the water column is salt-stratified. Line 15 is also discussed in chapter 3. As the flood progresses (lines 16 and 17), flood currents move from mid-depth to the surface, and the estuary fills again with oceanic water.

Taken together, these plots show a consistent tidal cycle. At the beginning of flood, the water is salt stratified. The surface layer ebbs while the bottom layer floods – this is the only instance of two-layer flow in the tidal cycle. The growing flood current moves from the bottom to the surface as the estuary fills with salt water. At the start of ebb, the water is unstratified. Ebb currents start suddenly at all depths, and the ebb propagates quickly down the river. Peak ebb currents should be strongest at the surface, but we have no along-channel sections from that dangerous time.

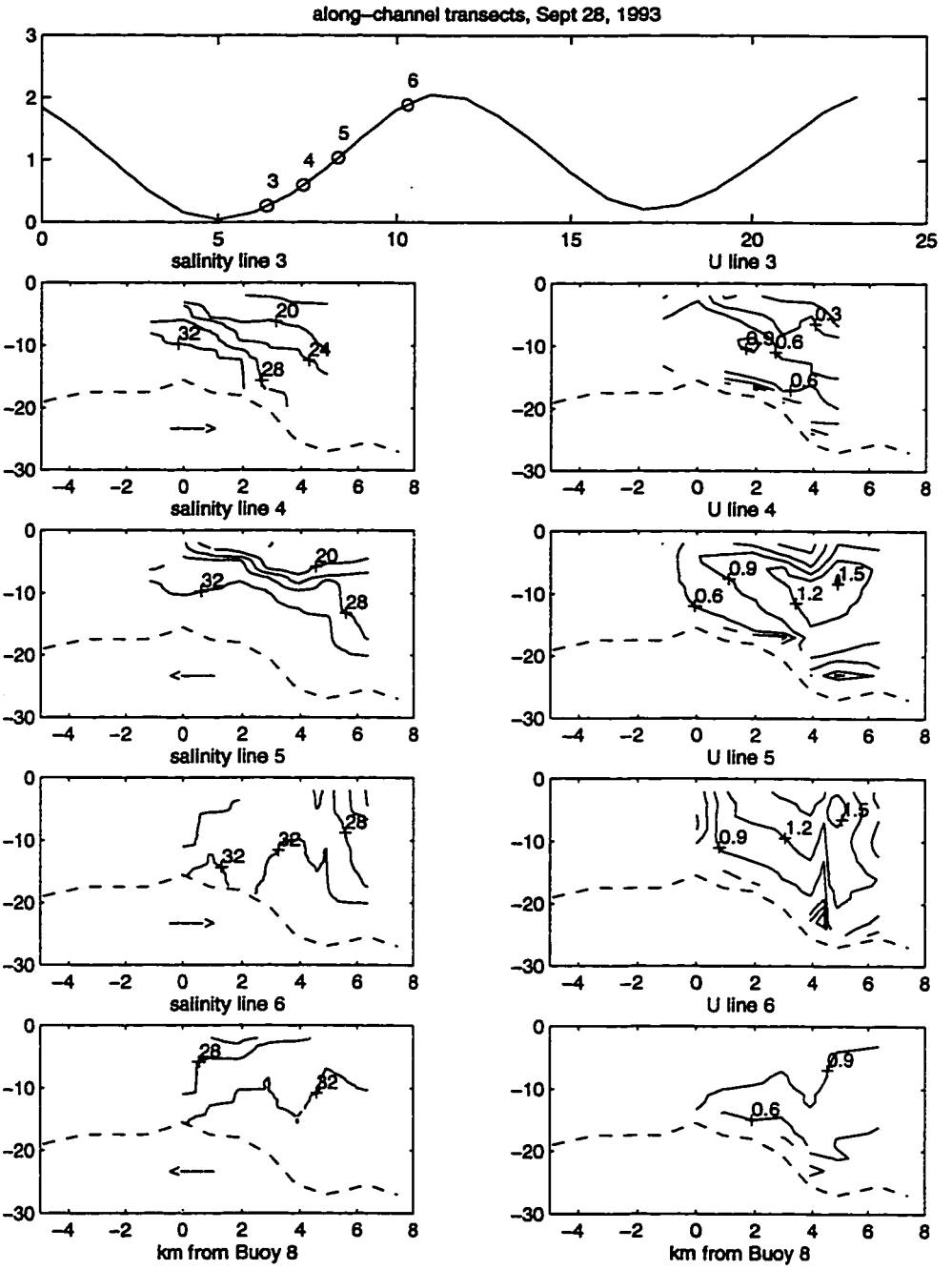

Figure A.1: Along channel sections from September 28, 1993.

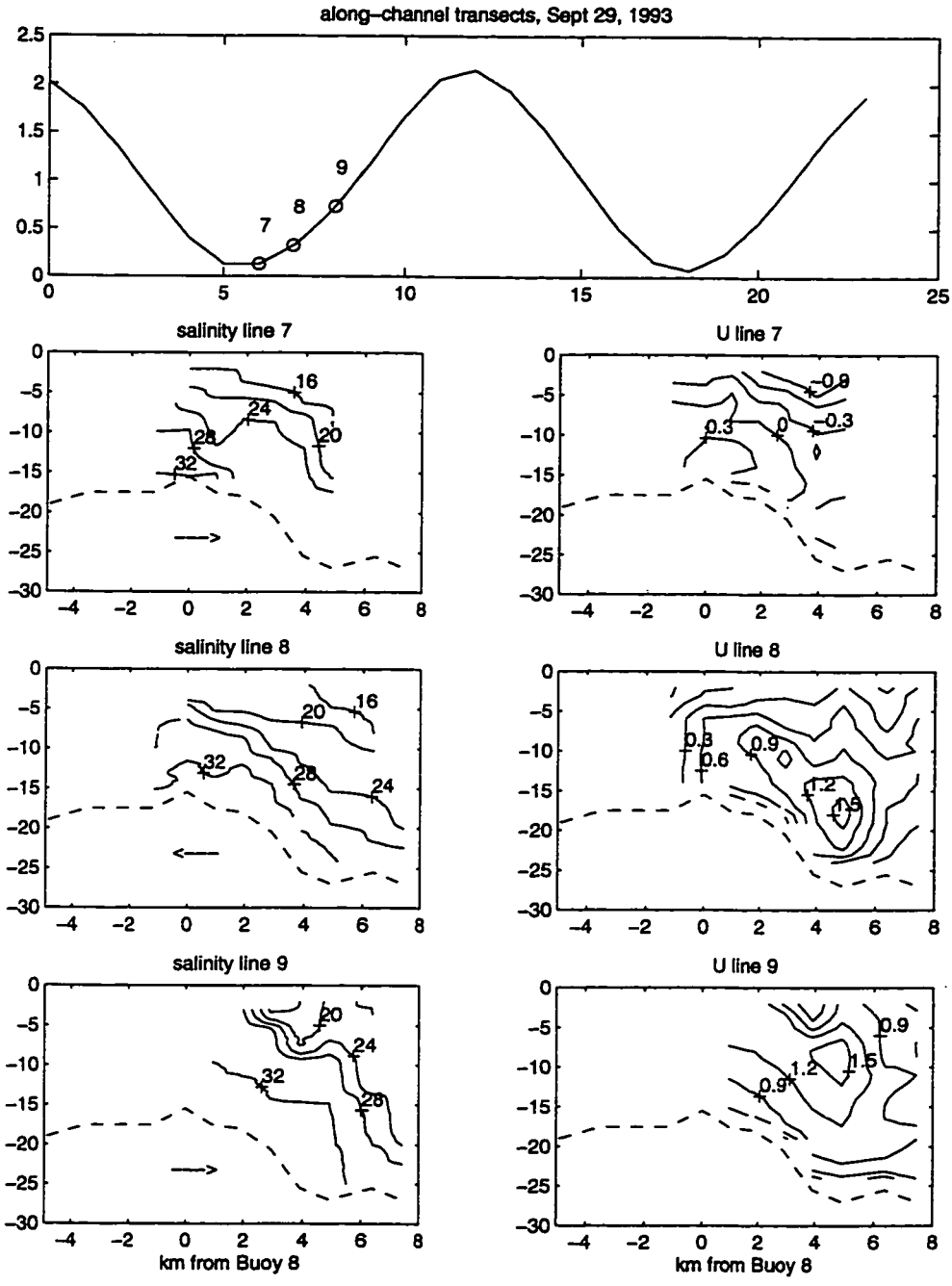

Figure A.2: Along channel sections from September 29, 1993.

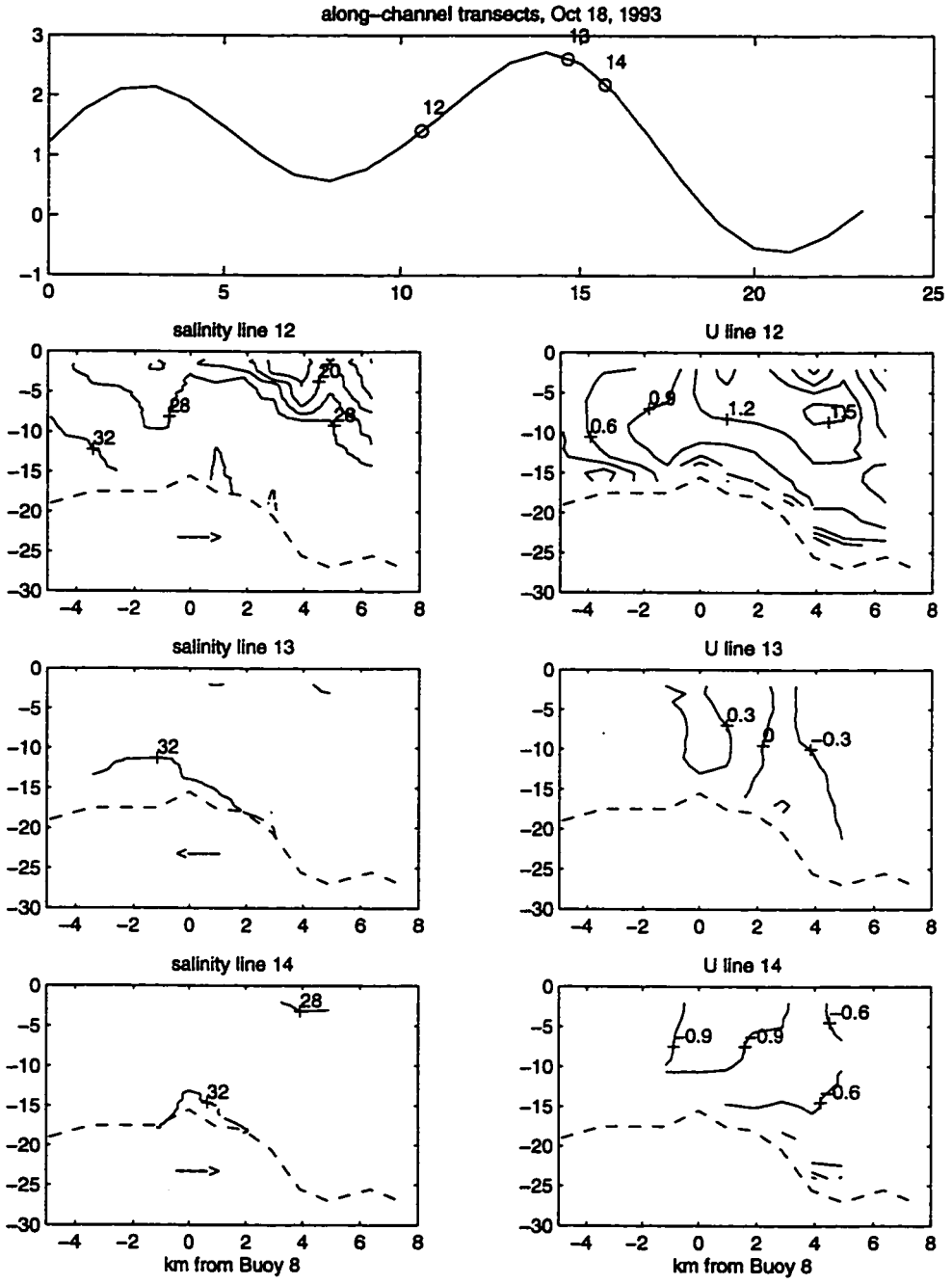

Figure A.3: Along channel sections from October 18, 1993.

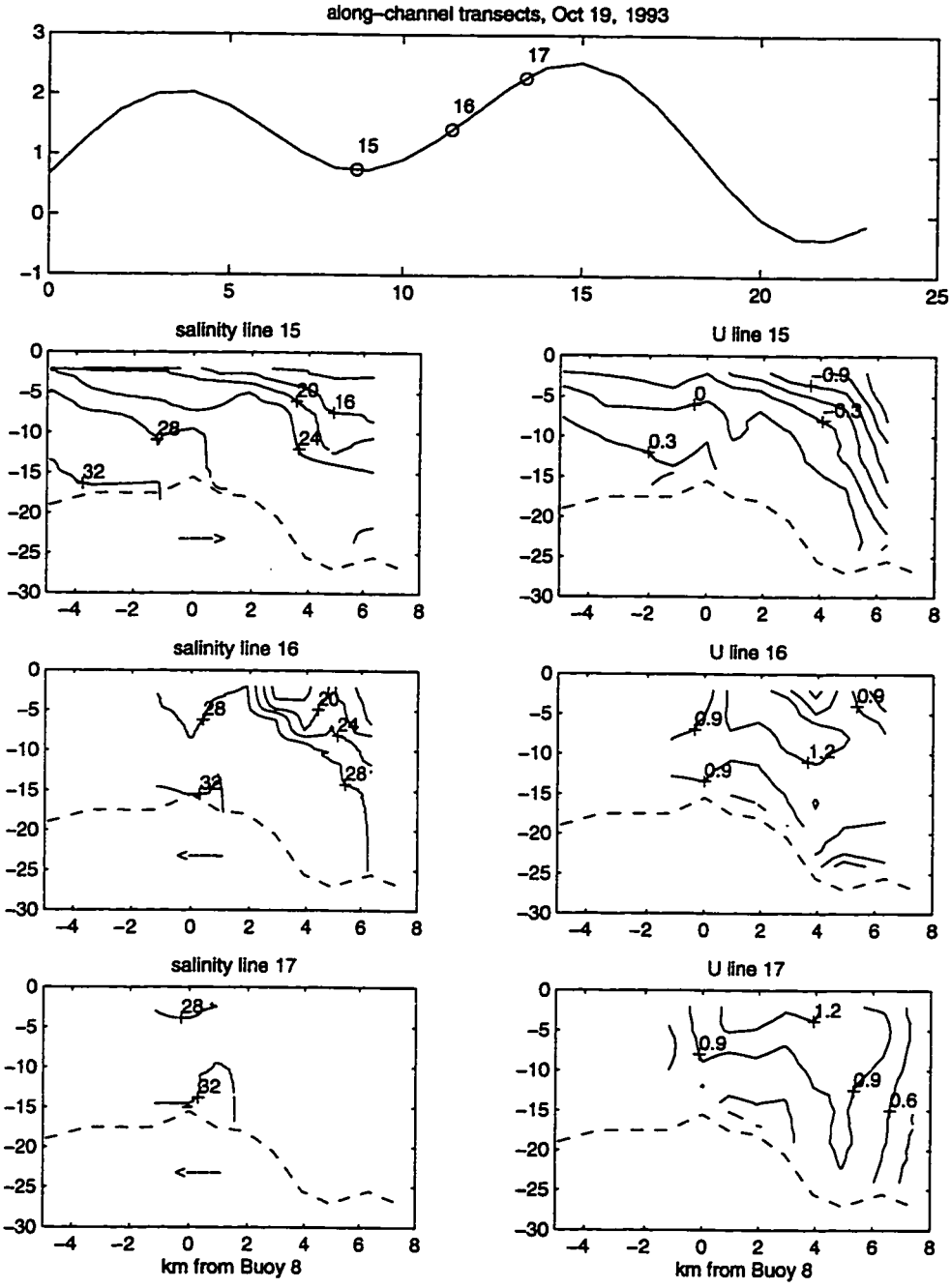

Figure A.4: Along channel sections from October 18, 1993.

VITA

NAME: Cynthia Nova Cudaback

EDUCATION:

1986 BA, University of California, Berkeley

AWARDS:

1991 Office of Naval Research Graduate Student Fellowship

PUBLICATIONS:

Cudaback, C. N. and D. A. Jay, 1997, *Lateral Circulation and Forcing in the Columbia River Entrance*, submitted to **Estuarine and Coastal Shelf Studies.**

Cudaback, C. N. and D. A. Jay, 1996, *Formation of the Columbia River plume - hydraulic control in action?*, in: D. Aubrey(ed), **Buoyancy effects on Coastal Dynamics, An AGU Coastal and Estuarine Sciences Monograph.**

Cudaback, C. N., A. J. Paulson and J. W. Lavelle, 1991, *A modeling study of the vertical distribution and transport of manganese in Puget Sound*, **NOAA Technical Memorandum ERL PMEL-93.**

Lavelle, J. W., C. N. Cudaback, A. J. Paulson and J. A. Murray, 1991, *A rate for the scavenging of fine particles by macroaggregates in a deep estuary*, **Journal of Geophysical Research, 96(C1).**

SELECTED PRESENTATIONS:

Cudaback, C. N. and D. A. Jay, 1998, *Parameterized friction and mixing in a layered flow with tidal currents: a new three-layer model*, **Ocean Sciences.**

Cudaback, C. N. and D. A. Jay, 1996, *The link between vertical mixing and along-channel transport in a layered flow*, **American Geophysical Union.**

Cudaback, C. N. and D. A. Jay, 1996, *River-ocean exchange at the Columbia River entrance: how it works*, **Land Margin Ecosystem Research**, all scientists meeting.

Cudaback, C. N. and D. A. Jay, 1995, *Lateral circulation and forcing in the Columbia River entrance channel*, **International Union of Geodesy and Geophysics.**

Cudaback, C. N. and D. A. Jay, 1994, *Formation of the Columbia River plume - hydraulic control in action?*, poster, **Physics of Estuaries and Coastal Seas.**

Cudaback, C. N. and D. A. Jay, 1993, *Estuary-Plume coupling at the Columbia River entrance*, **Estuarine Research Federation**, 1993.

IMAGE EVALUATION
TEST TARGET (QA-3)

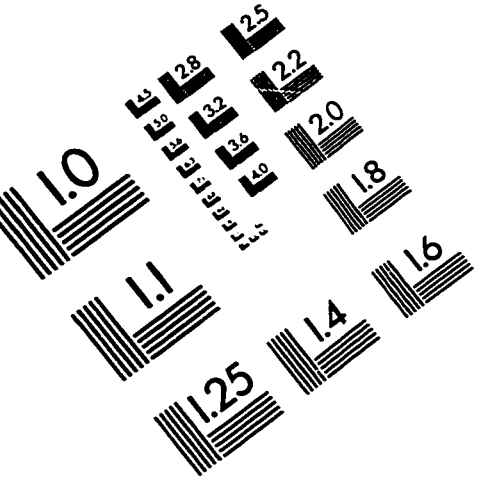

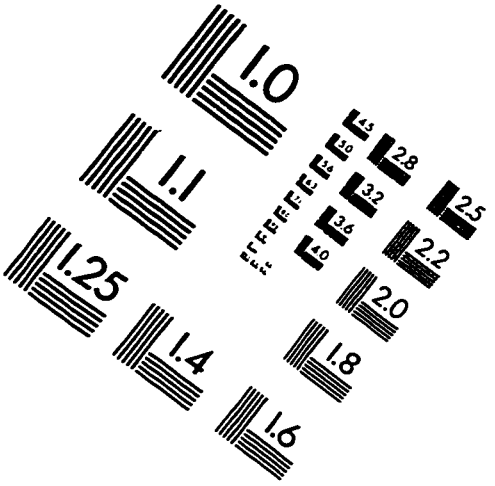

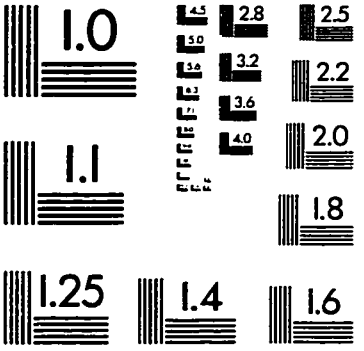

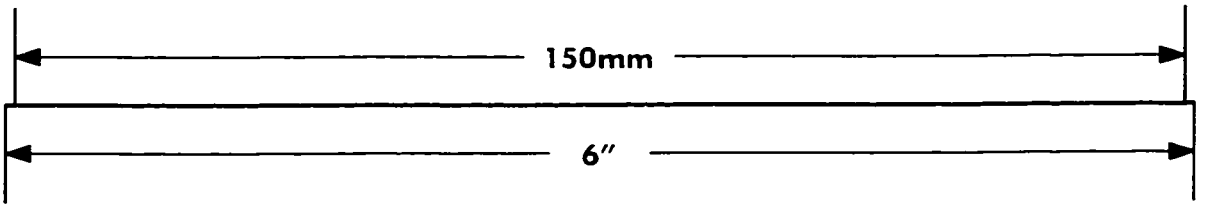

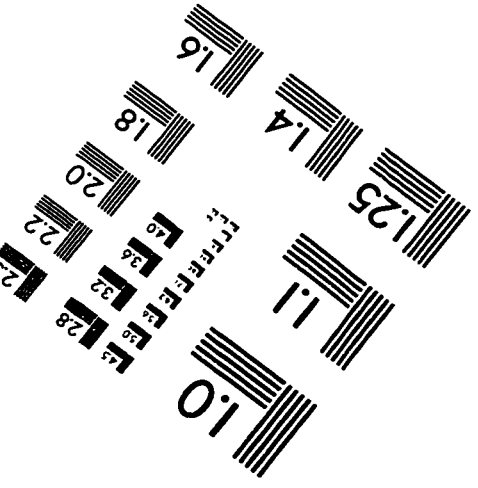

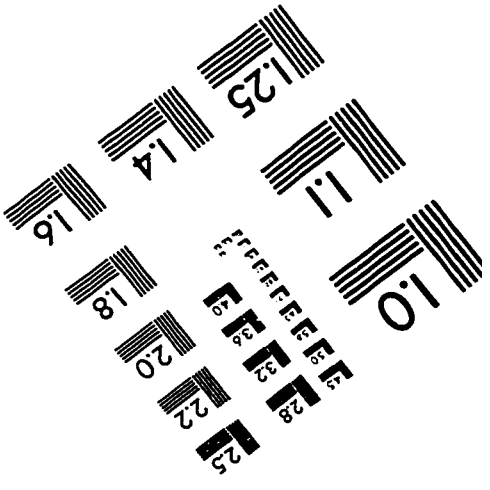

APPLIED IMAGE, Inc
1653 East Main Street
Rochester, NY 14609 USA
Phone: 716/482-0300
Fax: 716/288-5989